Title: Increased rates of hybridization in swordtails are associated with water pollution

Authors:

Benjamin M Moran[1,2,3†], Wilson F Ramírez-Duarte[2,4,5], Daniel L Powell[1,2,6], Terrance TL Yang[1], Theresa R Gunn[1,2], Gaston I Jofre-Rodríguez[2,7], Cheyenne Y Payne[8,9], Erik NK Iverson[10], Gabriel A Preising[1,2], Shreya M Banerjee[3], Alexandra E Donny[1,11], Rhea Sood[1], John J Baczenas[1], Gabriela María Vázquez Adame[2], Carla Gutiérrez-Rodríguez[12], Chelsea M Rochman[4], Molly Schumer[1,2,13*†], Gil G Rosenthal[2,14*]

Affiliations:

[1] Department of Biology, Stanford University

[2] Centro de Investigaciones Científicas de las Huastecas "Aguazarca", A.C.

[3] Present Address: Department of Evolution and Ecology, University of California at Davis

[4] Department of Ecology & Evolutionary Biology, University of Toronto

[5] Present Address: Department of Environmental & Physical Sciences, Concordia University of Edmonton

[6] Department of Biological Sciences, Louisiana State University

[7] Department of Biology, Virginia Commonwealth University

[8] Department of Ecology and Evolutionary Biology, University of California, Santa Cruz

[9] Southwest Fisheries Science Center, National Marine Fisheries Service, National Oceanic and Atmospheric Administration

[10] Department of Integrative Biology, University of Texas at Austin

[11] Department of Genome Sciences, University of Washington

[12] Red de Biología Evolutiva, Instituto de Ecología A.C

[13] Freeman Hrabowski Fellow, Howard Hughes Medical Institute

[14] Dipartimento di Biologia, Università degli Studi di Padova

* co-supervised this work

[†] Correspondence: bmmoran@ucdavis.edu, schumer@stanford.edu

Running Head: Anthropogenic hybridization in swordtails

Keywords: hybridization, hybrid populations, anthropogenic change, water quality, mate choice, freshwater fish, Poeciliidae, land use

Summary

The nature of reproductive barriers that separate species is a fundamental question in evolutionary biology. Such barriers may be sensitive to environmental conditions, and recent research has documented an increasing number of cases where anthropogenic environmental disturbance is associated with new hybrid populations. However, few studies have been able to quantitatively compare potential environmental drivers and test possible mechanisms connecting interspecific hybridization to anthropogenic disturbance. Here, we combine genomic and chemical surveys to explore the loss of reproductive isolation between the sister species *Xiphophorus malinche* and *X. birchmanni*, fishes whose riverine habitat in the Sierra Madre Oriental of Mexico is increasingly impacted by human-mediated disturbance. By inferring genome-wide ancestry in thousands of fish, we characterize the landscape of hybridization between these species in four distinct streams. Ancestry structure varied dramatically across streams, ranging from stable coexistence to clinal hybrid zones, hinting that the dynamics of hybridization in this system may be environmentally dependent. In one stream, a sudden shift in hybridization patterns coincides with the stream's passage through an urbanized area, with upstream sites showing distinct ancestry clusters and downstream sites showing a swarm of hybrids with variable ancestry. By sequencing mothers and embryos, we show that assortative mating by ancestry is weakened downstream of this urbanized area. We hypothesize that the hybrid swarm downstream of the town is driven by chemical disruption of olfaction that impacts mating preferences. Water chemistry measurements show that water quality changes significantly across this area, including in parameters known to disrupt fish olfaction and mating. We identify alterations of the olfactory epithelium between sites upstream and downstream of the urbanized

area that are consistent with differential effects of water quality. Taken together, our work illuminates potential mechanisms linking anthropogenic disturbance to the breakdown of reproductive isolation in these hybridizing species.

Introduction

To understand speciation, evolutionary biologists have long studied cases in which barriers to reproduction between species are incomplete and hybridization can occur (1, 2). Such studies have sometimes found evidence that hybridization occurs in areas of environmental disturbance. Disturbance can bring together species that do not otherwise coexist, create novel environments where hybrids thrive, or alter the interactions between species that previously coexisted without interbreeding (3–5). Empirical work has shown that premating barriers, such as a behavioral preference for mating with conspecifics (i.e. assortative mating), are highly context-dependent (6–10) and sensitive to environmental conditions (11, 12). They may therefore disappear in the face of disturbances that impact mechanisms of mate discrimination (13–15).

While natural changes to the environment may have been the major source of disturbance historically, human impacts (e.g. changes in land use, chemical pollution, resource extraction) have likely played an analogous role in recent decades (14, 16–18). Human modification of the environment can interfere with mechanisms used by conspecifics to identify each other, either by directly affecting signal production and transmission or by abolishing conspecific preferences (14, 19, 20). Ultimately, these changes can alter the impact of sexual selection on speciation dynamics (21). In aquatic species, in particular, a variety of chemical pollutants have been shown to weaken or ablate conspecific mate preferences (14, 19, 20, 22–24). As human impacts on the environment become ubiquitous (25), the reported rate of hybridization appears to be increasing across a range of taxa (5).

If assortative mating is a major reproductive barrier between species, weakening this barrier can lead to a collapse of population structure and phenotypic divergence (26–30), often

referred to as a “hybrid swarm”. Since mate discrimination is typically weaker in hybrids than in parental species (13), this can lead to irreversible phenotypic and genetic homogenization through hybridization (i.e. “speciation reversal” or “genetic swamping”). Although hybridization may sometimes lead to adaptive introgression (31, 32) or the formation of new species (33), the immediate consequence of the formation of hybrid swarms is more often the loss of genetic differentiation and functional biodiversity (18, 34). Moreover, early-generation hybrids often experience intrinsic hybrid incompatibilities (35, 36) and thus hybridization may also decrease fitness and overall population size.

Swordtails (Teleostei: genus *Xiphophorus*) provide a compelling system to study barriers to gene flow and their breakdown following anthropogenic disturbance. As model systems for hybridization and mate choice, these stream fishes have been the subject of numerous studies showing that mating preferences can be altered by environmental and social context (7, 8, 13, 19). Swordtails are found along the eastern slopes of the Sierra Madre Oriental and Gulf Coastal Plain of Mexico, a region experiencing growing human population density and agricultural land conversion since the 20th century (37, 38). This change in land use has impacted water quality, while also threatening the area’s exceptional biodiversity (39, 40). The sister species *X. malinche* and *X. birchmanni* overlap in the montane streams of northern Hidalgo state, Mexico, where steep slopes create frequent barriers to migration (waterfalls, cascades, and subterranean stream reaches) and coincide with dramatic ecological variation over short geographic distances. *X. malinche* occupy cool headwaters, while *X. birchmanni* are found in warmer lower-elevation streams, creating the potential for ecological selection against hybrids (41, 42). Genome-wide divergence between the species is moderate (D_{XY} = 0.45%) (43) and early-generation hybrids between these species suffer from severe genetic incompatibilities (44–46). However, some

hybrids are viable and fertile, and hybrid populations can be found in multiple independent stream reaches (43, 47). Researchers first reported hybridization between *X. malinche* and *X. birchmanni* in 1997, whereas hybrids were not detected when sampling the same stream reaches a decade earlier (48, 49). Meanwhile, the period of 1980–1995 saw a 37% increase in human population in the state of Hidalgo (50). Independent genetic approaches have estimated that these hybrid zones are on the order of ~100 generations old (51), consistent with hybridization beginning in the late 1900s. This recent onset of hybridization raises the question of what triggered it, and whether it was tied to the concurrent socio-ecological transformation of the region.

Though we lack data from these streams prior to the start of hybridization, we can still study the environmental factors which affect hybridization rates by observing spatial patterns in present day populations. The genetic structure in most hybrid populations between *X. malinche* and *X. birchmanni* is best described as a hybrid swarm lacking population structure (43). One exception to this pattern is a population just upstream of the town of Calnali, Hidalgo. There, genetic studies have described two subpopulations composed of *malinche*-like and *birchmanni*-like admixed fish that exist in sympatry and co-occur at small spatial scales (Fig. 1) (52). The long-term history of hybridization between these populations is uncertain, but their observed coexistence and partial admixture is consistent with some level of past gene flow, possibly counteracted by selection against hybrids (53). Sequencing over multiple years showed that this bimodal population structure was stable as early as 2003 and is driven by strong assortative mating between individuals of the same ancestry group (52). However, recent sampling showed that population structure disappears just downstream of the town of Calnali (44), raising the possibility that assortative mating breaks down after exposure to a point pollution source.

Here, we synthesize biological, geographic, and water chemistry datasets to assess the relationship between environmental conditions and patterns of hybridization across multiple *X. malinche* × *X. birchmanni* hybrid zones in Hidalgo, Mexico (Fig. 2). We use low-coverage whole-genome sequencing of 2620 fish to survey hybrid ancestry in four demographically independent streams and confirm the existence of a dramatic collapse of population structure around relatively urbanized areas within the Río Calnali, a pattern which is not replicated in other drainages. We then use mother-embryo sequencing in the Río Calnali to confirm that assortative mating by ancestry is weakened downstream of the urbanized area. Next, we document environmental changes which spatially coincide with the unique loss of reproductive isolation within the Río Calnali. Using land use classification of satellite imagery, we confirm that changes in population structure downstream on the Río Calnali are coupled with a high density of built infrastructure in close proximity to the stream. We also find that population structure in the Río Calnali breaks down at the point where we identify unique shifts in the stream's physical chemistry, organic and inorganic nutrient loading, and metal concentrations. Finally, given the known importance of olfactory communication in swordtail mate choice, we assess olfactory epithelial damage as a potential mechanism linking environmental change to hybridization. We test for variation in the morphology of olfactory rosettes along the Río Calnali, as well as evidence of histological changes after laboratory exposure to humic acid, copper, and ammonia. While we observe no effect of short-term chemical exposure on olfactory histology in the laboratory, we find evidence of greater histological damage in samples from polluted downstream sites compared to less disturbed upstream sites. This work thus explores potential links between environment, phenotype, and genomics in an anthropogenic hybrid zone, deepening our understanding of human impacts on biodiversity.

Results

Population structure across streams

Ancestry structure varied markedly among the four streams sampled in this study. One stream, the Pochula, showed a relatively smooth cline in ancestry from pure *X. malinche* at higher elevations to *X. birchmanni*-like hybrids at lower elevations. The other three streams varied in the degree of population structure, with at least one site in the Calnali, Huazalingo, and Conzintla showing significant departures from unimodality in the distribution of individual ancestry proportions (Fig. 3; Hartigan's Dip Test $P < 0.0001$). Examination of the variation in individual ancestry in these populations supported the presence of two subpopulations with distinct genome-wide ancestry.

Though three streams showed sites with bimodal population structure, we found that the extent of this structure differed dramatically across drainages. In the Río Conzintla, we observed sympatry between nearly-pure *X. malinche* and *X. birchmanni* at two sites separated by 3.7 stream kilometers (mean ± standard deviation minor parent ancestry 5.6 ± 3.1% at Xochicoatlán, 10.6 ± 4.5% at Mixtla), with no recent-generation hybrids detected. Downstream of these sympatric sites, the *X. malinche* cluster disappeared and left a single *X. birchmanni* ancestry cluster (Fig. 3; Table S4), whose ancestry fraction was stable across all contiguous downstream sites (Kolmogorov-Smirnov Test $P > 0.05$; Fig. 3). Combined with our observation of only 1 recent hybrid out of 239 individuals, this suggested that gene flow between ancestry groups in this stream is extremely limited. In the Río Huazalingo, the presence of two subpopulations was only detected at a site directly downstream of a waterfall separating pure *X. malinche* from

181 admixed *X. birchmanni*. *X. malinche*-like individuals were detected up to 0.91 km downstream of
182 the waterfall, but this pattern varied between sampling seasons, hinting that the *X. malinche*
183 individuals may not persist there (Supp. Info. 1; Fig. S1).

184 By contrast, in the Río Calnali, we observed a dramatic collapse in population structure
185 centered on the town of Calnali (Fig. 3). Sites upstream of the town, spanning 3.15 stream
186 kilometers, showed strong departure from unimodality in their ancestry distributions (D = 0.12 –
187 0.21, P < 0.00001 for all sites; Table S4). *X. malinche*-like and *X. birchmanni*-like subpopulations
188 co-existed in sympatry across these sites, but sites downstream of the town plaza showed
189 evidence of a unimodal distribution (D = 0.01 – 0.07, P > 0.18 across all sites; Table S4), with
190 intermediate ancestry and increased variance in individual ancestry proportion. Intriguingly,
191 average *X. malinche* ancestry increased downstream of the town of Calnali (Fig. 3), in contrast to
192 expectations given the elevational distribution of *X. malinche* populations in other streams.
193 Sequencing of four tributaries connected to this reach of the Calnali showed that each hosted a
194 single ancestry cluster, with three composed of *X. malinche*-like fish (Fig. S2). The shift towards
195 *X. malinche* ancestry downstream of these tributaries may therefore be a result of propagule
196 pressure.

197

198 *Strength of ancestry-assortative mating in the Calnali Low and Aguazarca hybrid populations*

199

200 In the upstream Calnali Mid hybrid population on the Río Calnali, we previously
201 documented bimodal ancestry structure and near-complete assortative mating by ancestry (52).
202 By contrast, the Calnali Low population does not show evidence of bimodal ancestry structure,
203 although variance in ancestry is high (Fig. 3). We used paired mother-embryo sequencing to

evaluate whether mating patterns differed from expectations under random mating with respect to ancestry. Despite the dramatic breakdown in population structure, we found that mothers and offspring were less different in ancestry than expected under simulated random mating in both upstream and downstream populations ($P < 0.001$ by simulation; Fig. 4A–B). However, the deviation from neutral expectations was greater at Calnali Mid than at Calnali Low (mean 0.0655 vs 0.0257, *t*-test $P = 0.0483$). This suggested that assortative mating by ancestry is weaker in the Calnali Low hybrid population.

As such, we sought to quantify the strength of ancestry-assortative mating in the Calnali Low population and compare it to the upstream Calnali Mid population. We used an approximate Bayesian computation approach to ask what strength of ancestry-assortative mating was consistent with the average mother-offspring ancestry difference in each population (see Methods). Based on accepted simulations, we recovered a well-resolved posterior distribution of the strength of ancestry-assortative mating ($P_{\text{assortative}}$), and estimated the maximum a posteriori (MAP) for Calnali Low to be 0.68 (95% CI 0.20–0.82; Fig. 4C), substantially weaker than estimates from Calnali Mid (MAP = 0.97, 95% CI 0.79–0.99). A direct comparison of the accepted simulations confirmed that assortative mating was significantly stronger in Calnali Mid (Wilcoxon signed rank test $P < 2.2e\text{-}16$), with a MAP for the estimated difference in the strength of assortative mating of 0.27 ($P_{\text{assortative}}$ 95% CI 0.08–0.72). Thus, our results suggested that weaker assortative mating contributes to the breakdown in population structure in the Calnali Low hybrid population.

Land use across drainages

Land use quantification showed that human impacts on the Río Calnali watershed were higher than other streams. The reaches where the stream passed through the town of Calnali had the highest proportion of developed land in the study area, with increased levels of urbanization centered on the location of genetic population structure collapse (Fig. 5). When calculating the cumulative watershed land input of a given point, the downstream sites on the Río Calnali had the highest proportions of developed land in the study area (Fig. 5B), especially when considering land within a short distance of the stream (Fig. 5E). Associations between cleared land (vegetation, with the exclusion of forest) and population structure within the Río Calnali were less clear (Fig. S3), but the downstream section of the Río Calnali did show the highest levels of cumulative cleared area within a short distance of the stream among all reaches surveyed (Fig. S3F, S3H). Overall, our findings suggested that some degree of deforestation and development is ubiquitous throughout the Atlapexco drainage, but the level of built infrastructure was especially high in the Calnali subcatchment.

Water chemistry variation

Water chemistry varied dramatically both between streams and between sites on the Río Calnali. Principal component analysis demonstrated that most variation in water quality could be summarized by two axes: one that largely separated the sites by stream (PC1), and another separating the sites upstream of the town of Calnali from the other streams and those downstream of Calnali (PC2; Fig. 6). Across streams, there was variation in conductivity, alkalinity, hardness, and pH, with sites in the Río Conzintla having the highest values of each of these metrics and sites along the Río Calnali having the lowest (Fig. 6A; Fig. S4). Sites

downstream of the town of Calnali were associated with increased dissolved organic matter, turbidity, ammonia, and nitrite, as well as reduced dissolved oxygen, all consistent with increased anthropogenic impacts (Fig. 6A). Statistical tests indicated that levels of turbidity, DOM, nitrite, and ammonia were all significantly elevated in the sites downstream on the Río Calnali relative to the upstream sites and to other streams (Fig. 6C–D, Table S6).

Turning to the concentration of metal ions measured by ICP-MS, a principal component analysis showed that concentrations of many ions were highest in the Conzintla and lowest in the Calnali (Fig. 6B; Fig. S5), potentially due to hydrological and geological variation (Supp. Info. 2, Fig. S6–7). The transition from the sites upstream to downstream of the town of Calnali was also associated with a dramatic increase in the concentration of numerous ions, especially major industrial metals (e.g. iron, aluminum, copper, lead, manganese; Fig. 6B). Multiple metals significantly increased in concentration downstream of the town of Calnali when individually tested, including copper, lead, cadmium, aluminum, and zinc (Kruskal Wallis $P < 0.001$; Fig. 6E; Fig. S5). On the other hand, other ions with known effects on fish neurobiology or olfaction showed similar or higher concentration in the Conzintla than in the Calnali downstream sites, including manganese, arsenic, and calcium (Supp. Info. 2; Fig. S5). We also found some evidence for seasonal fluctuations in metal concentrations, though we lack sufficient sampling to formally analyze these effects (Supp. Info. 3; Fig. S8–9).

Olfactory disruption as a function of water chemistry

Our chemistry measurements showed that fish in downstream sites on the Río Calnali experienced elevated levels of a range of compounds that may impact olfactory function. We saw

limited evidence for gross bioconcentration of these compounds in ICP-MS analysis of whole fish (Supp. Info. 4; Fig. S10), and thus focused on potential effects of water chemistry on the sensory epithelial surface. Specifically, we evaluated evidence for histological changes in the olfactory rosettes of wild caught fish from an upstream site, Aguazarca, and a downstream site, Calnali Low. H&E staining allowed us to observe the motile and sensory cilia which may be lost in the face of chemical exposure (54–56). We found marginally lower proportions of ciliated surface area on the olfactory epithelium at the Calnali Low site (Mann-Whitney Test $P = 0.08$; Fig. 7C). Likewise, AB/PAS staining clearly distinguished goblet cells through the deep blue staining of the protective mucoproteins they produce, and revealed significantly higher densities of goblet cells at Calnali Low (Mann-Whitney Test $P = 0.003$; Fig. 7A–B, 7D), consistent with a compensatory response to shield the olfactory epithelium from toxicants. In contrast to the differences observed in the wild, 96 hours of laboratory exposure to ecologically relevant levels of ammonia, copper, humic acid, or their combination yielded no such differences in ciliary surface (Kruskal-Wallis $P = 0.166$) or goblet cell density (Kruskal-Wallis $P = 0.406$) in *X. birchmanni* (Fig. 7E–F). Both histological metrics were comparable across all laboratory treatments to the values observed in the upstream Aguazarca population (Fig. 7C–F).

Discussion

With a fine-scale view of the genetic and environmental landscape of hybrid zones, we can move past a binary picture of hybridization's occurrence to assess the specific changes and mechanisms driving anthropogenic hybridization. Here, we explore spatial covariation in population structure, assortative mating, and environment as a proxy for the changes that may have driven initial hybridization between *X. birchmanni* and *X. malinche*. We then use targeted analyses within the Río Calnali to test the plausibility of one hypothesized driver: the disruption of olfactory-based mate choice by chemical pollution from human development. Although our results are primarily based on correlations with spatially varying environmental variables, they are consistent with this hypothesis, and lay the foundations for further manipulative studies.

By surveying genome-wide ancestry distributions from thousands of samples across dozens of sites, we document the outcomes of the complex interactions of migration, ecological selection, and mate choice in structuring hybrid zones. Migration played a major role in structuring ancestry in all drainages, with waterfalls and rapids isolating near-pure *X. malinche* populations upstream in the Ríos Pochula and Huazalingo, and shifts in ancestry distributions on either side of subterranean stream reaches in the Ríos Calnali and Conzintla (Fig. 1, 3). Though we found some degree of gene flow between *X. birchmanni* and *X. malinche* in all four streams, the amount and spatial distribution of admixture differed dramatically between streams (Fig. 3). At one extreme, the Río Conzintla showed two ancestry clusters with limited admixture across multiple sites. The functional consequences of this restricted admixture may be limited by genome-wide selection against introgression (43), and populations with similar admixture rates have been identified as warranting conservation in other cases of anthropogenic hybridization

(57). The stable Conzintla hybrid zone thus serves as a contrast to other streams, and comparisons in water quality may illuminate the potential drivers of breakdown in assortative mating in other contexts.

The Río Huazalingo and Río Pochula are both intermediate in water chemistry to the Río Conzintla and the Río Calnali, but show divergent ancestry patterns. The Huazalingo, like the Conzintla, has a zone of sympatry between two distinct ancestry clusters, but in the Huazalingo this zone is temporally unstable (Supp. Info. 1), lower in elevation (769 vs. 1020 m; Table S1), and limited to the area immediately downstream of a waterfall. This pattern could be explained by a combination of migration barriers and ecological selection, with *X. birchmanni*-like individuals prevented from migrating upstream by the waterfall, and *X. malinche*-like individuals outcompeted when passing below it. In contrast, the Río Pochula hosted near-pure *X. malinche* at even lower elevations (522 m; Table S1), but no sites with bimodal ancestry structure. Rather, this stream appeared more similar to classic clinal hybrid zones, where ancestry patterns are shaped by the countervailing effects of gene flow and selection against hybrids (58).

Why might rivers with similar water chemistry differ in population structure? Potential explanations for the lack of population structure in the Pochula might hinge on its relatively large watershed area and thus high stream volume (Fig. S6) at the point of interspecific contact. The attendant differences in swordtail habitat availability, population densities, and signaling environment might alter pre-mating isolation, as both demography (7) and individual condition (59) are known to affect hybridization rates. Alternatively, past anthropogenic impacts may have caused a collapse of population structure, which persisted beyond the disturbance due to a loss of ancestry-assortative mating in admixed individuals (60–62). The diversity of population structures we observed across these watersheds is consistent with numerous variables impacting

338 hybridization outcomes, as expected from the multitude of factors known to affect mate choice
339 and hybrid fitness (6–11, 13, 24). That said, similar surveys of additional streams may provide
340 the necessary contrasts to distinguish among some of these potential drivers.

341 The dramatic changes in ancestry structure in the Río Calnali from upstream to
342 downstream allow us to ask more direct questions about the relationship between environmental
343 factors and population structure. We observed strong bimodality in genome-wide ancestry at sites
344 upstream of the town of Calnali, with individuals falling into an *X. malinche*-like ancestry cluster
345 and an *X. birchmanni*-like cluster. These results align with prior work documenting the presence
346 of strong assortative mating by ancestry within ancestry clusters at the Aguazarca site on the Río
347 Calnali (52). In the less than two kilometers where the stream traverses the town of Calnali, this
348 bimodal population structure collapses into a hybrid swarm, with observed admixture
349 proportions spanning those of the upstream clusters (Fig. 3).

350 Likewise, mother-embryo sequencing and simulations demonstrated that assortative
351 mating is substantially weakened, but not entirely absent, at downstream sites on the Río Calnali
352 (Fig. 4). Ongoing assortative mating could be driven by some combination of downstream
353 migration of pregnant mothers, variable impacts of pollution on different sensory pathways (e.g.
354 visual vs. olfactory cues) (63, 64), or fluctuations in sensory disruption as a result of variation in
355 environmental conditions (Supp. Info. 3). Regardless of the precise drivers, our findings support
356 theoretical predictions that even modest reductions in the strength of assortative mating can
357 result in the emergence of hybrid swarms (26). The Río Calnali thus provides an opportunity to
358 study the environmental determinants of reproductive isolation through comparisons within and
359 between streams.

360

We next confirmed that anthropogenic impacts vary over space within our study area. As expected, the Calnali drainage was unique both in the scale of built infrastructure relative to catchment area, as well as the proximity of development to the stream (Fig. 5). Runoff from agricultural lands could also contribute to the chemical and biological variation we observed, but may be a less likely explanation given the relatively small differences in agricultural land area within and between drainages (Fig. S3). We then identified stream-specific water chemistry signatures, which we speculate may be driven by geology and mining impacts in the Conzintla drainage (Supp. Info. 2; Fig. S7), as well as orthogonal chemical changes between sites on the Río Calnali above and below the town of Calnali (Fig. 6). Both agricultural and urban development have been linked to some of the changes in water chemistry that we observe in the downstream Río Calnali (65–69). In particular, many metals whose concentrations change along the course of the Río Calnali have been previously associated with both domestic wastewater and runoff from roads (67).

Among the compounds that varied spatially, a substantial number have been previously shown to affect fish olfaction (19, 70, 71) or neurobiology (72–74). Many of these parameters were especially elevated in the areas downstream of the town of Calnali, and thus are potential candidates for the drivers of ancestry structure breakdown in this stream. Turbidity also increased in downstream Calnali sites, and though interspecific mate discrimination in these species is thought to be primarily olfactory (75, 76), a disruption of visual preference could nonetheless contribute to hybridization (77). In contrast, some ions with documented olfactory or neurological effects were most concentrated in the Conzintla (Fig. S5) (23, 78–80). This highlights the need both for ecotoxicological studies in *Xiphophorus* to establish species-specific sensitivity (i.e. EC_{50} values), and for careful consideration of how the total chemical environment

may modify the effects of individual compounds. For example, variation in pH between streams may generate interaction effects, as low pH increases metal bioavailability and toxicity (Fig. S4) (70).

Having established differences in both the degree of population structure and in water chemistry between sites in the Río Calnali, we explored the loss of olfaction-based assortative mate preferences as a mechanism which might connect the two. Our histological analysis of fishes in the upstream and downstream Calnali showed changes in morphology downstream consistent with olfactory damage (Fig. 7A–D). The loss of cilia in the sensory epithelium has previously been observed after exposure to metals and anthropogenic hydrocarbons (81, 82), and could directly reduce olfactory sensitivity by disrupting water flow through the nares (83, 84) or the function of olfactory sensory neurons (85). Likewise, increased goblet cell densities have been linked to nasal irritation in other systems, and may protect epithelia from noxious chemical exposure (86–88). By showing changes in olfactory structure *in situ*, this work complements prior *ex situ* experiments showing that water chemistry manipulations can alter assortative olfactory preferences in *X. birchmanni* (19, 23).

However, our short-term laboratory exposures of *X. birchmanni* to ecologically relevant levels of ammonia, copper, humic acid, or their combination did not generate the histological differences seen *in situ* (Fig. 7E–F). The effects seen in wild-collected fish may thus be dependent on the cumulative and interactive effects of numerous chemicals, exposure for longer periods, or exposure at a more sensitive developmental stage (89–91). Definitively linking the observed histological differences to the chemical environment, rather than a covarying biotic factor (e.g. pathogen exposure) (92), will require additional evidence from inter-stream comparisons and experiments. Likewise, whether these histological changes themselves weaken

assortative mating, or are correlated with other causative changes (e.g. neural accumulation of toxicants (93), water chemistry effects on signal transduction (22), individual condition (59, 94), or conspecific encounter rates (7)) is an exciting direction for future work.

Taken as a whole, our study presents an integrative window into the environmental and organismal drivers of hybridization between *X. birchmanni* and *X. malinche*. By showing that dramatic water chemistry differences coincided with changes in population structure, we support the relevance of prior behavioral work showing the disruption of assortative mating in these species following water chemistry changes (19, 23). It remains to be seen whether reproductive isolation might be re-established between these species through a combination of habitat restoration, immigration (Supp. Info. 1) and natural selection against hybrids, as has been observed in other cases of anthropogenic hybridization (95). Though many studies have documented a broad connection between environmental conditions and hybridization in freshwater fishes (5, 24), our analyses of assortative mating and olfactory histology provide a deeper understanding of proximal mechanisms by which water chemistry changes might disrupt reproductive isolation on small spatiotemporal scales. Further characterizing the drivers of hybridization will both grow our understanding of the processes which generate biodiversity, and enable improved management of unintended anthropogenic impacts.

Resource Availability

Raw sequencing reads used in this project are available under NCBI SRA Bioprojects PRJNA1346846, PRJNA1305547, PRJNA744894, PRJNA930165, and PRJNA610049. All other datasets necessary to recreate the results of the publication are available on Dryad

(https://doi.org/10.5061/dryad.nvx0k6f5h). All new customs scripts used to generate results are available on Github at https://github.com/benmoran11/anthro_xipho_hybrids and https://github.com/Schumerlab/Lab_shared_scripts.

Author Contributions

Conceptualization, B.M.M., C.M.R., M.S., and G.G.R.; Investigation, B.M.M., W.F.R.-D., D.L.P., T.T.L.Y., T.R.G., G.I.J.-R., C.Y.P., E.N.K.I., G.A.P., S.M.B., A.E.D., R.S., and J.J.B.; Software, B.M.M. and M.S.; Formal analysis, B.M.M.; Resources, C.M.R., M.S., and G.G.R.; Writing original draft, B.M.M. and M.S.; Writing — review and editing, B.M.M., W.F.R.-D., D.L.P., G.I.J.-R., E.N.K.I, G.A.P., S.M.B., G.M.V.A., C.G.-R., C.M.R, M.S., and G.G.R.; Supervision, G.M.V.A. and C.G.-R.; Funding acquisition, C.M.R., M.S., and G.G.R.; Project administration, G.M.V.A.

Acknowledgements

The authors thank members of the Schumer and Rosenthal laboratories for helpful discussion and feedback on earlier versions of this manuscript. We thank the Federal Government of Mexico for permission to collect fish (Permiso de Pesca de Fomento no. PPF/DGOPA-064/20). Stanford University and the Stanford Research Computing Center provided computational support for this project. We thank Dra. Susana Saval Bohórquez of the UNAM Environmental Engineering Laboratory and Dr. Guangchao Li and Douglas Turner of the Stanford Environmental Measurements Facility for technical and experimental support. We are deeply grateful to the delegates and landowners of the Calnali region for their engagement in our work

and for sharing access to their communities' waterways. This work was supported by a Knight–Hennessy Scholars fellowship and NSF GRFP 2019273798 to B.M.M., a CONACyT fellowship to G.I.J., NSF Awards 1723266, 1755327 and 1354172 and a grant from the Fondazione Cariparo to G.G.R., and Human Frontiers in Science Grant RGY0081 to M.S. & C.M.R.

Declaration of Interests

The authors declare no conflicts of interest related to this work.

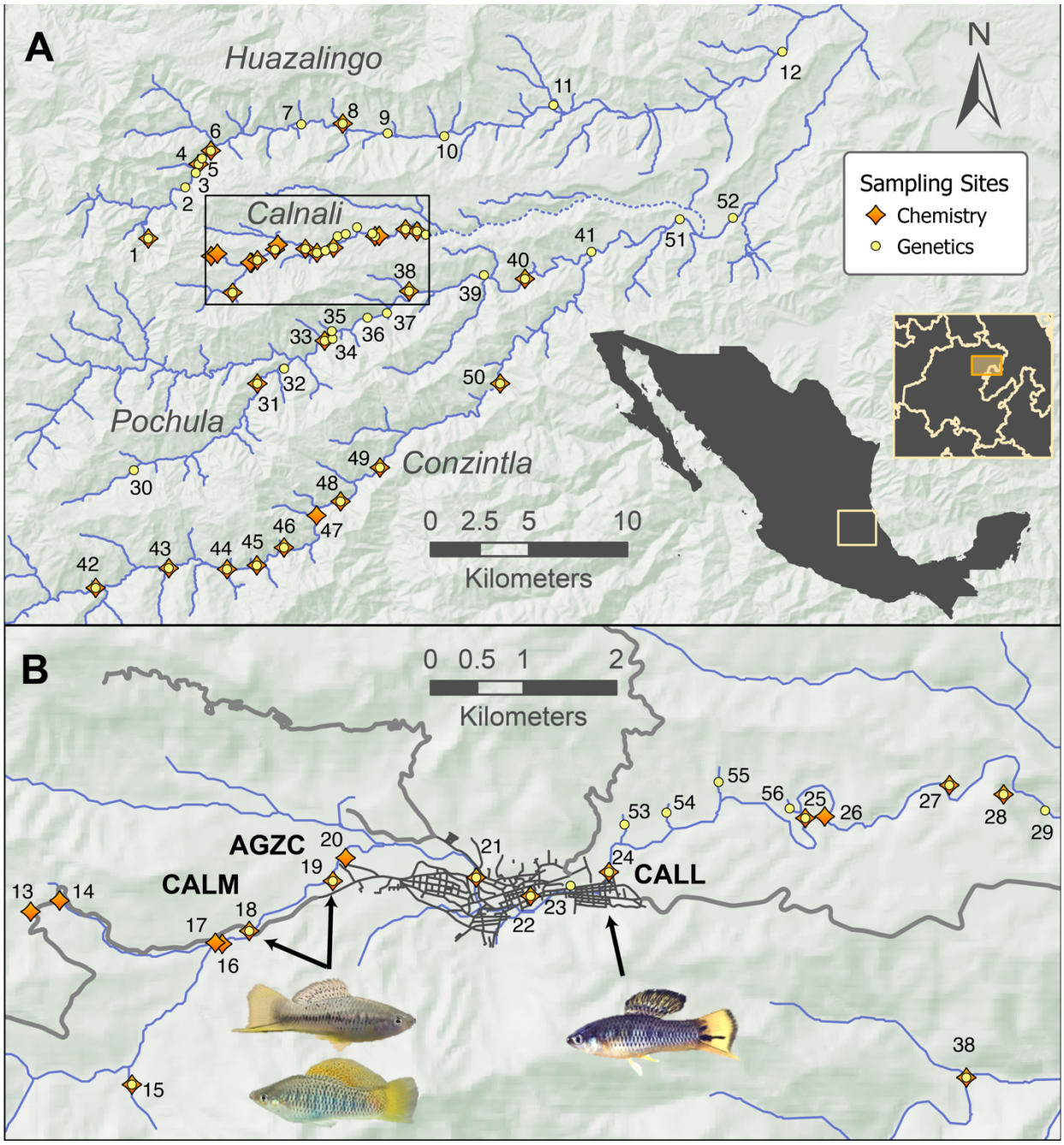

Figure 1. Study area and sampling sites. **A)** Overview of Río Atlapexco basin, highlighted in orange within the inset Mexican state map, whose area is indicated in yellow on the gray outline of Mexico. Streams are shown as blue lines, seasonally dry subterranean reaches are dashed, the four major streams studied are labelled, sites where fish were collected are yellow circles, and sites where water chemistry data were collected are orange diamonds. The black box encloses the

area displayed in panel **B**. **B)** Sites sampled on the Río Calnali. Gray lines show paved roads, and black lines show streets in the town of Calnali. Images show representative male *Xiphophorus* fishes with *X. malinche*-like (top left), *X. birchmanni*-like (bottom left) and admixed (right) phenotypes as observed in three populations on the Río Calnali (AGZC = Aguazarca, CALM = Calnali Mid, CALL = Calnali Low). These sites were the locations used for sample collection for mother-embryo sequencing (CALM and CALL) and histology (AGZC and CALL).

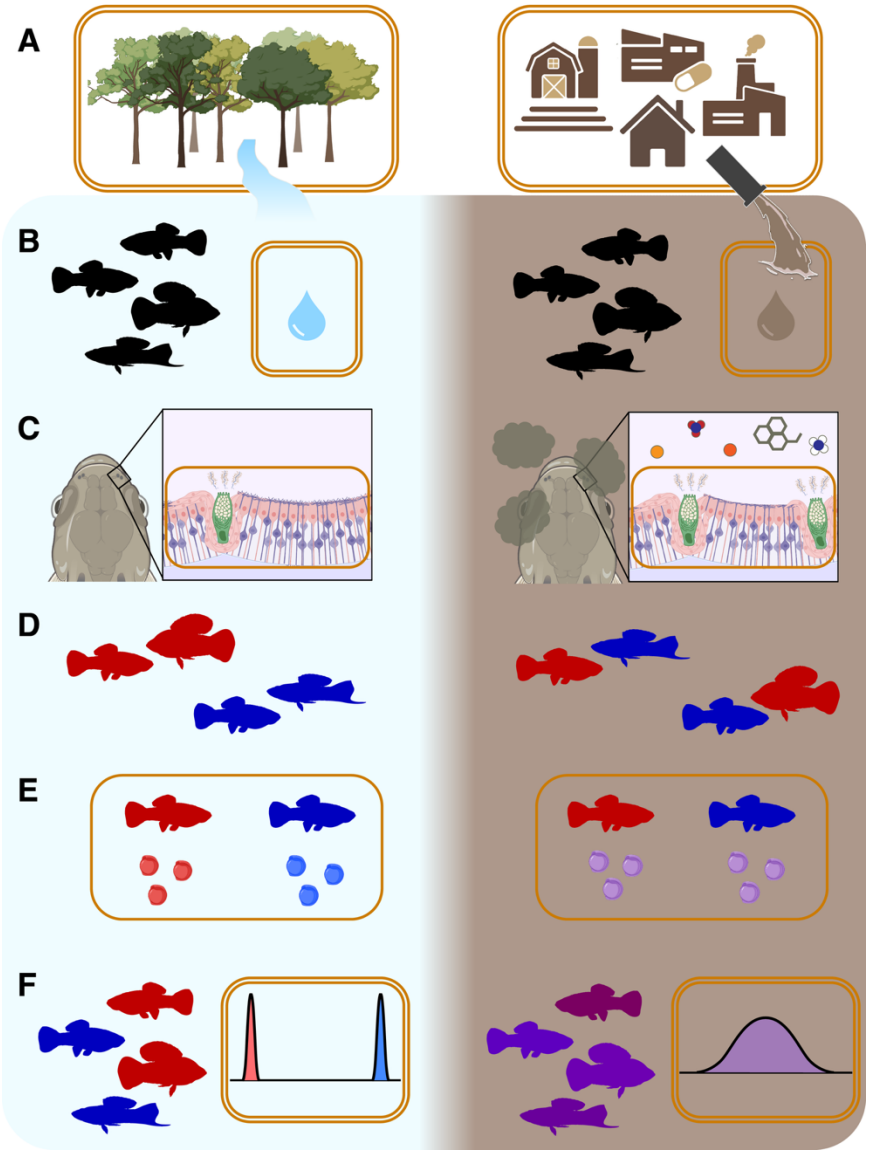

Figure 2. Overview of hypothesized mechanisms connecting human development to swordtail hybridization. Orange boxes represent aspects observed in this study, with double boxes measured across all four streams, and single boxes measured only within the Río Calnali. **A)** Levels of anthropogenic development differ across space in the Río Atlapexco drainage, leading to differential runoff which creates **B)** novel variation in chemical environment within and between rivers. **C)** Environmental change affects sensory biology and communication, **D)** attenuating preferences for mates of similar ancestry, and leading to **E)** decreased assortative

482 mating by ancestry and **F)** the collapse of subpopulations into hybrid swarms with unimodal

483 ancestry distributions. Figure created with BioRender.

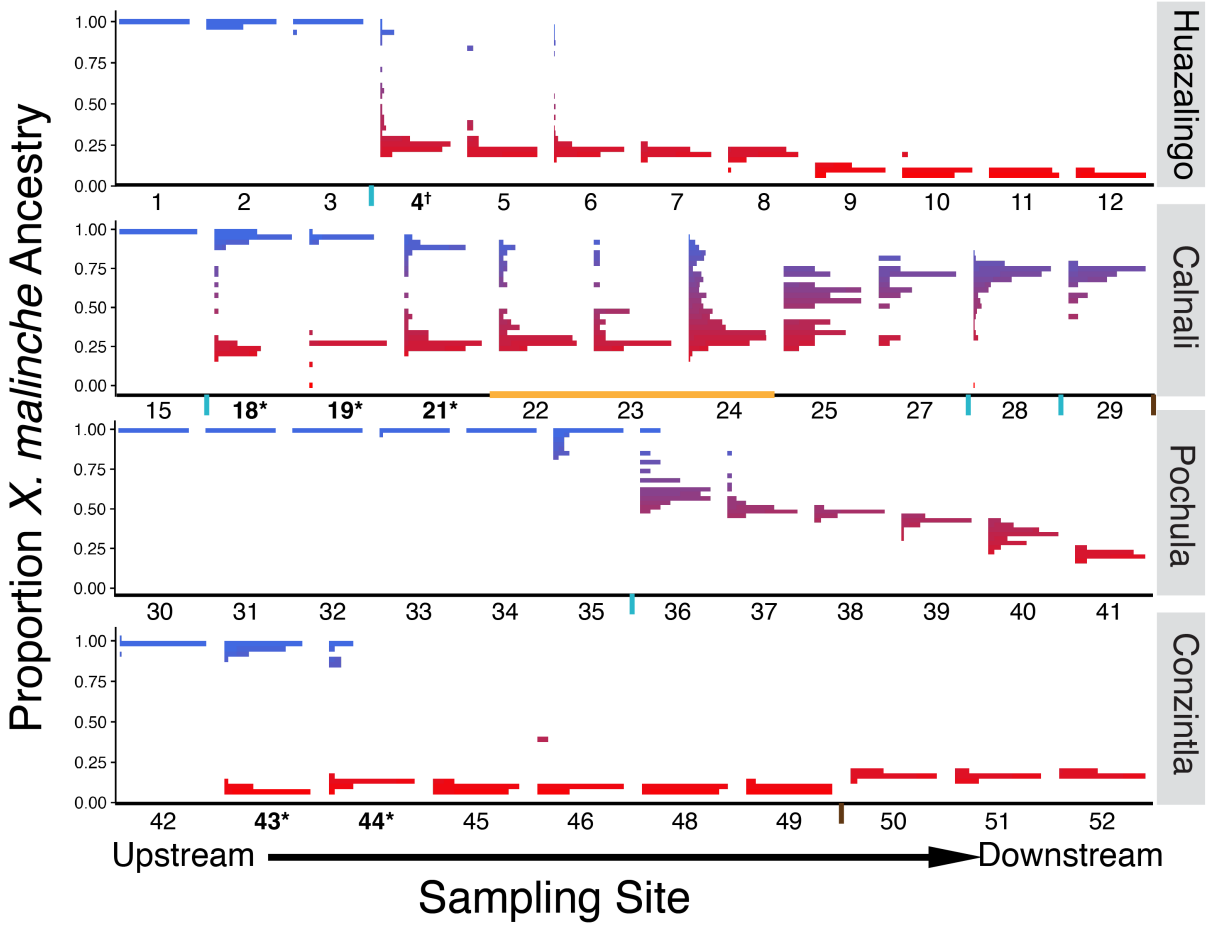

Figure 3. Genetic ancestry results from *X. malinche* × *X. birchmanni* hybrids in the Río Atlapexco Drainage. Histograms show ancestry distributions at sampling locations along four streams. Sites are arranged with upstream sites on the left side of the X-axis, and downstream sites on the right. Y-axis corresponds to the proportion of genome-wide ancestry derived from *X. malinche* among individuals in that population (1 = pure *X. malinche*, 0 = pure *X. birchmanni*), and the width of bars indicates the count of individuals in that ancestry bin (sample sizes per population in Table S4). X-axis text shows site numbers, as in Fig. 1. Bolded X-axis numbers indicate sites with significant deviations from a unimodal ancestry distribution, either across all sampling timepoints (asterisk; Table S4) or at a subset of sampling times (dagger, Supp. Info. 1). Orange segment on the Río Calnali transect denotes the sites located within the town of Calnali.

X-axis ticks denote likely migration barriers between sites (blue = dams, waterfalls, and rapids; brown = subterranean stream reaches).

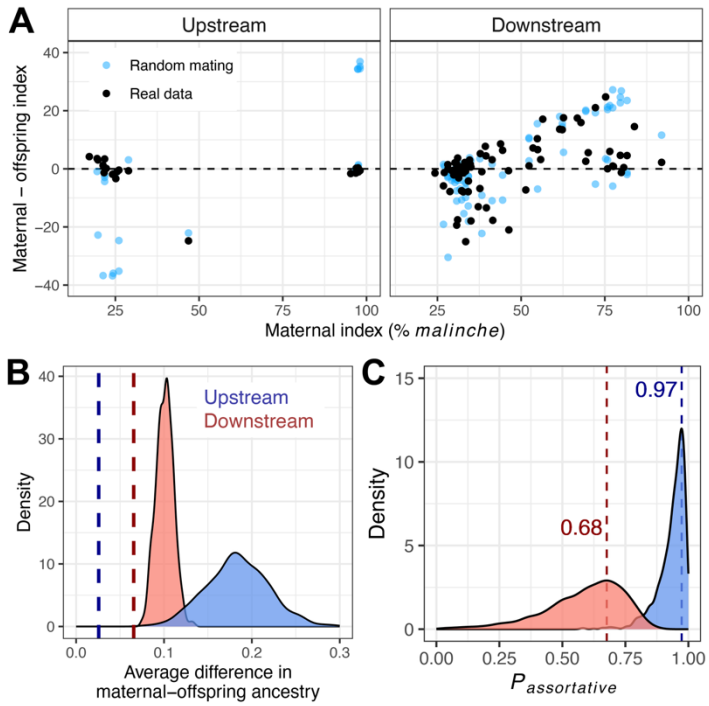

Figure 4. Mating patterns in fish upstream and downstream of the town of Calnali. **A)** Mother-embryo ancestry from upstream (Calnali Mid) and downstream (Calnali Low) of the town of Calnali. X-axis shows the proportion of each mother's genome derived from *X. malinche*, and Y-axis shows the difference in genome-wide ancestry between each mother and embryo. Black points are observed values, blue point are a simulated sample set under random mating. **B)** Observed mother-embryo ancestry differences diverge from random mating expectations both downstream (red) and upstream (blue) of the town of Calnali. Density curves show the distribution of average mother-embryo ancestry difference across 1000 simulations of random mating in each population, and dashed lines show the observed average mother-embryo ancestry difference. Mean ancestry difference was significantly lower than expected under random mating for both populations, consistent with assortative mating by ancestry ($P < 0.001$). **C)** Inferred strength of assortative mating from observed maternal-offspring ancestry distributions. Density curves depict the simulated probability of assortative mating ($P_{assortative}$) in accepted simulations

511 for each population, with 0 representing random mating. Dashed line denotes maximum *a*

512 *posteriori* estimates (Calnali Low = 0.68, Calnali Mid = 0.97).

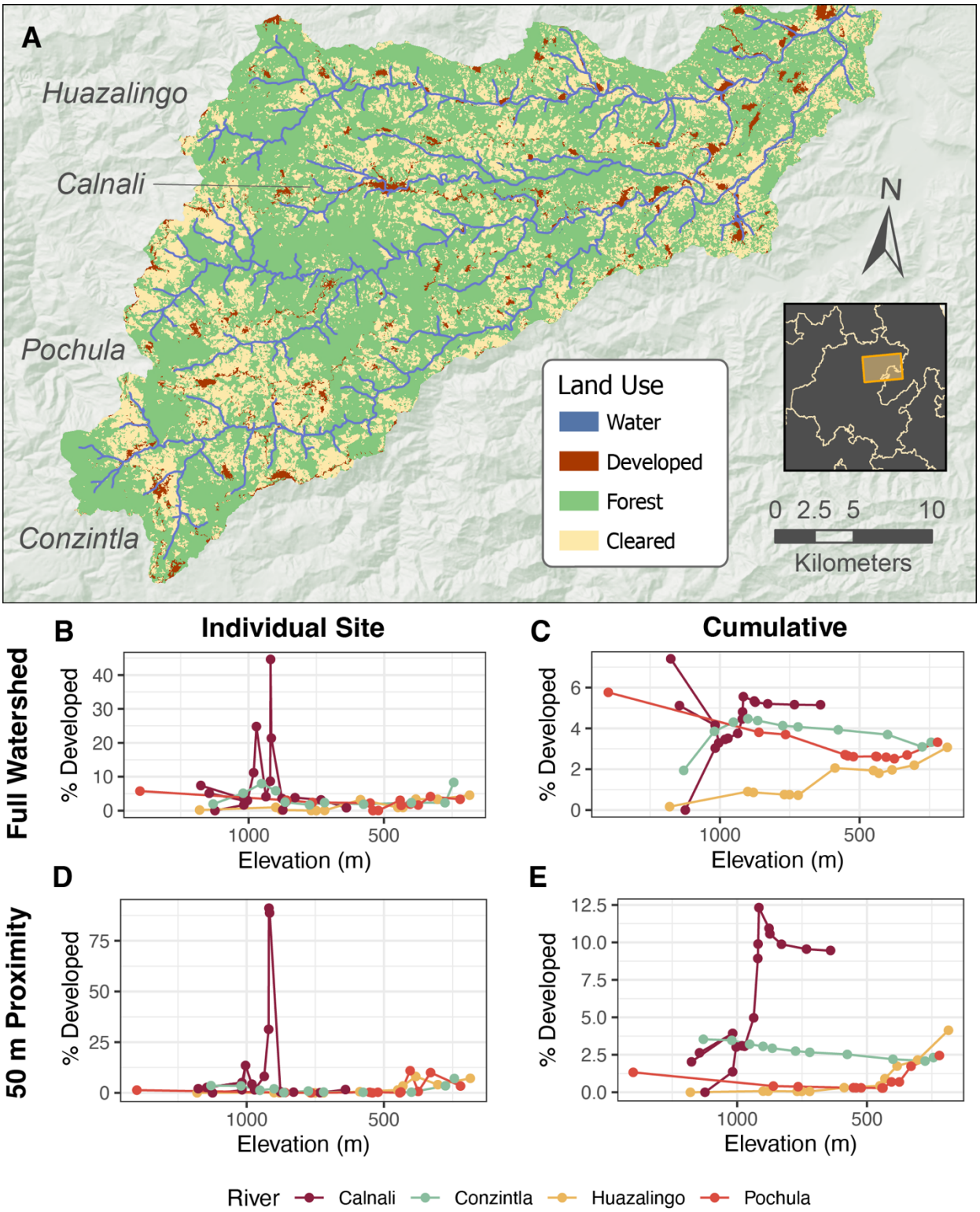

Figure 5. Results of land use classification analysis in the Río Atlapexco basin. **A**) Map of classification results from 2020–2023 hyperspectral imagery. 10 m^2 pixels were classified as

developed (buildings, mines, and roads), cleared land (grassland, pasture, or cultivated crops) forest (continuous tree cover, excluding plantations), or water by an SVM algorithm, with training polygons identified from 3 m^2-resolution 2022 imagery from Planet Labs (96). Stream polygons are shown as blue lines over classified pixels. **B–E)** Percent of land classified as developed within different drainages of the Río Atlapexco basin. Points show the proportion of pixels in each site's subcatchment that were classified as developed. Left column (**B** and **D**) shows the site-wise proportions, or the subcatchment of the section of stream between a site and the closest upstream site. Right column (**C** and **E**) shows the cumulative subcatchment of all sections of the stream upstream of a given site. Top row (**B** and **C**) shows calculations that include pixels of any distance from a stream, while bottom row (**D** and **E**) shows calculations limited to pixels within 50 m of a stream. Color denotes drainage, and lines connect sites in the same stream based on their order. The line corresponding to the Río Calnali branches because multiple headwater tributaries were sampled.

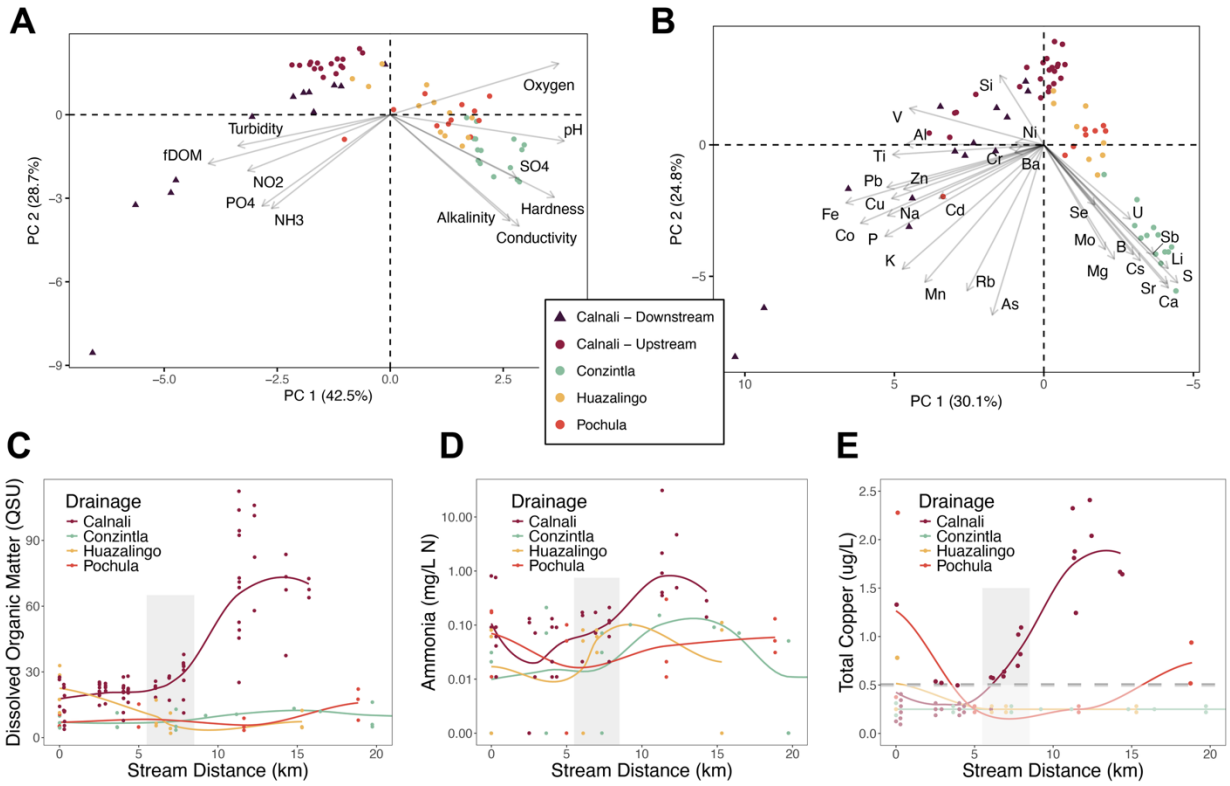

Figure 6. Water chemistry data from four streams in the Río Atlapexco drainage. **A–B)** Principal component analysis (PCA) biplots for **A)** parameters measured using the sonde, turbidimeter, colorimeter, and **B)** parameters measured using ICP-MS. Points represent sampling events, and color and shape denote drainage, with sites on the Río Calnali upstream and downstream of the town of Calnali labelled separately. Labelled arrows represent variable loadings onto first two principal components, with highly correlated variables showing similar vectors. **C–E)** Observations of water chemistry parameters elevated in sites downstream of the town of Calnali, including **C)** fluorescent dissolved organic matter, **D)** ammonia, and **E)** total copper. Grey shaded area denotes the sites located within the town of Calnali on the Río Calnali transect. X-axis indicates distance downstream from the first site sampled on a stream, points indicate individual measurements, and lines show a loess-spline fit of change over the stream course. Note that the Y-axis is log-scaled in the case of ammonia measurements (**D**). Translucent points below the

gray dashed line in **E)** represent measured values below the detection limit of the ICP-MS assay. Points below this limit are plotted at arbitrary Y-values and only represent sample counts. See Table S3 for sample sizes of each parameter.

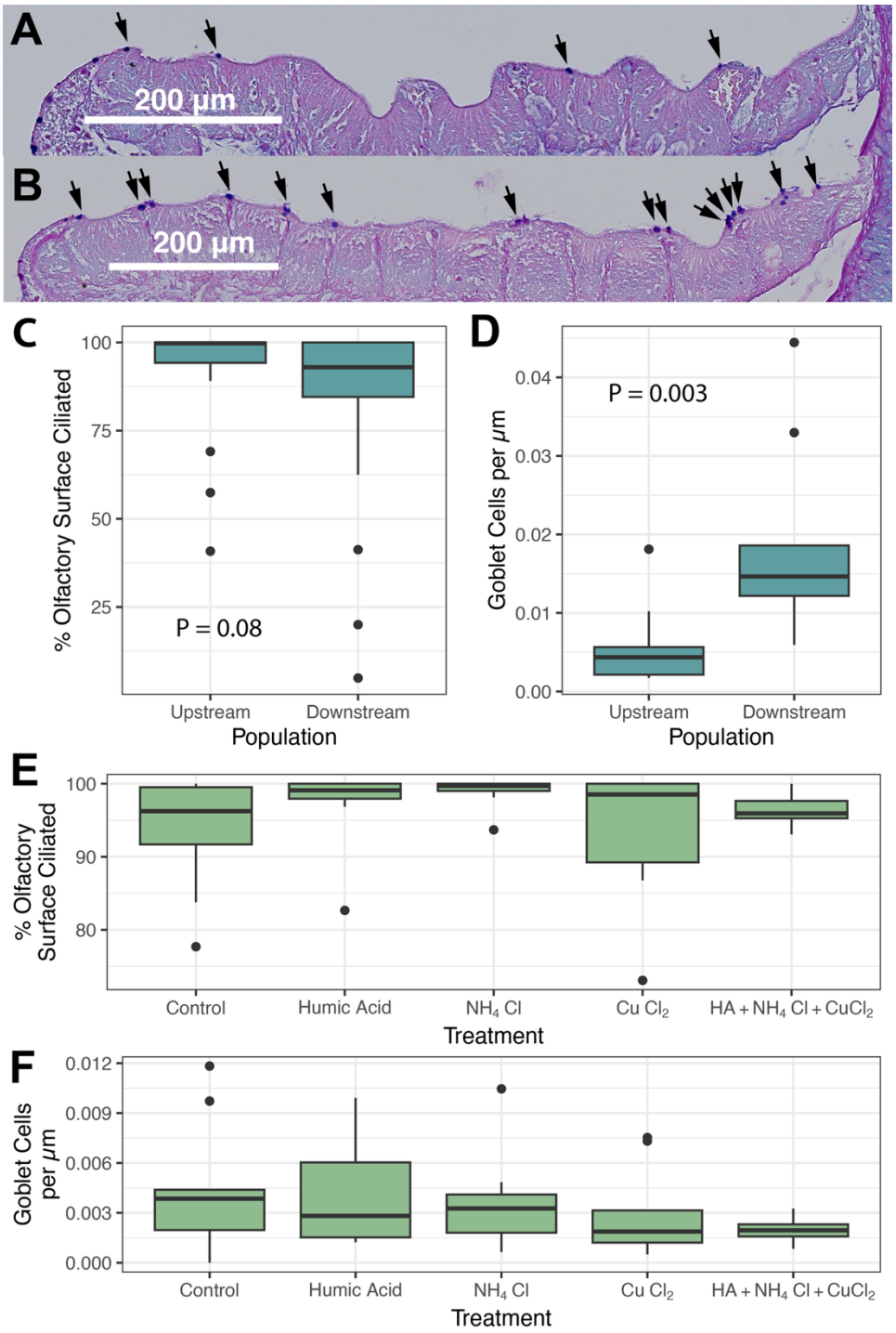

545

546 **Figure 7.** Histological phenotypes in wild-caught and laboratory-exposed fishes. **A–B)**

547 Representative AB/PAS stains of olfactory rosettes of *X. malinche* × *birchmanni* hybrids from **A)**

548 Aguazarca (n = 27 individuals), and **B)** Calnali Low (n = 29). Mucoproteins are stained blue by

549 AB/PAS, eosin counterstain appears as pink. Arrowheads indicate locations of goblet cells, with
550 the pictured individuals exhibiting the median count for each site. **C–D)** Results of olfactory
551 histology of fishes from sites upstream (Aguazarca) and downstream (Calnali Low) of the town
552 of Calnali. Thick lines denote group median, boxes show interquartile range (IQR), and whiskers
553 and points show samples inside and outside 1.5 × IQR, respectively. **C)** Proportion of each fish's
554 sensory epithelium with visible cilia, visualized with H&E staining (upstream n = 27,
555 downstream n = 29). **D)** Number of mucus-producing goblet cells per µm of olfactory rosette
556 surface area, visualized with AB/PAS staining (n = 9 individuals each). P-values indicate results
557 of Mann-Whitney U Test for difference between sites. **E–F)** Results from a laboratory exposure
558 experiment (n = 10 individuals each). Adult *X. birchmanni* were exposed to elevated dissolved
559 organic matter, ammonia, or copper (delivered as humic acid, NH_4Cl, and $CuCl_2$, respectively) or
560 all the above for 96 hours, and compared to control fish with no exposure. **E)** Ciliated surface
561 and **F)** goblet cell density were measured as in **C–D).** Note difference in y-axis scale from **C–D)**.

562 **STAR Methods**

563 ***Experimental model and study participant details***

564 *Xiphophorus* fishes were collected at 48 sites across four stream basins, which together
565 compose the Río Atlapexco drainage of Hidalgo, Mexico (see Table S1 for full list with GPS
566 coordinates, and Table S2 for sample size by year), with permission from the Mexican
567 government and Stanford University animal welfare protocols (Stanford APLAC protocol
568 #33071). Fish were collected using baited minnow traps and anesthetized in a buffered solution
569 of 100 mg/mL MS-222 dissolved in stream water. Fin clips were taken and stored in 95% ethanol
570 for low-coverage whole-genome sequencing, after which fish were allowed to recover then
571 returned to the pool from which they had been sampled. A subset of female fish from the Calnali
572 Mid (n = 22) and Calnali Low (n = 74) sites (Fig. 1) were euthanized and stored in 95% ethanol
573 for later dissection of embryos and analysis of assortative mating (see below). In addition, 30
574 fish each from the Aguazarca and Calnali Low sites were decapitated following euthanasia in
575 May and September 2022, with whole heads preserved in 10% neutral buffered formalin for
576 olfactory histology (see below). Finally, *X. birchmanni* used in laboratory chemical trials were
577 born and raised in the Stanford fish facility (source population Río Coacuilco, 21°5'51.16"N
578 98°35'20.10"W). Fish were late juveniles or adults (>4 month old) before the beginning of
579 experimentation in July and August 2023. Experimental trial groups were balanced by sex, with
580 2 females and 3 males per treatment in July, and 3 females and 2 males per treatment in August.
581 Fish were housed in groups of 5 in 10-gallon tanks on a 12/12 light dark cycle at 22°C and fed
582 twice daily. All individuals were healthy and had not been involved in previous procedures.
583

584 ***Method Details***

585 *Low-coverage whole-genome sequencing*

586

587 DNA was extracted from preserved fin clips using the Agilent DNAdvance extraction kit
588 (Beckman Coulter, Brea, California). The protocol followed the manufacturer's instructions for
589 tissue extraction except that we used halved volumes in all reactions. Extracted DNA was
590 quantified on a BioTek Cytation5 (Agilent, Santa Clara, CA) microplate reader and diluted to 2.5
591 ng/µl for library preparation. We used a previously described tagmentation-based protocol to
592 prepare DNA libraries for low-coverage sequencing (41). We prepared a tagmentation master
593 mix to enzymatically shear diluted DNA using 0.25 µl of TDE1 Tagment DNA enzyme (Illumina
594 no. 20034197), 1.375 µl of TD1 buffer (Illumina no. 20034197), and 1.375 µl of Tris-HCl
595 $MgCl_2$ buffer (20 mM Tris-HCl, 10 mM MgCl2) per sample. We added 3 µl of tagmentation
596 master mix to 2 µl of diluted DNA and incubated at 55°C for 5 min. We prepared a PCR master
597 mix with per-sample volumes of 8.9 µl of OneTaq Hot Start Quick-Load 2X Master Mix (NEB
598 no. M0488) 3.5 µl of nuclease-free water, and 1.2 µl of 10 µM i5 index. We combined 5 µl of
599 tagmented DNA, 1.5 µl of 10 µM i7 index, and 13.5 µl of the PCR master mix per sample and
600 amplified the PCR reaction for 12 cycles. We used custom i7 indexes. PCR products were pooled
601 and purified using 18% SPRI beads. Libraries were quantified on a Qubit fluorometer (Thermo
602 Scientific, Wilmington, DE), and library size distribution was visualized on an Agilent 4200
603 Tapestation (Agilent, Santa Clara, CA). Sequencing was carried out at Weill Cornell Medical
604 College, Harvard Bauer Core, and Admera Health Services (South Plainfield, NJ) on an Illumina
605 HiSeq 2500 (N = 526), HiSeq 4000 (N = 1289), NovaSeq X (N = 221), and NovaSeq X Plus
606 (709). Library formats included 150 bp paired-end reads (N = 660), 75 bp paired-end (N = 691),
607 100 bp single-read (N = 182), and 100 bp paired-end (N = 276). We used downsampling analyses

608 of higher-coverage individuals to confirm that individual variation in coverage and library type
609 could not explain the differences in genome-wide ancestry we observed in our study (Supp. Info.
610 5). The average nominal coverage (base pairs sequenced / *X. birchmanni* genome size) of
611 individuals included post-filtering was 0.65X. Individual-specific information is available in the
612 metadata of the relevant NCBI BioProjects (see Data Availability statement).
613
614 *Water chemistry surveys*
615
616 We chose to focus water quality sampling on a subset of 32 sampling sites that captured
617 the full range of variation in ancestry structure present in each stream and collected
618 measurements from these sites between February 2022 and September 2024 (Fig. 1). Due to
619 changes in equipment availability over time, sample sizes for individual water quality
620 measurements varied between 0 and 13 per location and measure; for details on all measures
621 collected and sample sizes per location, see Table S3. All water chemistry measurements were
622 taken from streambanks or exposed rocks to minimize disturbance of bottom sediments, and
623 samples were collected 2–10 cm below the stream surface with laboratory-grade plastic bottles,
624 50 mL Falcon tubes and 50 mL sterile syringes. We measured temperature, conductivity,
625 dissolved oxygen, and fluorescent dissolved organic matter (fDOM) using YSI EXO 2 and EXO
626 1s multiparameter sondes (Xylem Inc.) held 2–10 cm below the stream surface. Turbidity was
627 measured in nephelometric turbidity units (NTUs) with an Orion AQ4500 Turbidity Meter
628 (Thermo Fisher). Using a YSI 9500 photometer, we applied colorimetric assays to measure pH,
629 total alkalinity, total hardness, calcium hardness, and concentrations of sulfate, sulfite, sulfide,
630 phosphate, ammonia, nitrite, and nitrate. Turbidity measurements and colorimetry tests were

631 performed at the site of sampling to ensure the accurate measurement of unstable chemicals,
632 while further measurements were performed on collected water samples. For measurements of
633 dissolved organic carbon (DOC) and total nitrogen, we stored samples in glass vials capped with
634 PTFE/silicone septa, which were combusted at 500 °C for 1 hour and rinsed ten times with
635 ultrapure water (Milli-Q® Merck) prior to sample collection. Water samples were processed on-
636 site by syringe-filtering through a 0.45 μm polyethersulfone (PES) membrane, acidifying to pH
637 2–3 using concentrated hydrochloric acid, and capping with no air bubbles remaining in the vial.
638 DOC and N measurements were carried out on a Shimadzu TOC-L analyzer using the TC/IC and
639 TN protocols, respectively, at the Environmental Engineering Laboratory of the National
640 Autonomous University of Mexico (UNAM) and the Environmental Measurements Facility at
641 Stanford University. Total and dissolved metals were measured from samples collected in 50 mL
642 Falcon tubes triple-rinsed with sample water, with samples for dissolved metals filtered through
643 0.45 μm PES and all samples acidified to a pH of ~2 using trace metal grade nitric acid.
644 Inductively coupled plasma mass spectrometry (ICP-MS) detection of 39 ions was carried out
645 following a modified version of the APHA3030B/6020A methods by ALS Environmental
646 (Waterloo, ON; see Table S3 for full list of ions and QA/QC). Given that many metals in the
647 filtered samples were below the lower detection limits of ICP-MS, we used ICP-MS
648 measurements of total concentration from unfiltered samples in all downstream statistical
649 analyses.
650
651 *Histology in wild-caught and laboratory fish*
652 Like their relatives (97), *X. malinche* × *birchmanni* hybrids have plate-like olfactory rosettes with
653 beds of sensory epithelia surrounded by ridges of nonsensory tissue (Fig. S11). Sensory epithelial

654 beds contain a combination of ciliated and microvillous olfactory neurons, which collect and
655 transmit chemical information to the olfactory bulb, and ciliated sustentacular cells, which
656 increase flow over the beds to heighten olfactory sensitivity (81, 98). The intervening nonsensory
657 ridges are composed largely of connective tissue and goblet cells, the latter of which are
658 responsible for producing the glycoprotein-based mucus which physically shields the epithelium
659 from irritants (86, 97). Based on reports from the literature (54–56, 86, 87), we quantified the
660 loss of cilia from the sensory epithelial surface and the proliferation of goblet cells in the
661 nonsensory epithelium and treated these two measures as a proxy for olfactory disruption.
662 To understand whether polluted water was directly impacting the sensory periphery of
663 fish in *X. malinche* × *birchmanni* populations, we collected a total of 30 fish each from the
664 Aguazarca and Calnali Low populations in May (n = 10 per site) and September (n = 20) 2022.
665 Fishes were euthanized by MS-222 overdose and decapitation, after which heads were fixed in
666 10% buffered formalin for at least 48 hours. Fixed crania were dissected to remove the gills and
667 lower jaw, decalcified for 8 hours in 1X PBS with 10% formic acid, then dehydrated for 20
668 minutes each in 30%, 50%, and 70% ethanol before long-term storage in 70% ethanol. Samples
669 were submitted to Histo-Tec Laboratories (Hayward, CA) for xylene clearing, paraffin
670 embedding, sectioning, and staining. Horizontal sections were taken at 5 μm intervals with a
671 rotary microtome after removing 75–150 μm of tissue from the dorsal surface, with deeper
672 sectioning needed to reach the olfactory epithelia in larger individuals. One slide per individual
673 was prepared with hematoxylin and eosin (H&E) staining to observe gross morphological
674 changes (i.e. presence/absence of ciliary on olfactory epithelium). Samples from one collection
675 (May 2022) were also subject to Alcian Blue / Periodic Acid-Schiff stain for mucoproteins to
676 identify mucus-producing goblet cells, with eosin as a counterstain. Individuals for whom

677 olfactory rosettes were not present in the Histo-Tec slides were excluded from further analysis
678 (final cilia n = 27 for Aguazarca, n = 29 for Calnali Low; final goblet cell n = 9 individuals for
679 both populations). Slides were scored by a single blinded observer at 1000X magnification using
680 oil immersion. We defined the bounds of each sensory epithelial bed, and estimated the
681 proportion of the surface area of each bed on which cilia were visible to the nearest 10%. We
682 also scanned and imaged each slide at 40x magnification via a Biotek Cytation5 microplate
683 reader, utilizing the in-place ruler on the image to calculate the length of each bed in ImageJ.
684 Finally, we designed an experiment to test if laboratory exposure to ammonia, copper,
685 and dissolved organic matter, alone or in combination, could replicate histological changes
686 observed in the wild. We chose these three compounds as known neurological and olfactory
687 toxicants in fishes (19, 70, 99) which were elevated in the site of population structure collapse
688 downstream of the town of Calnali (Fig. 6). In each round of testing, adult *X. birchmanni* were
689 exposed to either 0.25 mg/L total ammonia (delivered as NH_4Cl, VWR BDH9208), 2 μg/L
690 copper (delivered as $CuCl_2$, Sigma Aldrich 307483), 20 mg/L humic acid (Sigma Aldrich 53680),
691 all three treatments combined, or a no-treatment control. These concentrations were chosen to
692 match those observed in polluted sites downstream of the town of Calnali (ammonia and copper)
693 or to match prior studies showing effects on *Xiphophorus* mate choice (humic acid) (19).
694 Concentrations were maintained by daily 50% water changes, and water samples were taken
695 before and after water changes to ground-truth concentrations in the tanks. After 96 hours of
696 exposure, fish were euthanized by lethal MS-222 overdose and decapitation, after which heads
697 were fixed in 10% buffered formalin for at least 48 hours. The experiment was run in two
698 batches, in July and August 2023, for a total of 10 fish per treatment. Horizontal cranial sections
699 were prepared, H&E and AB/PAS staining were performed, and ciliary coverage and goblet cell

700 densities were quantified as described for wild-caught fish. Ground-truth water samples were
701 tested for the concentration of ammonium, dissolved organic carbon, and total copper on a
702 Westco SmartChem 200 Discrete Analyzer, a Shimadzu TOC/TN Analyzer (TOC-L), and a
703 Thermo Scientific™ iCAP™ RQ ICP-MS, respectively. These tests confirmed that we achieved
704 the desired change in ammonia and copper concentrations to mirror those seen between natural
705 sites, though the change in dissolved organic carbon with our treatment of humic acid was lower
706 than the range of natural variation (Fig. S12).
707
708 ***Quantification and Statistical Analysis***
709
710 *Local ancestry inference*
711
712 Hybrids between *X. birchmanni* and *X. malinche* harbor ancestry from both species that
713 varies locally along the genome and globally between individuals and populations. We used an
714 approach developed by our group for accurate local ancestry inference in *X. malinche* × *X.*
715 *birchmanni* hybrids that relies on a hidden Markov model and known ancestry informative sites
716 that distinguish *X. birchmanni* and *X. malinche* to infer local ancestry (*ancestryinfer*) (100). Both
717 simulation studies (100) and analyses of populations of known ancestry have indicated that this
718 approach has a low error rate (~0.1% per ancestry informative site) (45, 101). Likewise,
719 inference of local ancestry is robust to a number of technical challenges, including parameter
720 misspecification (100).
721 We inferred local ancestry using *ancestryinfer* from whole genome sequence data for all
722 individuals for which we collected more than 300,000 reads from the sequencing approach

723 described above, with a maximum of 2,000,000 reads aligned per individual for computational
724 efficiency. This coverage cutoff is based on previous simulation studies (100) and resulted in 12
725 to 702 individuals per site post-filtering (median 32; Table S4). *ancestryinfer* outputs posterior
726 probabilities of ancestry for all informative sites along the genome. In the case of *X. malinche* ×
727 *X. birchmanni* hybrids, this results in estimates of ancestry at 729,167 ancestry informative sites
728 across 24 chromosomes. Since we were primarily interested in accurately estimating global
729 admixture proportion for individuals along a spatial cline, we converted posterior probabilities to
730 'hard calls' using a threshold of 0.9. For example, if an individual had a posterior probability
731 greater than or equal to 0.9 for *X. malinche* ancestry at a given marker, we converted that marker
732 to the *X. malinche* state. If both ancestries had a summed probability ≤0.1, the site was called as
733 heterozygous, and if a site did not have a posterior probability ≥0.9 for any ancestry state, we
734 converted the site to missing data (average missing data across all individuals = 13.1%).
735 We used ancestry hard calls to estimate the proportion of the genome derived from each
736 parental species. We estimated this proportion using two approaches. First, we calculated the
737 ratio of the number of alleles called for the *X. malinche* state out of the total number of alleles
738 called (treating heterozygous sites as 1 allele for each parental species). We also used a spatially
739 aware approach, given that there is variation in the distance between ancestry informative sites.
740 To do so, we calculated the proportion of the genome covered by high-confidence *X. malinche* or
741 *X. birchmanni* ancestry tracts, excluding regions that were not confidently called from the
742 denominator. In practice, this approach generated nearly identical results (Supp. Info. 5; Fig.
743 S13).
744 With these results in hand, we visualized the distribution of admixture proportion in
745 populations along the Río Calnali, Río Pochula, Río Huazalingo, and Río Conzintla (Fig. 3). As

746 previous results had indicated the presence of bimodal ancestry structure in upstream populations
747 of the Río Calnali, we also calculated Hartigan's dip statistic (102), which quantifies departures
748 from a unimodal distribution, on samples from each collection site. Since we used this test across
749 many collection sites, we applied a Bonferroni correction for the number of tests. We recognized
750 that variation in sample sizes across sites (Table S4) might complicate our interpretation of these
751 results, and so we tested the effects of sample size on our ability to detect significant ancestry
752 structure (Supp. Info. 6, Table S5). Samples were collected between 2006 and 2024, with the
753 highest sampling density between 2014 and 2022 (Table S2). Given the broad period over which
754 samples were collected and the uneven spatial distribution of sampling in some years, we also
755 sought to ensure that any spatial differences in ancestry structure we observed were not due to
756 changing ancestry over time. As such, we evaluated whether ancestry structure was stable at a
757 given site across the study period (Supp. Info. 1; Fig. S1) (52).
758
759 *Analysis of ancestry-assortative mating*
760
761 Previous work has shown that the distinct ancestry clusters in the Río Calnali upstream of
762 the town of Calnali are maintained by strong ancestry-assortative mating (52). Note that in this
763 prior work, samples from the nearby sites Aguazarca and Calnali Mid were pooled for analysis,
764 but we analyzed them separately here (Fig. 1B). In the current study, we identified the Calnali
765 Low population as one of the first sampling sites where this genetic structure breaks down along
766 the Río Calnali. As a result, we were interested in evaluating the strength of ancestry-assortative
767 mating in this population and making comparisons to upstream populations.

To do so, we analyzed mother-embryo samples from the Calnali Low population, including previously published samples collected in 2020 (45), as well as newly sequenced samples from a 2017 collection, and compared them to mother-embryo pairs collected from populations upstream of the town of Calnali between 2008 and 2018. Because swordtails are livebearing fish that exhibit multiple paternity, when we collected pregnant *X. malinche* × *X. birchmanni* females we also collected ~10 offspring from 2–3 fathers (103). Although we cannot directly assay the paternal genotypes, we can use the ancestry of the offspring to infer the ancestry of the male that sired each embryo, since offspring will inherit approximately 50% of their genome from each parent. Thus, the difference between the mother's genome-wide ancestry and the genome-wide ancestry of her offspring is a useful proxy for paternal ancestry.

We have previously used this approach to quantify ancestry-assortative mating in upstream sites on the Río Calnali (52), and repeated this approach here. Specifically, we asked about the observed difference between maternal and offspring ancestry genome-wide in each site, compared to expectations under a scenario where females mate at random with respect to male ancestry. To generate a distribution of offspring ancestry expected under no assortative mating, we performed simulations in R (version 4.4.1). For each focal female in our dataset (n = 74 for Calnali Low, n = 22 for Calnali Mid), we randomly sampled a mate from our full dataset of adults from that site (n = 702 for Calnali Low, n = 79 for Calnali Mid). Next, we drew the ancestry for a single offspring from a normal distribution centered on the average of the maternal and paternal ancestry, and with variance drawn from that observed among siblings in our real dataset. Specifically, we calculated the variance in ancestry across 1,000 randomly drawn pairs of siblings from each site; to be conservative in our inference of lost assortative mating, we used the 0.05 quantile of this variance (4×10^{-6}) for our simulations, which was the same across both

791 sites. We repeated this procedure until we had simulated offspring for all the focal females. We
792 generated 1,000 replicate simulations and compared the observed and simulated differences in
793 mother-offspring admixture proportions in each site. Finally, we compared the mean of the
794 difference in mother-offspring admixture proportions between the two populations using a two-
795 sample *t*-test.
796
797 *Inferring the strength of assortative mating*
798
799 We found evidence that the observed mother-offspring ancestry patterns in the Calnali
800 Low site differed subtly from patterns expected if mating were truly random with respect to
801 ancestry (Fig. 4A–B). However, this difference from random mating was much weaker than that
802 inferred in the population upstream of the town of Calnali (Fig. 4A–B). To quantitatively
803 compare the strength of ancestry-assortative mating consistent with the observed data, we used
804 the same approach previously used to quantify the strength of ancestry-assortative mating at
805 upstream sites (52).
806 Briefly, we used an approximate Bayesian computation approach in R (version 4.4.1) to
807 evaluate what levels of ancestry-assortative mating were consistent with our observed data. We
808 drew a probability that a female would accept a mate with an ancestry proportion that differed
809 from hers by more than 5% from a random uniform distribution ranging from 0 (perfect
810 assortative mating) to 1 (random mating). We refer to this value as the strength of assortative
811 mating. For each female, we then randomly drew a mate from the population ancestry
812 distribution. If the mate fell within the ancestry threshold, the mate was accepted. If it did not,
813 we used a random binomial weighted by the strength of assortative mating to determine if the

mate was accepted. If the mate was rejected, we continued this procedure until the female was matched with a mate, then simulated offspring as described above. This was repeated until all females were matched with a mate. We repeated this simulation procedure for a total of 3,000,000 simulations.

We used a simple rejection sampling approach to select simulations that closely matched the empirical data. For each simulation, we calculated the mean and variance of the difference in ancestry between mothers and their offspring. If both summary statistics fell within 5% of the observed value for the site (Calnali Low mean 6.6%, variance 0.46%; Calnali Mid mean 2.5%, variance 0.26%), we accepted the simulation. This allows us to estimate the range of values of assortative mating consistent with our data. We plotted the posterior distribution of accepted assortative mating strengths and identified the maximum a posteriori (MAP) estimate. To test for a difference in the strength of assortative mating between populations, we first evaluated whether the inferred strength of assortative mating in one site fell within the 95% credible interval of the other site, and vice versa. To investigate whether the distributions were significantly different, we randomly matched each of the 1073 accepted simulations from Calnali Mid with one of the 5720 accepted simulations from Calnali Low, sampled without replacement. We then calculated the difference in mating proportion between each pair, and tested whether the median difference was significantly different from 0 using a Wilcoxon signed rank test. The inferred biological effect size was quantified by the MAP and 95% CI of the difference in mating proportion.

Geospatial analyses

To complement our measurements of water chemistry, we measured land use in each stream catchment as a proxy for anthropogenic disturbance. Briefly, we used Google Earth Engine to access Sentinel-2 multispectral imagery from the month of May in the years 2020–2023 (104), removed images with > 20% cloud cover, masked pixels flagged as clouds, then took the median intensity for each band and pixel to construct a composite image with bands 11 (1610 nm, short-wave infrared, 20 m^2 resolution), 8 (842 nm, near-infrared, 10 m^2), and 2 (490 nm, blue, 10 m^2). This spectral combination provides better contrast between built infrastructure, herbaceous, and woody vegetation than the visible spectrum (105). All further analyses were performed in ArcGIS Pro (version 3.3.1) with the Spatial Analyst and Image Analyst extensions. We segmented the three-band raster file using the Segmentation tool, with a spectral detail of 18, a spatial detail of 19, and a minimum size per object of 20 pixels. Next, we selected four land use types for classification: water, forest (continuous tree cover, excluding plantation-style agriculture), non-forest vegetation (grassland, pasture, or cultivated crops, including plantation-style orchard), and developed land (buildings, mines, and roads). We included water surfaces (primarily to prevent their misclassification as other land use types), forest as the primary undisturbed land cover in the area, and non-forest vegetation as an additional form of human disturbance beyond hardened infrastructure. Using 3 m^2-resolution imagery of the study area in March 2022 downloaded from Planet Labs (96), we identified 60 polygons of each land class to serve as training samples. Given the short time frame between the capture of our Sentinel and Planet Labs image sets, we assumed that there would be negligible change in the proportion of land classes. We then used the Classification tool to perform object-based land use classification using a support vector machine algorithm with maximum 500 samples per class. We visually

inspected the resulting classification for pixels misclassified as developed land, and removed these pixels from the dataset prior to further analyses (0.8% of all pixels).

To delineate catchments for each sampling site, we downloaded a digital elevation model (DEM) of the state of Hidalgo with 15 m^2 resolution from the Mexican National Institute for Statistics and Geography (106). Starting with this DEM, we calculated flow direction and flow accumulation, snapped each site to the nearest pour point pixel, and calculated the land area which drained into the stream upstream of a given site (Fig. S6), using the Flow Direction, Flow Accumulation, Snap Pour Points, and Watershed tools, respectively. To identify the land area with greatest potential for runoff into waterways (i.e. greatest influence on water chemistry), we used the Raster Calculator tool. We converted all cells which received flow from at least 3000 uphill cells into a polyline object representing the relevant waterways in our study area (Fig. S6). We then used the Buffer tool to identify the land area within 500 m, 100 m, and 50 m of these waterways, and used the Clip Raster tool to identify the subset of classified land use pixels within each of these buffers. Using the Zonal Histogram tool, we summed the pixel counts of each land use category in each site's subcatchment, then calculated the proportion of the total pixels per subcatchment composed of each land use type. Finally, we calculated cumulative land use within a site's watershed by summing the land use categories within its own site-specific subcatchment and within the subcatchments of all upstream sites.

Water chemistry surveys

Unless otherwise noted, all further statistical analyses were performed in R (version 4.4.1) with RStudio (107). We first explored overall differences in water chemistry between sites

and drainages using Principal Component Analysis (PCA). Given differing sample sizes of ICP-MS measurement relative to other measures, we conducted two separate PCAs, one for ICP-MS metals measurement (n = 66 measurements) and one for all other data (n = 58). For water chemistry parameters other than metals, we included only measurements that were consistently collected throughout the length of the field study, including dissolved oxygen (mg/L), fDOM (quinine sulfate units), conductivity (μS/cm), total hardness (mg/L $CaCO_3$ equivalent), total alkalinity (mg/L $CaCO_3$ equivalent), pH, nitrite (mg/L N), ammonia (mg/L N), phosphate (mg/L PO_4), sulfate (mg/L SO_4), and turbidity (NTU). Of the 39 ions measured in the metal measurements, we retained 30 that had more than one measurement above the lower detection limits of ICP-MS. For the purposes of this analysis, metals measurements below the detection limit were set to halfway between zero and the lower detection limit. For example, for cadmium, the detection limit was 5 ng/L, and we set values below the detection limit to 2.5 ng/L. While this approach has some limitations (108, 109) compared to alternative approaches using imputation (110), we could not apply imputation approaches to our data given the possibility of systematic differences in concentrations of many of the metals between streams. However, we explored the potential impacts of this analysis choice on our conclusions by repeating PCAs with the measurements below the detection limit set to the detection limit or zero, and found our results were qualitatively unchanged.

We also used the PCA analysis to qualitatively compare patterns within and across streams and identify chemicals of interest for further statistical analysis. Specifically, we chose chemicals that had negative loadings on both PC1 and PC2 in either the non-metal or metal PCA because we found that this approach clearly separated sites downstream on the Río Calnali from the others (Fig. 6). From this set of parameters, we next identified those which had evidence for

affecting fish neurobiology, olfaction, or mate choice in the literature. These parameters included DOM (19), turbidity (111), nitrite (112), ammonia (72, 99), copper (54, 113), lead (114), cadmium (73, 115), zinc (116), and aluminum (117). In the analysis of ICP-MS metals data, where the effects of samples below the detection limit prevented the use of parametric tests, we used Kruskal-Wallis tests to identify differences in concentration within and between drainages. For all other variables, we used ANOVA and Tukey's HSD tests to confirm differences between the downstream Calnali sites and the other groups, testing for differences in the natural log-transformed response variables as a function of drainage, sampling month, and their interaction. We also used the same approach to explore differences in water chemistry between watersheds (Supp. Info. 2; Fig. S6–7) and over different years across the sampling period (Supp. Info. 3; Fig. S8–9).

Histological data

We normalized ciliated proportions by bed length to calculate the total proportion of the sensory epithelium with visible cilia in each individual, then used a Mann-Whitney *U* test to test for differences in ciliated surface proportion between fish from Aguazarca and Calnali Low. Kolmogorov-Smirnov tests indicated that the ciliated surface proportions were not significantly different between the two sampling months ($P = 0.481$), and that there was no significant difference between the two populations or sampling months in the number of sensory beds (population $P = 0.7951$, month $P = 0.5238$), individual bed length (population $P = 0.08173$, month $P = 0.3268$), or total bed length (population $P = 0.6684$, month $P = 0.2415$). To estimate the density of goblet cells, a blinded observer counted all cells positive for AB/PAS staining

within a bed, and we tested for a significant difference between populations in the number of cells per individual, corrected for total rosette length, using Mann-Whitney *U* tests. For laboratory chemical exposure trial data, we tested for significant differences between treatments in the rates of ciliary loss and goblet cell densities using non-parametric Kruskal-Wallis tests.

932 **Key Resources Table**

REAGENT or RESOURCE	SOURCE	IDENTIFIER
Chemicals, peptides, and recombinant proteins		
Ammonium Chloride (NH_4Cl)	VWR	Cat#BDH9208
Copper chloride ($CuCl_2$)	Sigma Aldrich	Cat#307483
Humic Acid	Sigma Aldrich	Cat#53680
Critical commercial assays		
DNAdvance Extraction Kit	Beckman Coulter	Cat#A48705
TDE1 Enzyme and Buffer Kit	Illumina	Cat#20034197
OneTaq® Hot Start Quick-Load® 2X Master Mix with Standard Buffer	New England Biolabs	Cat#M0488
Qubit 1X dsDNA High Sensitivity Assay Kit	Thermofisher Scientific	Cat#Q33231
D1000 Screentape	Agilent	Cat#5067-5582
9300 photometer kit – pH	YSI	YAP130
9300 photometer kit – total alkalinity	YSI	YAP188
9300 photometer kit – total hardness	YSI	YAP254
9300 photometer kit – calcium hardness	YSI	YAP252
9300 photometer kit – sulfate	YSI	YAP154
9300 photometer kit – sulfite	YSI	YAP266
9300 photometer kit – sulfide	YSI	YAP168
9300 photometer kit – phosphate low range	YSI	YAP177
9300 photometer kit – ammonia	YSI	YAP152
9300 photometer kit – nitrate	YSI	YAP163
9300 photometer kit – nitrite	YSI	YAP109
Deposited data		
NCBI Sequence Read Archive: new short-read WGS data from wild *X. malinche* × *X. birchmanni*	This paper	PRJNA1346846
NCBI Sequence Read Archive: Río Pochula short-read WGS data	Robles et al. 2025 (118)	PRJNA1305547
NCBI Sequence Read Archive: Calnali Low short-read WGS data	Moran et al. 2024 (45)	PRJNA744894
NCBI Sequence Read Archive: Tlalica short-read WGS data	Banerjee et al. 2023 (101)	PRJNA930165
NCBI Sequence Read Archive: Chahuaco Falls short-read WGS data	Powell et al. 2020 (44)	PRJNA610049
Dryad: Geospatial and organismal datasets	This paper	https://doi.org/10.5061/dryad.nvx0k6f5h
Github: code used for paper-specific analyses	This paper	https://github.com/benmoran11/anthro_xipho_hybrids
Github: general ancestry file processing scripts	This paper	https://github.com/Schumerlab/Lab_shared_scripts
Experimental models: Organisms/strains		
Xiphophorus malinche × *X. birchmanni* wild-caught samples	This paper	N/A
Xiphophorus birchmanni laboratory-raised fish (Coacuilco population of origin)	This paper	N/A
Software and algorithms		

Ancestryinfer commit ae89066	Schumer et al. (100)	https://github.com/Schumerlab/ancestryinfer
R v4.4.1	R Core Team (119)	https://www.R-project.org/
ArcGIS v3.3.1	ESRI	https://www.esri.com/en-us/arcgis/products/arcgis-pro
ImageJ v1.52q	Schneider et al. (120)	https://mvnrepository.com/artifact/net.imagej/ij/1.52q

Supplemental Information

Document S1: Supplemental Information, Supplemental Figures S1–13 and Supplemental Tables S1–2 and S4–6.

Table S3. Metadata for water chemistry measurements. The first two sheets list sample sizes for all water chemistry variables, the first excluding measurements from September as in the main text analysis, and the second for all timepoints. Site codes match those in Table S1. The next sheet provides a key connecting ICP-MS sample codes in subsequent sheets to locations and sampling times provided in the publication. Subsequent sheets provide detailed ICP-MS results for each sample, results of technical duplicates and quality control samples, methodology used, holding time exceedances, and detection limits for each ion. (Provided as Excel file)

References

1. R. J. Abbott, N. H. Barton, J. M. Good, Genomics of hybridization and its evolutionary consequences. *Molecular Ecology* **25**, 2325–2332 (2016).

2. N. H. Barton, The role of hybridization in evolution. *Molecular Ecology* **10**, 551–568 (2001).

3. E. Mayr, *Systematics and the Origin of Species: from the Viewpoint of a Zoologist* (Columbia University Press, 1942).

4. E. Anderson, Hybridization of the habitat. *Evolution* 1–9 (1948).

5. K. C. Grabenstein, S. A. Taylor, Breaking barriers: causes, consequences, and experimental utility of human-mediated hybridization. *Trends in Ecology & Evolution* **33**, 198–212 (2018).

6. J.-G. J. Godin, S. E. Briggs, Female mate choice under predation risk in the guppy. *Animal Behaviour* **51**, 117–130 (1996).

7. P. M. Willis, M. J. Ryan, G. G. Rosenthal, Encounter rates with conspecific males influence female mate choice in a naturally hybridizing fish. *Behavioral Ecology* **22**, 1234–1240 (2011).

8. M. N. Verzijden, Z. W. Culumber, G. G. Rosenthal, Opposite effects of learning cause asymmetric mate preferences in hybridizing species. *Behavioral Ecology* **23**, 1133–1139 (2012).

9. J. Hunt, R. Brooks, M. D. Jennions, Female mate choice as a condition-dependent life-history trait. *The American Naturalist* **166**, 79–92 (2005).

10. A. E. Hausmann, *et al.*, Light environment influences mating behaviours during the early stages of divergence in tropical butterflies. *Proceedings of the Royal Society B: Biological Sciences* **288**, 20210157 (2021).

11. K. S. Pfennig, Facultative mate choice drives adaptive hybridization. *Science* **318**, 965–967 (2007).

12. G. G. Rosenthal, D. Stuart-Fox, others, “Environmental disturbance and animal communication” in *Behavioural Responses to a Changing World: Mechanisms and Consequences*, (Oxford University Press, 2015), pp. 16–31.

13. G. G. Rosenthal, Individual mating decisions and hybridization. *Journal of Evolutionary Biology* **26**, 252–255 (2013).

14. O. Seehausen, J. J. M. van Alphen, F. Witte, Cichlid fish diversity threatened by eutrophication that curbs sexual selection. *Science* **277**, 1808–1811 (1997).

15. B. Seifert, J. Kulmuni, P. Pamilo, Independent hybrid populations of Formica polyctena Xrufa wood ants (Hymenoptera: Formicidae) abound under conditions of forest fragmentation. *Evolutionary Ecology* **24**, 1219–1237 (2010).

16. R. Ubsdell, Studies on variation and evolution in Centaurium erythraea Rafn and C. littorale (D. Turner) Gilmour in the British Isles. 3. Breeding systems, floral biology and general discussion. *Watsonia* **12**, 225–232 (1979).

17. C. Brochmann, Hybridization and distribution of Argyranthemum coronopifolium (Asteraceae – Anthemideae) in the Canary Islands. *Nordic Journal of Botany* **4**, 729–736 (1984).

18. P. Vonlanthen, *et al.*, Eutrophication causes speciation reversal in whitefish adaptive radiations. *Nature* **482**, 357–362 (2012).

19. H. S. Fisher, B. B. M. Wong, G. G. Rosenthal, Alteration of the chemical environment disrupts communication in a freshwater fish. *Proceedings of the Royal Society B: Biological Sciences* **273**, 1187–1193 (2006).

20. J. L. Ward, M. J. Blum, Exposure to an environmental estrogen breaks down sexual isolation between native and invasive species. *Evolutionary Applications* **5**, 901–912 (2012).

21. J. W. Boughman, J. A. Brand, R. C. Brooks, R. Bonduriansky, B. B. M. Wong, Sexual selection and speciation in the Anthropocene. *Trends in Ecology & Evolution* **39**, 654–665 (2024).

22. P. C. Hubbard, E. N. Barata, A. V. M. Canario, Possible disruption of pheromonal communication by humic acid in the goldfish, Carassius auratus. *Aquatic Toxicology* **60**, 169–183 (2002).

23. D. L. Powell, A. D. Rose, G. G. Rosenthal, A widely-used pollutant causes reversal of conspecific mate preference in a freshwater fish. [Preprint] (2022). Available at: https://www.biorxiv.org/content/10.1101/2022.09.07.507014v1 [Accessed 1 September 2023].

24. W. F. Ramirez-Duarte, *et al.*, Hybridization in the Anthropocene – how pollution and climate change disrupt mate selection in freshwater fish. *Biological Reviews* **100**, 35–49 (2025).

25. E. C. Ellis, Anthropogenic transformation of the terrestrial biosphere. *Philosophical Transactions of the Royal Society A: Mathematical, Physical and Engineering Sciences* **369**, 1010–1035 (2011).

26. R. T. Gilman, J. E. Behm, Hybridization, species collapse, and species reemergence after disturbance to premating mechanisms of reproductive isolation. *Evolution* **65**, 2592–2605 (2011).

27. D. J. Hasselman, *et al.*, Human disturbance causes the formation of a hybrid swarm between two naturally sympatric fish species. *Molecular Ecology* **23**, 1137–1152 (2014).

28. T. B. Malek, J. W. Boughman, I. Dworkin, C. L. Peichel, Admixture mapping of male nuptial colour and body shape in a recently formed hybrid population of threespine stickleback. *Molecular Ecology* **21**, 5265–5279 (2012).

29. B. Alric, *et al.*, Local human pressures influence gene flow in a hybridizing Daphnia species complex. *Journal of Evolutionary Biology* **29**, 720–735 (2016).

30. T. van Hengstum, *et al.*, Human-induced hybridization among congeneric endemic plants on Tenerife, Canary Islands. *Plant Systematics and Evolution* **298**, 1119–1131 (2012).

31. C. Chen, K. S. Pfennig, Female toads engaging in adaptive hybridization prefer high-quality heterospecifics as mates. *Science* **367**, 1377–1379 (2020).

32. N. B. Edelman, J. Mallet, Prevalence and adaptive impact of introgression. *Annual Review of Genetics* **55**, 265–283 (2021).

33. J. I. Meier, *et al.*, Ancient hybridization fuels rapid cichlid fish adaptive radiations. *Nature Communications* **8**, 14363 (2017).

34. S. A. Taylor, E. L. Larson, Insights from genomes into the evolutionary importance and prevalence of hybridization in nature. *Nature Ecology & Evolution* **3**, 170–177 (2019).

35. M. Schumer, R. Cui, G. G. Rosenthal, P. Andolfatto, Reproductive isolation of hybrid populations driven by genetic incompatibilities. *PLOS Genetics* **11**, e1005041 (2015).

36. C. Veller, N. B. Edelman, P. Muralidhar, M. A. Nowak, Recombination and selection against introgressed DNA. *Evolution* **77**, 1131–1144 (2023).

37. M. Ribeiro Palacios, “Land use change in Southern Huasteca, Mexico; drivers and consequences for livelihood and ecosystem services,” Instituto Potosino de Investigación Científica y Tecnológica. (2012).

38. H. R. Hernández, M. A. Robledo, J. R. A. Rivera, J. F. Martinez, Spatial configuration of land-use/land-cover in the Pujal-Coy Project Area, Huasteca Potosina region, Mexico. *Ambio* **37**, 381–389 (2008).

39. M. L. Martínez, *et al.*, Effects of land use change on biodiversity and ecosystem services in tropical montane cloud forests of Mexico. *Forest Ecology and Management* **258**, 1856–1863 (2009).

40. L. Chapa-Vargas, K. Monzalvo-Santos, Natural protected areas of San Luis Potosí, Mexico: ecological representativeness, risks, and conservation implications across scales. *International Journal of Geographical Information Science* **26**, 1625–1641 (2012).

41. C. Payne, *et al.*, Genomic insights into variation in thermotolerance between hybridizing swordtail fishes. *Molecular Ecology* (2022). https://doi.org/10.1111/mec.16489.

42. Z. W. Culumber, D. B. Shepard, S. W. Coleman, G. G. Rosenthal, M. Tobler, Physiological adaptation along environmental gradients and replicated hybrid zone structure in swordtails (Teleostei: Xiphophorus). *Journal of Evolutionary Biology* **25**, 1800–1814 (2012).

43. M. Schumer, *et al.*, Natural selection interacts with recombination to shape the evolution of hybrid genomes. *Science* **360**, 656–660 (2018).

44. D. L. Powell, *et al.*, Natural hybridization reveals incompatible alleles that cause melanoma in swordtail fish. *Science* **368**, 731–736 (2020).

45. B. M. Moran, *et al.*, A lethal mitonuclear incompatibility in complex I of natural hybrids. *Nature* **626**, 119–127 (2024).

46. M. Schumer, Y. Brandvain, Determining epistatic selection in admixed populations. *Molecular Ecology* **25**, 2577–2591 (2016).

47. Z. W. Culumber, *et al.*, Replicated hybrid zones of *Xiphophorus* swordtails along an elevational gradient. *Molecular Ecology* **20**, 342–356 (2011).

48. M. Rauchenberger, I. K. D. Kallman, Monophyly and geography of the Rio Pánuco basin swordtails (Genus Xiphophorus) with descriptions of four new species. *American Museum Novitates* 44 (1990).

49. G. G. Rosenthal, *et al.*, Dissolution of Sexual Signal Complexes in a Hybrid Zone between the Swordtails Xiphophorus birchmanni and Xiphophorus malinche (Poeciliidae). *Copeia* **2003**, 299–307 (2003).

50. INEGI, México en cifras. (1998). Available at: https://www.inegi.org.mx/app/areasgeograficas/ [Accessed 6 April 2025].

51. M. Schumer, *et al.*, High-resolution mapping reveals hundreds of genetic incompatibilities in hybridizing fish species. *eLife* **3**, e02535 (2014).

52. M. Schumer, *et al.*, Assortative mating and persistent reproductive isolation in hybrids. *Proceedings of the National Academy of Sciences* **114**, 10936–10941 (2017).

53. O. Seehausen, *et al.*, Genomics and the origin of species. *Nature Reviews Genetics* **15**, 176–192 (2014).

54. J. A. Hansen, J. D. Rose, R. A. Jenkins, K. G. Gerow, H. L. Bergman, Chinook salmon (Oncorhynchus tshawytscha) and rainbow trout (Oncorhynchus mykiss) exposed to copper: Neurophysiological and histological effects on the olfactory system. *Environmental Toxicology and Chemistry* **18**, 1979–1991 (1999).

55. M. Lazzari, S. Bettini, L. Milani, M. G. Maurizii, V. Franceschini, Differential response of olfactory sensory neuron populations to copper ion exposure in zebrafish. *Aquatic Toxicology* **183**, 54–62 (2017).

56. K. E. Klima, F. M. Applehans, Copper exposure and the degeneration of olfactory receptors in rainbow trout (Oncorhynchus mykiss). *Chemical Speciation & Bioavailability* **2**, 149–154 (1990).

57. Fish and Wildlife Service, US Department of the Interior, Endangered and threatened wildlife and plants; 90-day finding on a petition to list the Colorado River cutthroat trout. *Federal Register* **69**, 21151–21158 (2004).

58. N. H. Barton, K. S. Gale, "Genetic Analysis of Hybrid Zones" in *Hybrid Zones and the Evolutionary Process*, p. 33.

59. S. Cotton, J. Small, A. Pomiankowski, Sexual selection and condition-dependent mate preferences. *Current Biology* **16**, R755–R765 (2006).

60. B.-J. Velthuis, W. Yang, T. Van Opijnen, J. H. Werren, Genetics of female mate discrimination of heterospecific males in *Nasonia* (Hymenoptera, Pteromalidae). *Animal Behaviour* **69**, 1107–1120 (2005).

61. O. Svensson, *et al.*, The genetics of mate preferences in hybrids between two young and sympatric Lake Victoria cichlid species. *Proceedings of the Royal Society B: Biological Sciences* **284**, 20162332 (2017).

62. E. M. Schmidt, K. S. Pfennig, Hybrid female mate choice as a species isolating mechanism: environment matters. *Journal of Evolutionary Biology* **29**, 865–869 (2016).

63. J. Lunt, D. L. Smee, Turbidity interferes with foraging success of visual but not chemosensory predators. *PeerJ* **3**, e1212 (2015).

64. S. M. Leahy, M. I. McCormick, M. D. Mitchell, M. C. O. Ferrari, To fear or to feed: the effects of turbidity on perception of risk by a marine fish. *Biology Letters* **7**, 811–813 (2011).

65. Y. Xia, C. Ti, D. She, X. Yan, Linking river nutrient concentrations to land use and rainfall in a paddy agriculture–urban area gradient watershed in southeast China. *Science of The Total Environment* **566–567**, 1094–1105 (2016).

66. E. Apeagyei, M. S. Bank, J. D. Spengler, Distribution of heavy metals in road dust along an urban-rural gradient in Massachusetts. *Atmospheric Environment* **45**, 2310–2323 (2011).

67. J. J. Sansalone, J. P. Hird, F. K. Cartledge, M. E. Tittlebaum, Event-based stormwater quality and quantity loadings from elevated urban infrastructure affected by transportation. *Water Environment Research* **77**, 348–365 (2005).

68. S. Yu, *et al.*, Anthropogenic land uses elevate metal levels in stream water in an urbanizing watershed. *Science of The Total Environment* **488–489**, 61–69 (2014).

69. V. Paul, M. S. Sankar, S. Vattikuti, P. Dash, Z. Arslan, Pollution assessment and land use land cover influence on trace metal distribution in sediments from five aquatic systems in southern USA. *Chemosphere* **263**, 128243 (2021).

70. D. H. Baldwin, C. P. Tatara, N. L. Scholz, Copper-induced olfactory toxicity in salmon and steelhead: Extrapolation across species and rearing environments. *Aquatic Toxicology* **101**, 295–297 (2011).

71. A. E. Smith, "The influence of sub-lethal zinc exposure on olfaction of alarm cues and associated alarm behaviours in juvenile coho salmon," University of British Columbia. (2023).

72. Y. K. Ip, S. F. Chew, D. J. Randall, "Ammonia toxicity, tolerance, and excretion" in *Fish Physiology*, Nitrogen Excretion., (Academic Press, 2001), pp. 109–148.

73. K. Heffern, K. Tierney, E. P. Gallagher, Comparative effects of cadmium, zinc, arsenic and chromium on olfactory-mediated neurobehavior and gene expression in larval zebrafish (*Danio rerio*). *Aquatic Toxicology* **201**, 83–90 (2018).

74. L. Sonnack, *et al.*, Effects of metal exposure on motor neuron development, neuromasts and the escape response of zebrafish embryos. *Neurotoxicology and Teratology* **50**, 33–42 (2015).

75. M.-D. Crapon de Caprona, M. J. Ryan, Conspecific mate recognition in swordtails, *Xiphophorus nigrensis* and *X. pygmaeus* (Poeciliidae): olfactory and visual cues. *Animal Behaviour* **39**, 290–296 (1990).

76. M. R. Morris, J. A. Moretz, K. Farley, P. Nicoletto, The role of sexual selection in the loss of sexually selected traits in the swordtail fish *Xiphophorus continens*. *Animal Behaviour* **69**, 1415–1424 (2005).

77. B. B. M. Wong, G. G. Rosenthal, Female disdain for swords in a swordtail fish. *The American Naturalist* **167**, 136–140 (2006).

78. H. Tjälve, C. Mejàre, K. Borg-Neczak, Uptake and transport of manganese in primary and secondary olfactory neurones in pike. *Pharmacology & Toxicology* **77**, 23–31 (1995).

79. Y. Rodríguez-Agudelo, *et al.*, Motor alterations associated with exposure to manganese in the environment in Mexico. *Science of The Total Environment* **368**, 542–556 (2006).

80. D. B. Szymkowicz, *et al.*, Exposure to arsenic during embryogenesis impairs olfactory sensory neuron differentiation and function into adulthood. *Toxicology* **420**, 73–84 (2019).

81. P. A. Triana-Garcia, "Studies on The Olfactory Biology and Behavioral Responses to Copper Exposure of The Native Indicator Species Delta Smelt (Hypomesus transpacificus)," UC Davis. (2021).

82. S. J. Song, B. Park, K. Jo, C.-S. Kim, Damage to olfactory organs of adult zebrafish induced by diesel particulate matter. *International Journal of Molecular Sciences* **23**, 407 (2022).

83. I. Reiten, *et al.*, Motile-cilia-mediated flow improves sensitivity and temporal resolution of olfactory computations. *Current Biology* **27**, 166–174 (2017).

84. J. P. L. Cox, Hydrodynamic aspects of fish olfaction. *Journal of The Royal Society Interface* **5**, 575–593 (2008).

85. D. P. McEwen, P. M. Jenkins, J. R. Martens, "Chapter 12 Olfactory Cilia: Our Direct Neuronal Connection to the External World" in *Current Topics in Developmental Biology*, Ciliary Function in Mammalian Development., (Academic Press, 2008), pp. 333–370.

86. T. Shimizu, "Mucus, Goblet Cell, Submucosal Gland" in *Nasal Physiology and Pathophysiology of Nasal Disorders*, T. M. Önerci, Ed. (Springer, 2013), pp. 1–14.

87. D. Saucier, L. Astic, Morpho-functional alterations in the olfactory system of rainbow trout (*Oncorhynchus mykiss*) and possible acclimation in response to long-lasting exposure to low copper levels. *Comparative Biochemistry and Physiology Part A: Physiology* **112**, 273–284 (1995).

88. J. R. Harkema, S. A. Carey, J. G. Wagner, The nose revisited: a brief review of the comparative structure, function, and toxicologic pathology of the nasal epithelium. *Toxicologic Pathology* **34**, 252–269 (2006).

89. S. Schubert, *et al.*, Transient exposure to environmental estrogen affects embryonic development of brown trout (*Salmo trutta fario*). *Aquatic Toxicology* **157**, 141–149 (2014).

90. B. B. H. Yuen, A. B. Qiu, B. H. Chen, Transient exposure to environmentally realistic concentrations of di-(2-ethylhexyl)-phthalate during sensitive windows of development impaired larval survival and reproduction success in Japanese medaka. *Toxicology Reports* **7**, 200–208 (2020).

91. C. E. Hicken, *et al.*, Sublethal exposure to crude oil during embryonic development alters cardiac morphology and reduces aerobic capacity in adult fish. *Proceedings of the National Academy of Sciences* **108**, 7086–7090 (2011).

92. F. R. Gómez de Anda, *et al.*, The nasal epithelium as a route of infection and clinical signs changes, in rainbow trout (Oncorhynchus mykiss) fingerlings infected with Aeromonas spp. *Applied Sciences* **11** (2021).

93. F. W. Sunderman, Nasal toxicity, carcinogenicity, and olfactory uptake of metals. *Annals of Clinical & Laboratory Science* **31**, 3–24 (2001).

94. C. Y. Payne, *et al.*, Recent evolution of large offspring size and post-fertilization nutrient provisioning in swordtails. *Proceedings of the Royal Society B: Biological Sciences* **293**, 20251945 (2026).

95. A. Jacobs, *et al.*, Rapid niche expansion by selection on functional genomic variation after ecosystem recovery. *Nature Ecology & Evolution* **3**, 77–86 (2019).

96. Planet Labs, Planetscope Scene, March 29 2022, Instrument PS2.SD, Strip 5529184. (2022).

97. E. Zeiske, R. Melinkat, H. Breucker, J. Kux, Ultrastructural studies on the epithelia of the olfactory organ of cyprinodonts (teleostei, cyprinodontoidea). *Cell and Tissue Research* **172**, 245–267 (1976).

98. P. A. Triana-Garcia, G. A. Nevitt, J. B. Pesavento, S. J. Teh, Gross morphology, histology, and ultrastructure of the olfactory rosette of a critically endangered indicator species, the Delta Smelt, Hypomesus transpacificus. *Journal of Comparative Physiology. A, Neuroethology, Sensory, Neural, and Behavioral Physiology* **207**, 597–616 (2021).

99. D. J. Randall, T. K. N. Tsui, Ammonia toxicity in fish. *Marine Pollution Bulletin* **45**, 17–23 (2002).

100. M. Schumer, D. L. Powell, R. Corbett-Detig, Versatile simulations of admixture and accurate local ancestry inference with mixnmatch and ancestryinfer. *Molecular Ecology Resources* **20**, 1141–1151 (2020).

101. S. M. Banerjee, *et al.*, Complex hybridization between deeply diverged fish species in a disturbed ecosystem. *Evolution* **77**, 995–1005 (2023).

102. J. A. Hartigan, P. M. Hartigan, The dip test of unimodality. *The Annals of Statistics* **13**, 70–84 (1985).

103. K. A. Paczolt, *et al.*, Multiple Mating and Reproductive Skew in Parental and Introgressed Females of the Live-Bearing Fish Xiphophorus Birchmanni. *Journal of Heredity* **106**, 57–66 (2015).

104. European Union/ESA/Copernicus, Sentinel-2 MSI: MultiSpectral Instrument, Level-2A. (2020).

105. J. Transon, R. D'Andrimont, A. Maugnard, P. Defourny, Survey of hyperspectral Earth observation applications from space in the Sentinel-2 context. *Remote Sensing* **10**, 157 (2018).

106. INEGI, Continuo de elevaciones mexicano y modelos digitales de elevación v3. (2013).

107. Posit team, *RStudio: Integrated Development Environment for R* (Posit Software, PBC, 2023).

108. A. Kamal, K. Wichuk, D. McCartney, K. Londry, C. Felske, Effect of treated wood on biosolids composting. *Compost Science & Utilization* **25**, 178–193 (2017).

109. K. J. Pieper, *et al.*, Evaluating water lead levels during the Flint water crisis. *Environmental Science & Technology* **52**, 8124–8132 (2018).

110. D. R. Helsel, *Nondetects and Data Analysis*. *Statistics for Censored Environmental Data* (2005).

111. O. Seehausen, *et al.*, Speciation through sensory drive in cichlid fish. *Nature* **455**, 620–626 (2008).

112. J.-H. Kim, S. K. Kim, Y. B. Hur, Toxic effects of waterborne nitrite exposure on antioxidant responses, acetylcholinesterase inhibition, and immune responses in olive flounders, *Paralichthys olivaceus*, reared in bio-floc and seawater. *Fish & Shellfish Immunology* **97**, 581–586 (2020).

113. W. A. Dew, A. Azizishirazi, G. G. Pyle, Contaminant-specific targeting of olfactory sensory neuron classes: Connecting neuron class impairment with behavioural deficits. *Chemosphere* **112**, 519–525 (2014).

114. J.-W. Lee, *et al.*, Toxic effects of lead exposure on bioaccumulation, oxidative stress, neurotoxicity, and immune responses in fish: A review. *Environmental Toxicology and Pharmacology* **68**, 101–108 (2019).

115. C. R. Williams, E. P. Gallagher, Effects of cadmium on olfactory mediated behaviors and molecular biomarkers in coho salmon (Oncorhynchus kisutch). *Aquatic Toxicology* **140–141**, 295–302 (2013).

116. J. T. Hentig, C. A. Byrd-Jacobs, Exposure to zinc sulfate results in differential effects on olfactory sensory neuron subtypes in adult zebrafish. *International Journal of Molecular Sciences* **17**, 1445 (2016).

117. D. A. Klaprat, S. Brown, T. J. Hara, The effect of low pH and aluminum on the olfactory organ of rainbow trout, Salmo gairdneri. *Environmental Biology of Fishes* **22**, 69–77 (1988).

118. N. V. Robles, *et al.*, Admixture mapping reveals evidence for multiple mitonuclear incompatibilities in swordtail fish hybrids. *Molecular Ecology* **34**, e70106 (2025).

119. R Core Team, *R: A Language and Environment for Statistical Computing* (R Foundation for Statistical Computing, 2024).

120. C. A. Schneider, W. S. Rasband, K. W. Eliceiri, NIH Image to ImageJ: 25 years of image analysis. *Nature Methods* **9**, 671–675 (2012).

Supplementary Information 1. Confirming stable ancestry structure over time

To study the structure of *X. birchmanni* × *malinche* hybrid zones across numerous sites, we relied on collections gathered over more than a decade (Table S1-2), with repeated sampling at some sites to achieve sufficient sample sizes. The results presented in the main text document patterns of hybrid population structure that vary dramatically across sites, but the variation in sampling dates of our data raise the possibility that some of the spatial differences we observe could in fact be driven by changes over time. In particular, we wished to exclude the possibility that a hybrid population could appear as two structured ancestry clusters in one sampling event, and as a unimodal hybrid swarm in another. To ensure that the contrasting patterns of *X. birchmanni* × *malinche* hybrid ancestry we observed between sites was not a result of a confounding of space and time in our dataset, we used sites with sampling in multiple years to explore the stability of ancestry structure over time.

We began by separating the ancestry data we had collected at each site by collection year, and calculating the mean and variance of ancestry fraction for each sampling location and year. To avoid large fluctuations due to sampling error, rather than true ancestry shifts, we excluded sampling locations and years with a sample size < 10. For each pair of sampling years within a site, we then calculated the difference in mean and variance of ancestry between sampling years. As a broad test for changes in ancestry over time, we calculated the correlation between the number of years between two sampling events at a given location, and the difference in ancestry mean and variance for the two sampling events. This approach allowed us to remove the effect of opportunistic sampling across years of different combinations of sites with varying ancestries. We observed a significant positive relationship between the number of years between sampling events and the absolute value of the change in mean ancestry between sampling points (Spearman's $\rho = 0.475$, $P = 0.012$, $n = 27$) and a negative relationship between the number of years between sampling events and the change in ancestry variance (Spearman's $\rho = -0.403$, $P = 0.037$, $n = 27$). However, this relationship was largely driven by sampling events at a single site, Corazón, which had the longest timespan between samples (2014, 2021, and 2024). The 2014 sample at this site included two clusters of hybrids, one *X. malinche*-like and one *X. birchmanni*-like, but the *X. malinche* cluster became less frequent in 2021, and disappeared entirely in 2024, with little change in the average ancestry of the *X. birchmanni*-like cluster (Fig. S1A). This change in ancestry appears to be either a change in the migration rate of *X. malinche*-like individuals from upstream populations, or a change in the relative fitness of *X. malinche*-like and *X. birchmanni*-like alleles, rather than any change in reproductive isolation between the two clusters. Excluding the Corazón comparisons, there was no longer a significant relationship between temporal separation and change in mean ancestry (Spearman's $\rho = 0.315$, $P = 0.133$, $n = 24$) or variance in ancestry (Spearman's $\rho = -0.200$, $P = 0.349$, $n = 24$). We therefore see little evidence for selection or genetic drift causing major shifts in ancestry proportions across repeated samples at the same site.

To more directly test for changes in the ancestry distributions of our sampled populations over time, we also conducted a Kolmogorov-Smirnov test to evaluate evidence for a shared underlying ancestry distribution between years. We performed this test between pairs of sampling years and implemented a Bonferroni correction for multiple testing. Of the 15 populations where fish were sampled across more than one year, we saw a significant change in the ancestry distribution in three of the populations. The change at Corazón, as previously discussed, was largely a result of the disappearance of the *X. malinche*-like cluster (Fig. S1A).

Though not significant after Bonferroni correction, a similar pattern appeared at the downstream site of Totonicapa, where the mean of the *X. birchmanni*-like cluster was stable over time, but the number of intermediate and *X. malinche*-like individuals varied between sampling events. At the Xochicoatlán site on the Río Conzintla, we observed the same two distinct ancestry clusters in both sampling events, but with a shift from a majority *X. malinche*-like to a majority *X. birchmanni*-like population (Fig. S1B). The last site, Calnali Low, had the most years of sampling, and the most complex patterns of ancestry structure. We see little change in the range of ancestry proportions present in the population across time, with individuals spanning the spectrum from *X. birchmanni*-like to *X. malinche*-like ancestry in every sampling year. However, we do see changes in the relative frequency of individuals with different ancestry proportions (Fig. S1C). Thus, the degree of reproductive isolation and frequency of cross-cluster hybridization seems to be stable across years, but the relative proportion of different ancestry clusters is not. It is unclear whether these shifts are the result of stochastic processes such as migration and genetic drift, or a systematic shift due to changes in fitness of the two clusters. However, it is worth noting that the *X. malinche* cluster decreased in frequency across all three structured sites, as one might expect if warming temperatures were reducing the relative fitness of this high-elevation species.

Finally, we conducted Hartigan's dip test on the data from each sampling site and year, with a Bonferroni correction for multiple testing, to test if the unimodality of ancestry had changed over time at each site. We found three sites at which the Bonferroni-corrected significance of the dip test changed over time. At both Xochicoatlán and Corazón, when samples were separated by year only the first time point showed significant multimodality, in keeping with the decrease in *X. malinche*-like individuals over time (Fig. S1A–B). We note that when combined across years, the full dataset at Xochicoatlán showed significant ancestry structure (Hartigan's $D = 0.192$, $P < 2e\text{-}16$, $n = 70$), while the full data from Corazón did not ($D = 0.032$, $P = 0.586$, $n = 113$). However, since the changes in ancestry we observed did not include an increase in the number of individuals of intermediate ancestry, we treat both these sites as bimodal structured populations for analyses connecting water chemistry to hybrid population structure. At the Calnali Low site, we detected significant multimodality in the most recent time point (2022, $D = 0.066$, $P < 1e\text{-}4$, $n = 155$), with a higher frequency of *X. malinche*-like individuals than is present at other timepoints (Fig. S1C). While this sampling event still contained a full spectrum of ancestries, this intriguing result suggests that ancestry structure could reestablish in the sites downstream of the town of Calnali, given a sufficient number of migrants from upstream structured populations, selection against intermediate hybrids (1, 2), and the restoration of environmental conditions conducive to assortative mating.

Supplementary Information 2. Geological influences on water chemistry

In the main text, we focus on variation in water chemistry distinguishing the sites in the Río Calnali where population structure breaks down. However, our principal component analyses also showed a more general clustering of samples by drainage (Fig. 6). This clustering was sharper in a PCA constructed from ICP-MS data than from non-metal parameters (Fig. 6); given that none of the other streams in our dataset pass directly through a major population center like the town of Calnali, we interpret this variation to be a consequence of geological variation in basins draining to each stream. The bedrock of the Sierra Madre Oriental in Hidalgo is highly variable, with beds of basalt, tuff, limestone, shale, sandstone, breccia, and conglomerate underlying the catchments of the four streams in our survey (Fig. S7) (3). The role of bedrock weathering in determining water chemistry is further supported by the loading of major ionic components of bedrock (Si, Ca, Mg, S) onto the same vector in PC space which separates watersheds (Fig. 6). The effect of geological variation could also be compounded by the presence of an open-pit manganese mine in the headwaters of the Río Conzintla, which may increase sediment inputs to the stream (Fig. S7). Though our study was not designed to directly link water chemistry variation to mining activity, several such mines exist in the Sierra Madre Oriental of Hidalgo, and a targeted study of their ecotoxicological impacts could explore another axis of anthropogenic change in this region.

Geological inputs may also explain the exceptions to the general patterns of separation by drainage that we observe in the ICP-MS PCA. The site Veneno, located in the headwaters of the Río Huazalingo, clustered with the Río Calnali sites in the metals PCA, but with the other Río Huazalingo sites in the non-metals PCA (Fig. 6). Notably, the site's small catchment is located almost entirely within the basalt outcrop which also lies under a large proportion of the Calnali's headwaters (Fig. S7). Likewise, the site Zacatipán is closer in PC space to the Río Huazalingo/Pochula cluster than to the other Río Conzintla sites. This may be because Zacatipán is far downstream of the other measured sites on the Conzintla, and its watershed includes multiple rock beds that are shared with the Huazalingo and Pochula sites, but not with the upstream Conzintla sites. This interpretation is supported by the fact that a nearby site measured on the Conzintla, Otlamalacatla, also groups closer to the Río Huazalingo/Pochula cluster in PC space. Finally, the Atempa site on the Río Pochula has the lowest values on PC1 and PC2 of any site on the Río Pochula, separating from the rest of the river along the same vector which separates the sites upstream and downstream of Calnali. A geothermal spring surfaces in the village of Atempa and drains into the Río Huazalingo after being harnessed for a series of public baths. Thus, either the mineral water itself or to the anthropogenic impacts that stem from its commercial development could be impacting the observed patterns, but this hypothesis would require further sampling to validate.

Supplementary Information 3. Temporal variation in water chemistry

Prior work has shown that reproduction in *Xiphophorus* is seasonal, with pregnancy rates peaking in early summer in both *X. birchmanni* and *X. malinche*, and reproduction nearly nonexistent in high-elevation populations during the fall and winter *(4, 5)*. We therefore focused our studies of water quality on the region's dry season (February through early June), under the assumption that water chemistry in the period coinciding with reproduction would have the most direct effect on mate choice and species barriers. However, we also conducted limited sampling in September, during the rainy season (July through November) to understand how water chemistry might vary throughout the year, and how this might affect our conclusions about the link between water chemistry and population structure.

The Río Calnali drainage was the only area in which we collected more than one sample per site in September (1–3 measurements per site for non-metal parameters, 1–2 for ICP-MS metals), so we began with an in-depth view of seasonal variation in this drainage. We constructed PCAs using data from all seasons for non-metal and metal parameters as in the main text, but excluding sulfate measurements from non-metal analysis due to missing measurements in September. In non-metal parameters, we observed that concentrations of nearly all parameters were lower in the September samples, and that differences between sites upstream and downstream of the town of Calnali were minimized (Fig. S8–9). This suggests that any increase in surface inputs during the rainy season is offset by increased flow, ultimately causing dilution of pollutants. Patterns in metal data were more complex, with PC1 capturing covariation in the concentrations of nearly all ions, and PC2 separating outliers in the rainy season from those in the dry season (Fig. S8–9). Treating PC1 as a measurement correlated with total ion concentration, the divergent value of PC1 across seasons (mean = 1.76 in May, -0.66 in September, and -1.19 in February) aligns with that observed in non-metal parameters. The dominant seasonal trend in water quality in the Calnali is thus a general peak in the concentration of pollutants during the early summer, exactly when *Xiphophorus* reproductive output is at its highest.

Since we lacked non-metal measurements in September for many sites outside of the Calnali, we limited our exploration of cross-drainage temporal patterns in water quality to metals data. We constructed a PCA adding the September sampling to the ICP-MS data featured in the main text, and found again that the first PCA (27% of variation) largely separated variation between stream drainages, with the Río Calnali sites at one end and the Conzintla on the other. The second PC (25% of variation) largely captured variation that was shared between the Río Conzintla samples collected in September and a subset of Río Calnali measurements across seasons (Fig. S8B). Notably, these Conzintla samples were collected after an exceptionally large rainfall caused elevated water levels and turbidity. We are unable to disentangle the effects of space and time without intensive sampling across watersheds under a variety of weather conditions. However, our results suggest that the Conzintla may be especially sensitive to short-term water chemistry fluctuations driven by erosion, potentially due to the open-pit manganese mine present in its headwaters (Fig. S7).

Supplementary Information 4. ICP-MS analysis of fish tissue in the Río Calnali

To understand how changes in concentration of metals in rivers might lead to differential bioaccumulation in swordtails, we measured ion concentrations in whole fish at a subset of our sampling sites on the Río Calnali. Six fish each were collected at CAPASC Fuente de Agua (CAPAC; #15 in Fig. 1 and Table S1), Aguazarca (AGZC), Calnali Low (CALL), and Tlalica (CAPS; #25 in Fig. 1 and Table S1) in November 2021 and February 2022 (total n = 12 individuals per site), with the length and weight of each fish measured before euthanasia and storage at -80°C. At ALS Environmental Services, whole fish were homogenized, subsampled, and microwave digested (EPA Method 3052) before collision-reaction cell ICP-MS (EPA Method 6020B). Where sufficient tissue mass was present, moisture content was also estimated for each sample as the proportional weight loss of a sample after drying at 105°C. Given that many samples were below the weight necessary for moisture analysis, all downstream analyses were performed on a wet-weight basis.

To assess gross morphological differences that might influence bioaccumulation, we used a Type II ANOVA and Tukey's HSD to test for differences in total length and condition factor (weight / total length) as a function of site, month, and their interaction. We also calculated site-wise mean concentrations of each ion and tested the correlation between the concentrations in surface water (see Main Text results) and tissue after controlling for differences in mean metal abundance across all sites. Specifically, we constructed two linear models, one model for measurements in water, and one for measurements from whole fish, each with the ion measured as the explanatory variable and the log-scaled site-wise mean concentration as the response variable. We then took the Spearman's rank correlation of the residuals from the two models. We applied principal component analysis to visualize the tissue concentrations of ions that were consistently measured above the detection limit across all sites (Ag, Al, As, Ca, Cd, Co, Cr, Cu, Fe, K, Mg, Mn, Mo, Na, Pb, Se, Zn). Finally, we tested for differences in tissue metal profiles between groups using redundancy analysis (RDA), with a response matrix composed of all tissue ion concentrations included in PCA, and site, month, and fish length as explanatory variables. For direct comparison between tissue and water data, we conducted an RDA with a response matrix composed of the same ions measured in water at the same four sites, with site and month as explanatory variables.

We found that fish length differed by site (ANOVA P = 0.005) and its interaction with month (P = 0.001, Fig. S10A), but not month alone (P = 0.425) and that individual condition varied with site (ANOVA P = 3.12e-6) and month (P = 4.68e-9), but not their interaction (P = 0.114, Fig. S10B). Ion concentrations were orders of magnitude higher in fish tissue than in the surrounding water (tissue:water ratio range 42–11289, median 430; Fig. S10C), consistent with bioaccumulation of all metals measured. However, correlations between concentrations in water and tissue were not significant after controlling for the mean concentration of each metal across sites (ρ = -0.115, S = 58407, P = 0.3514; Fig. S10C), suggesting that sites with higher aqueous concentrations of a given ion did not predictably have higher tissue concentrations. PCA showed non-overlapping clusters for the sites upstream and downstream of the town of Calnali on the first two principal axes (Fig. S10D). While tissue metal profiles varied upstream and downstream of the town of Calnali as in surface water, loadings on the first two PCs showed less concordant patterns for individual ions, in keeping with our correlation test. Concentrations of zinc, manganese, selenium, potassium, and copper were higher at downstream sites, while all other ions were either higher in upstream sites or undifferentiated between upstream and downstream

sites (Fig. S10D). RDA found that all three explanatory variables had significant effects on fish's overall ionic profiles (site $P = 0.001$, month $P = 0.008$, fish length $P = 0.032$, overall model $P = 0.001$, adjusted $R^2 = 0.302$). More variance was associated with site (30.3% of total variance) than with month (4.1%) or fish length (3.2%). In comparison, RDA of water chemistry data also found a strong relationship between explanatory variables and ion profiles (site $P = 0.001$, month $P = 0.001$, overall model $P = 0.001$, adjusted $R^2 = .491$). However, sampling month captured a much larger portion of the variance (23.3%) relative to site (36.9%).

Our results suggest that any mechanistic connection between aqueous metals and reproductive isolation is unlikely to be mediated by gross bioaccumulation of toxic ions in the body. The total levels of bioaccumulated metals observed in the Río Calnali were modest compared to those observed during intentional ecotoxicological exposure (6), and varied less over time than concentrations in the surrounding water (Fig. S8–9). Though bioaccumulation is occurring, the lack of correlation between relative concentrations of ions at a given site in water and in aggregate tissue suggests that this is accumulation is mediated at least partially by diet or interactions with substrate, rather than direct absorption from water (i.e. bioconcentration) alone. The decoupling of water and tissue concentrations may be driven by a number of intervening mechanistic steps and confounding variables separating sites, including differences in fish size between sites and allometric scaling of tissue types, differences in substrate causing differential trace element sequestration (7), potential differences in swordtail diet between locations, and differential accumulation based on exposure route (8).

Should metal exposure play a role in the observed ancestry structure differences throughout the Atlapexco drainage, it may thus be mediated by ion-specific accumulation in tissues specifically relevant to mate choice (e.g. gonads, brain, sensory organs), which could be explored through more sensitive spectroscopic and histological analyses. Alternatively, a relationship might exist in the absence of tissue-level bioaccumulation should the ions directly affect extracellular interactions between sensory epithelia and signaling molecules, as has been hypothesized in the case of humic acid (9, 10). Thoroughly testing such hypotheses would require the characterization of sexual signaling molecules and development of electro-olfactographic techniques in *Xiphophorus*, both of which are currently lacking.

Supplementary Information 5. Accuracy and robustness of genome-wide ancestry estimates

In our study of water chemistry's effect on hybridization rates in *Xiphophorus*, we used low-coverage whole-genome sequencing and a Hidden Markov Model to infer the ancestry of hybrid individuals at genomic sites that are fixed or nearly fixed for different alleles between *X. birchmanni* and *X. malinche.* To translate genotypes at these ancestry-informative markers (AIMs) to an estimate of the proportion of the genome derived from *X. birchmanni* or *X. malinche,* we tested two approaches. First, we calculated the ratio of the number of AIMs called for the *X. malinche* state at a posterior probability threshold of 0.9, divided by the total number of alleles called, with heterozygous sites counted as 1 allele for each parental species. Second, we calculated ancestry taking the distance between sites into account. To do so, we identified tracts of each individual's genome called with high confidence as *X. malinche*, heterozygous, or *X. birchmanni* ancestry, then took the mean ancestry across all tracts weighted by tract length. Both methods were carried out with custom scripts in Linux bash, Perl, and R, which can be found at https://github.com/benmoran11/anthro_xipho_hybrids (R) and https://github.com/Schumerlab/Lab_shared_scripts (bash and Perl).

These two methods of ancestry estimation are expected to produce the same result if the distance between AIMs is not correlated with genome-wide ancestry. To test this, we applied both methods to 73 hybrid individuals collected at the Plaza site (#22 in Fig. 1 and Table S1) in the Río Calnali. We observed that the allele count estimates were on average slightly less variable between individuals than the ancestry tract method (Fig. S13A). However, the absolute deviation was small in all cases, with a maximum difference between the two methods of 3.99% and a mean difference of 2.51%. We therefore used the allele count method for all subsequent calculations.

Given the wide range of coverage of individual genomes in our dataset (300,000–2,000,000 reads aligned in *ancestryinfer*), we next sought to test how genome-wide ancestry estimates varied as a function of read counts and library type. To do so, we chose five individuals of varying genome-wide ancestry from our 150bp paired-end libraries, and five individuals from our 100bp single-end libraries, to represent the highest and lowest effective coverage we would expect with our 300,000 read cutoff. We then drew from each individual's fastq files with `seqtk sample` to create files with between 25,000 and 2,000,000 reads (or all reads in the individual's entire fastq file, if < 2,000,000). *ancestryinfer* was run in two batches, one for all paired-end data and one for all single-read data. We then calculated hybrid indices for each output file as in the main text, and visualized hybrid index as a function of read count for each individual.

Our downsampling analysis showed that decreasing read depths consistently decreased the amount of minor parent ancestry detected (Fig. S13B). However, changes in inferred ancestry in paired-end libraries were slight among files above our minimum coverage cutoff of 300,000 reads. The most extreme shift in ancestry between 300,000 reads and maximum coverage in our paired-end reads was 2.6%, suggesting that variation in read depth is unlikely to have affected the conclusions of our study. As expected given the decreased coverage per read, we found that single-read libraries may be more sensitive to read count than paired-end libraries (Fig. S13B). However, they showed similarly low variation (1.2%) due to read count above our coverage cutoff.

Supplementary Information 6. Effects of variable sample size on analyses of ancestry distributions

Our survey of genetic structure in *X. birchmanni* × *malinche* hybrid populations includes multiple sites from which we have gathered extensive genetic datasets for previous studies (1, 2). To maximize our information about the ancestry structure at different sites, we chose to include all available genomes in our overview of ancestry structure and in our site-wise applications of Hartigan's dip test (Fig. 3). However, we recognized that sample sizes varying by an order of magnitude across sites (Table S4) might complicate our interpretation of these results, and so we sought to test the effects of sample size on our ability to detect significant ancestry structure.

Since our primary concern was that low sample sizes might reduce our power to detect significant departures from a unimodal ancestry distribution, we performed a down-sampling analysis and tested its effects on our inference of population structure. Specifically, we chose to match the sample size at Pezmatlán (n = 22), the smallest sample size in the Río Calnali. Since the sample size at Pezmatlán was below the median sample size across sites (n = 32.5), this was a conservative representation of the potential effect of sample size on our analysis. For each of 12 sites with sample sizes ranging from 22 to the maximum of our study (Table S5), we drew a sample size of 22 individuals without replacement from the pool of all individuals. We then calculated Hartigan's dip statistic (*D*) for each subsampled population, and recorded the *P*-value of the dip test for unimodality. For each population, we calculated the mean *D* across 1,000 replicate subsamples, as well as the proportion of the time that we identified significant deviations from unimodality.

This analysis showed that down-sampling reduced the variance in *D* measurements between different sites included in our dataset ($\sigma^2 = 0.005$ for full-sample size *D*, 0.003 for mean down-sampled *D*). Our down-sampling analysis also suggested that our power to detect ancestry structure even at low sample sizes was dependent on the specific ancestry distribution of the population. While we could reject unimodality the overwhelming majority of the time in populations with equal frequencies of X. *birchmanni*-like and *X. malinche*-like hybrids (significance frequency = 0.976 for Aguarzarca, 0.908 for Xochicoatlán), down-sampling had much greater effects in sites with greater within-cluster variance in ancestry and in sites with unequal representation of ancestry clusters (0.845 for CALM, 0.429 for PILO, 0.285 for MXLA). In contrast, we rarely or never detected a non-unimodal ancestry distribution when sampling from a population inferred to be unimodal based on our full dataset (minimum 0.0, maximum 0.001).

Finally, we performed a simple Pearson's correlation between the sample size of a site and the *D* statistic inferred from our full genetic dataset. We found that the relationship between this metrics was negative but not significant ($\rho = -0.252$, $t = -1.71$, $P = 0.095$), implying that any effect of sample size variation might be to inflate signals of multimodality at low sample sizes. Given that the majority of our sites showing significant departures from unimodality had larger sample sizes (minimum 29, all others >51) we took this as a sign that our results reflected true positives, rather than false positives from under-sampling a distribution of high variation.

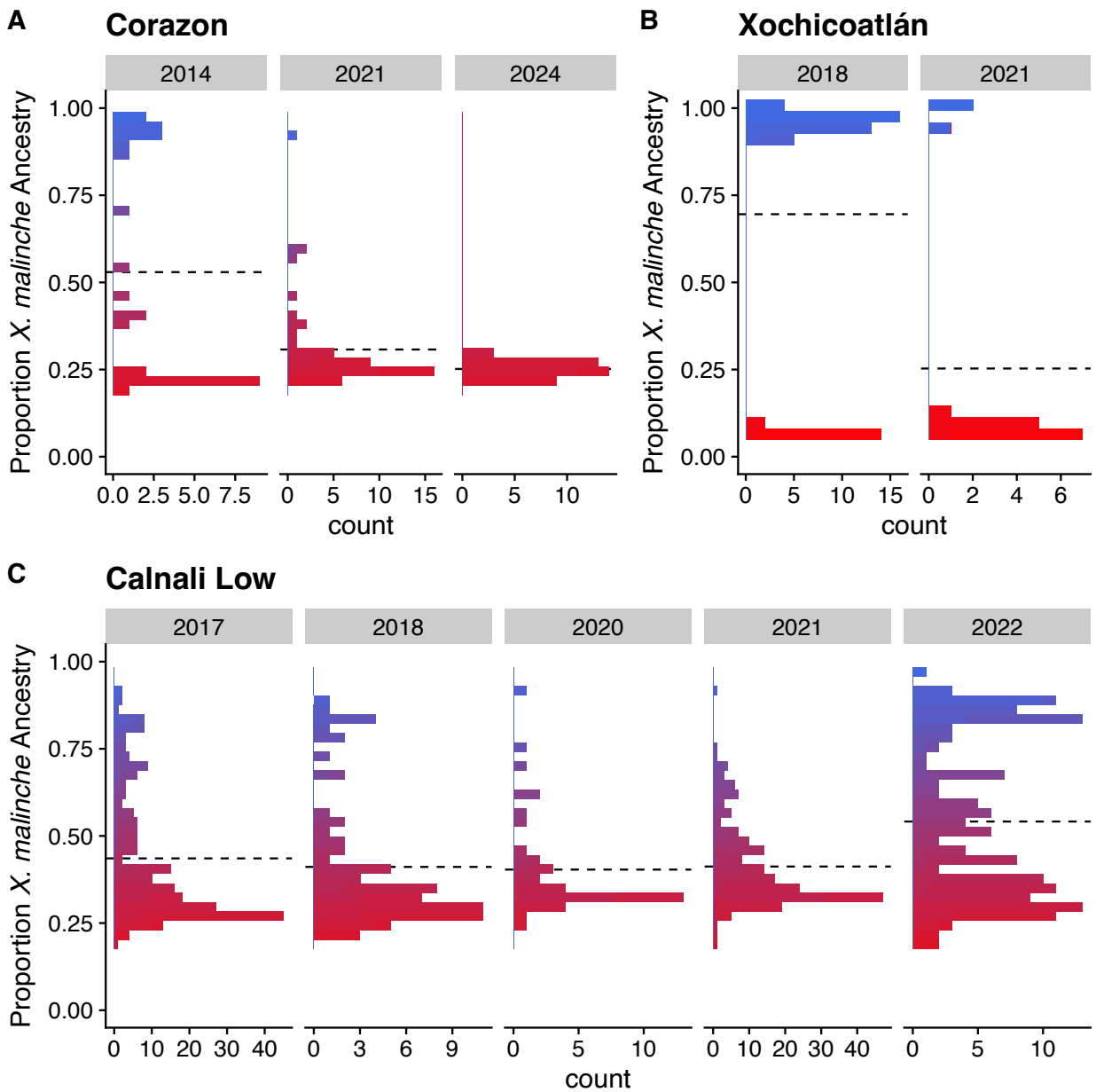

Figure S1. Ancestry distributions across sampling years at sites where we detected significant differences in ancestry distribution over time (Supp. Info 2). **A)** Distribution of individual ancestry across years at the Corazón site on the Río Huazalingo. **B)** Distribution of individual ancestry across years at the Xochicoatlán site on the Río Conzintla. **C)** Distribution of individual ancestry across years at the Calnali Low site on the Río Calnali. The y-axis denotes the proportion of the genome derived from the *X. malinche* parent (i.e. 1 is equivalent to 100% *X. malinche* ancestry genome wide). The height of bars on the x-axis indicates the number of individuals in that ancestry bin. Based on Hartigan's dip statistic, we reject a unimodal ancestry distribution at the Corazón site in 2018 (dip test $D = 0.132$, $P = 0.0002$), at the Xochicoatlán site in 2018 (dip test $D = 0.141$, $P < 1e\text{-}11$) and Calnali Low in 2022 (dip test $D = 0.066$, $P = 0.00002$).

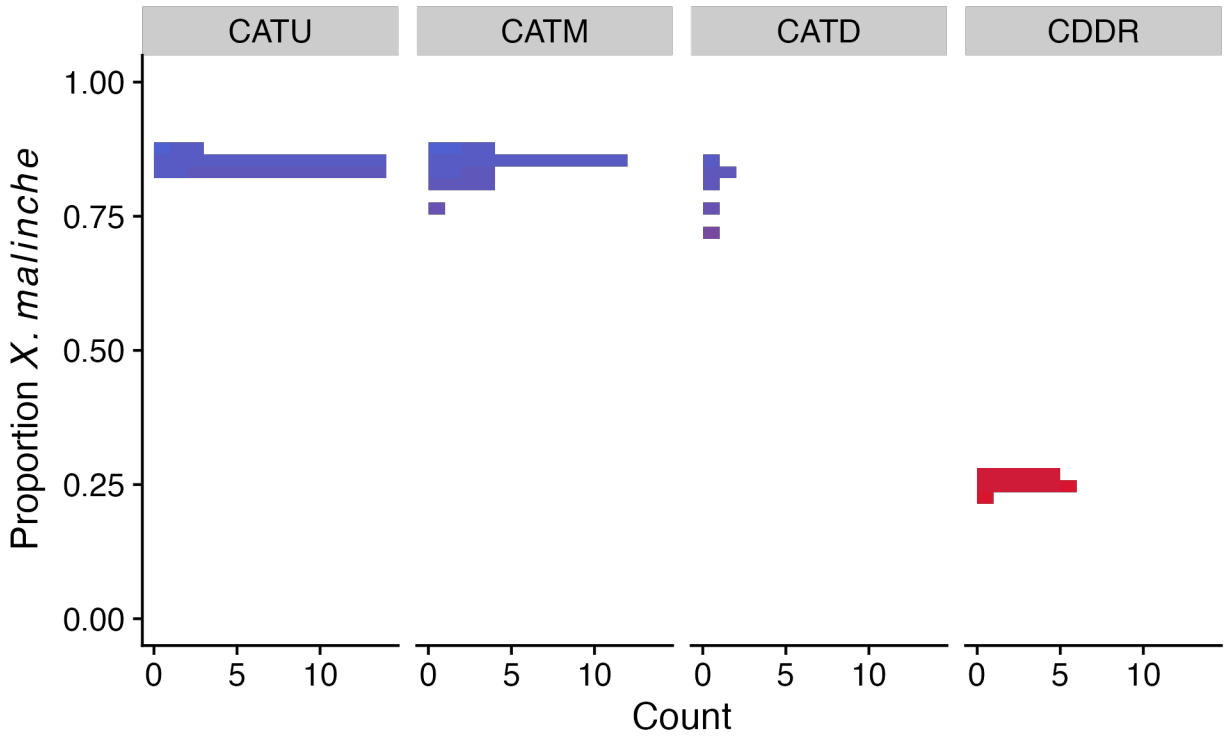

Figure S2. Ancestry distributions in four tributaries that flow into the Río Calnali between the sites of Calnali Low and Tlalica. Sites are arranged with upstream sites on the left side of the x-axis, and downstream sites on the right. Each plot shows the distribution of genome wide ancestry for individuals sampled at that site on the y-axis, and the height of the bars corresponds to the number of individuals in that ancestry bin on the x-axis. Ancestry is plotted in terms of the proportion of the genome derived from *X. malinche*, with 1 corresponding to 100% *X. malinche* ancestry. Abbreviations: CATU – Calnali Tributary Up, CATM – Calnali Tributary Mid, CATD – Calnali Tributary Down, CDDR – Ciudad de Ranas.

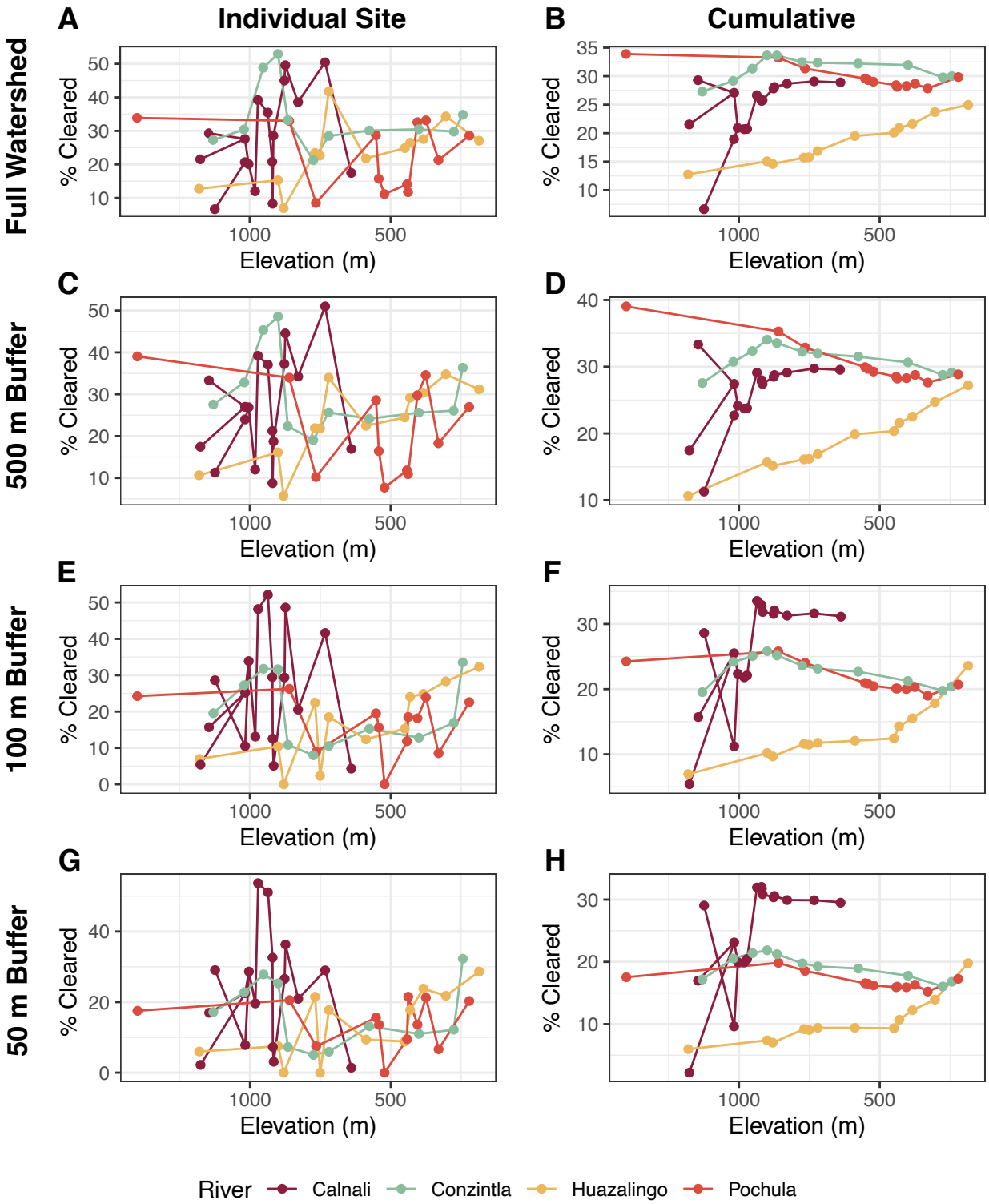

Figure S3. Proportion of land cover identified as cleared land (non-native vegetation, grasslands, and pasture) in each watershed in 2020–2023 based on analysis in ArcGIS Pro. The left column shows the proportion at each site, based on analysis of the subcatchment between that site and the site directly upstream (see Fig. S6). The right column shows the cumulative subcatchment of all sections of the stream upstream of a given site. The first row shows calculations incorporating

pixels at any distance from a stream within the focal subcatchment area, while lower rows show calculations limited to pixels within **C–D)** 500 meters, **E–F)** 100 meters, or **G–H)** 50 meters of a stream. Streams were designated as pixels with accumulated flow > 3000 cells, depicted with blue lines in Fig. 5A. Points represent sites, lines connect sites in the order in which they occur on the stream (note that Calnali line branches due to inclusion of multiple headwater tributaries). Colors correspond to the stream, see legend below plots.

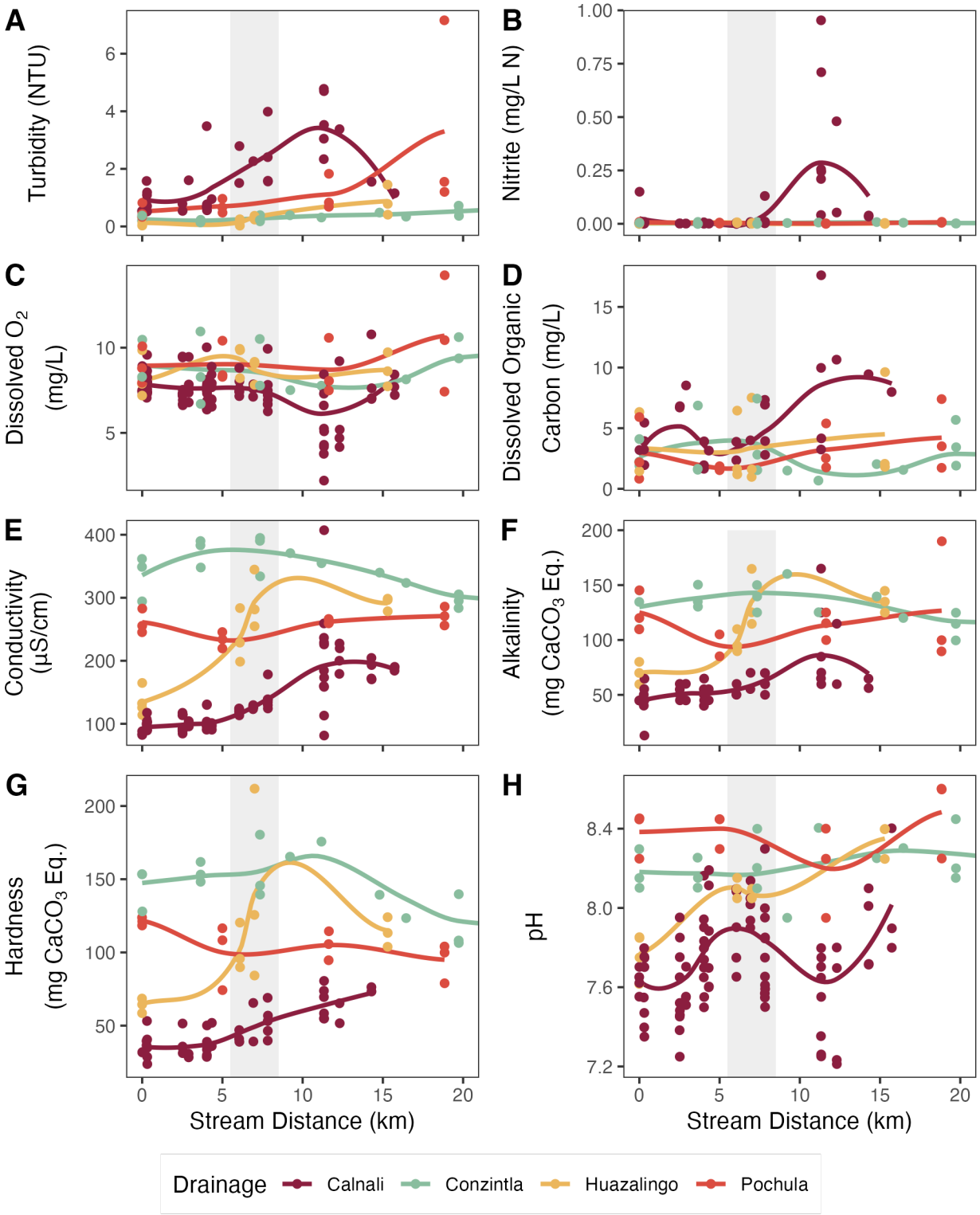

Figure S4. Plots of non-metal water quality parameters along each stream. Points represent individual samples. Numbers on the x-axis correspond to the position along the stream with, with 0 indicating the most upstream site sampled. Lines are LOESS curves fit through data for each stream, and gray bars indicate the span in which the Río Calnali passes through the town of Calnali. Subplots represent **A)** turbidity, in nephelometric turbidity units, **B)** nitrite, in mg N/L,

C) dissolved oxygen, in mg O_2/L, **D)** dissolved organic carbon from Shimadzu TOC-L analyzer, in mg C/L. **E)** total (special) conductivity, in µS/cm **F)** alkalinity, in $CaCO_3$ equivalents, **G)** total hardness, in $CaCO_3$ equivalents, and **H)** pH.

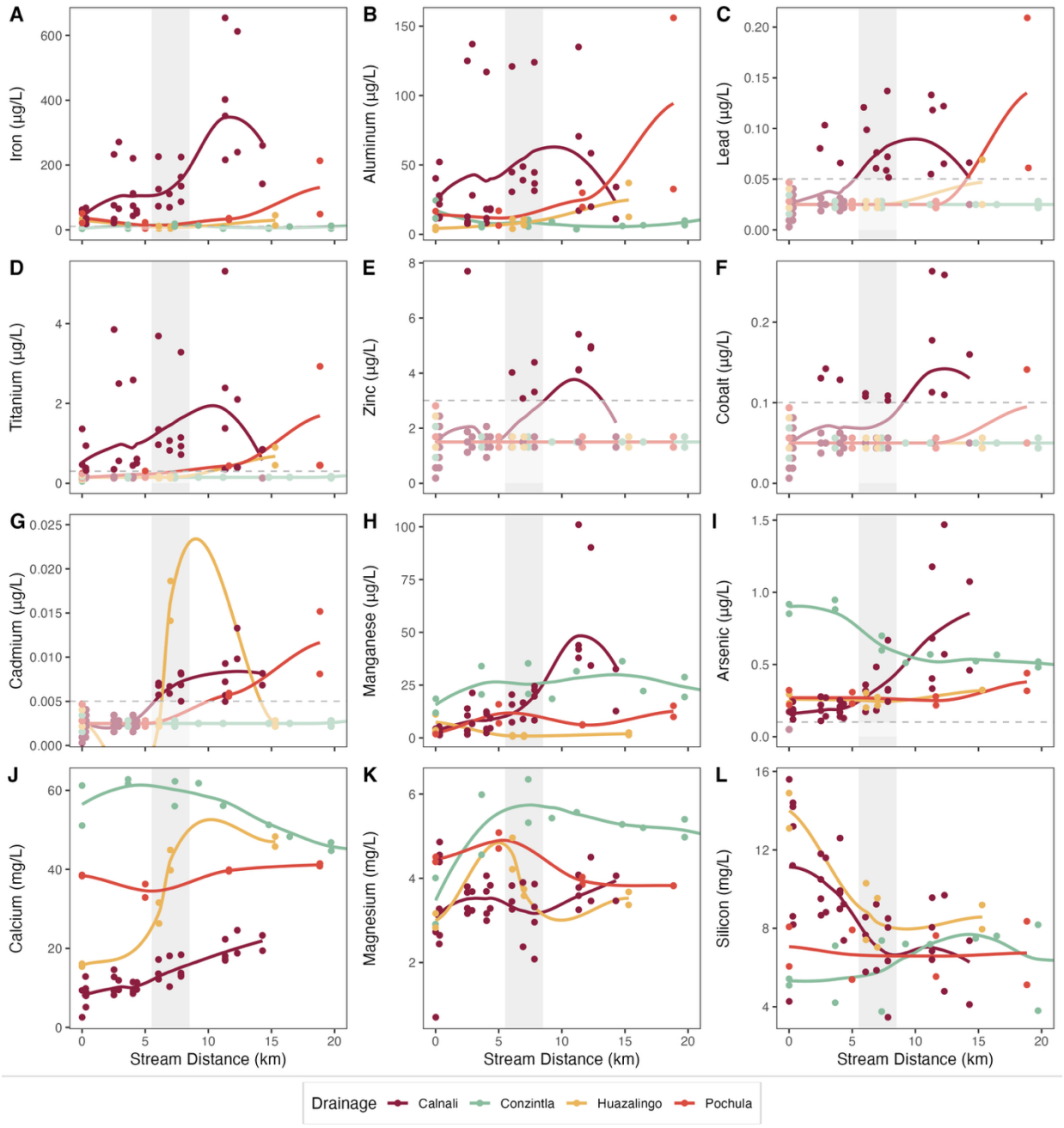

Figure S5. Plots of ICP-MS water quality parameters along each stream. **A–F)** Ions that were detected as particularly elevated in sampling sites downstream of the town of Calnali. **G–L)** Ions that varied between streams. Points represent individual samples. Numbers on the x-axis correspond to the position along the stream with, with 0 indicating the most upstream site sampled. Values on the y-axis correspond to measurements of the chemical parameter sampled, and color denotes stream of sampling (see legend at bottom). Lines are LOESS curves fit through data for each stream. Results for **A)** Iron **B)** Aluminum **C)** Lead **D)** Titanium **E)** Zinc **F)** Cobalt, **G)** Cadmium **H)** Manganese **I)** Arsenic **J)** Calcium **K)** Magnesium and **L)** Silicon. Grey shaded area denotes the sites located within the town of Calnali on the Río Calnali transect. Dashed horizontal lines and translucent zones in **C–G)** and **I)** represent measurements that fell below the detection limit of the ICP-MS assay. Points below this limit are arbitrarily plotted at half the

detection threshold, with jittering for visualization. Note that these values below the line do not represent point estimates of the ion concentrations.

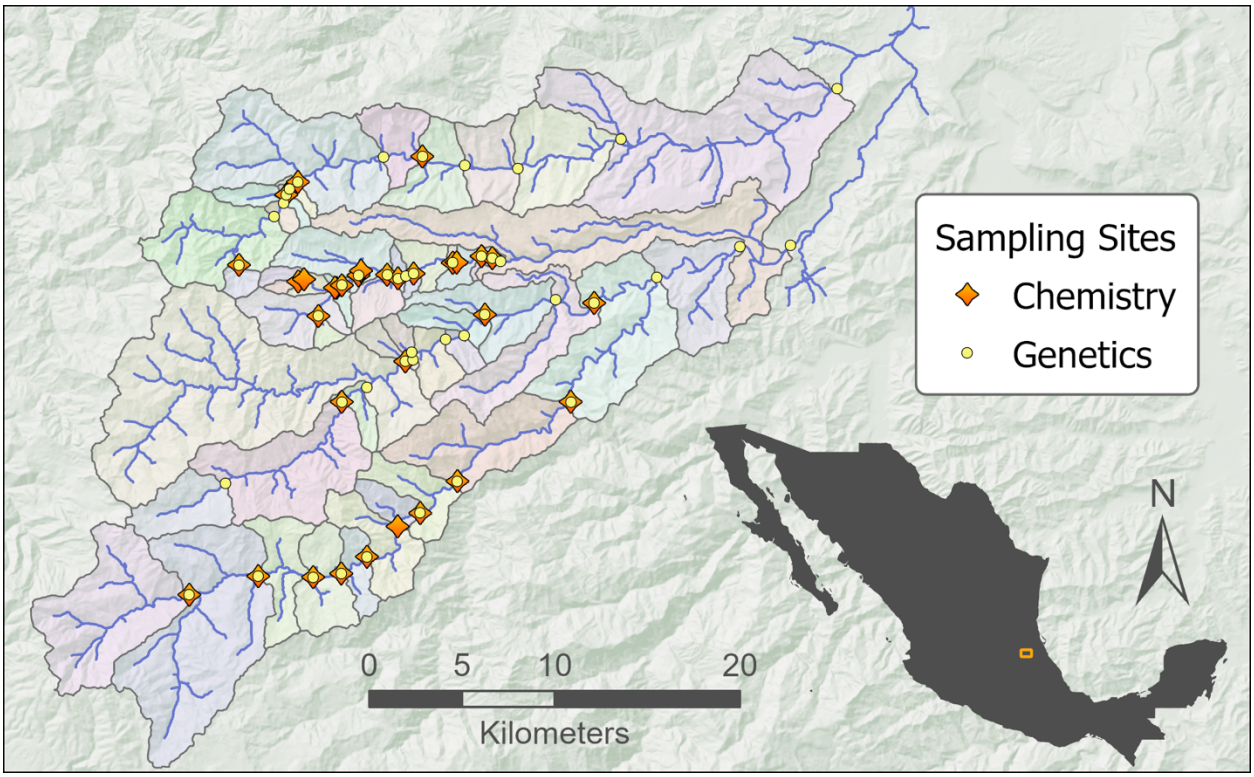

Figure S6. Locations of sampling sites overlaid with the inferred subcatchment of each site. Streams are shown as blue lines, sites where fish were collected are yellow circles, and sites where water chemistry data were collected are orange diamonds. The subcatchment draining to each site is indicated with translucent shaded areas separated by dark lines. Note that the full drainage of each site includes all subcatchments upstream of it (i.e. not only the closest subcatchment, but all the subcatchments of all upstream sites).

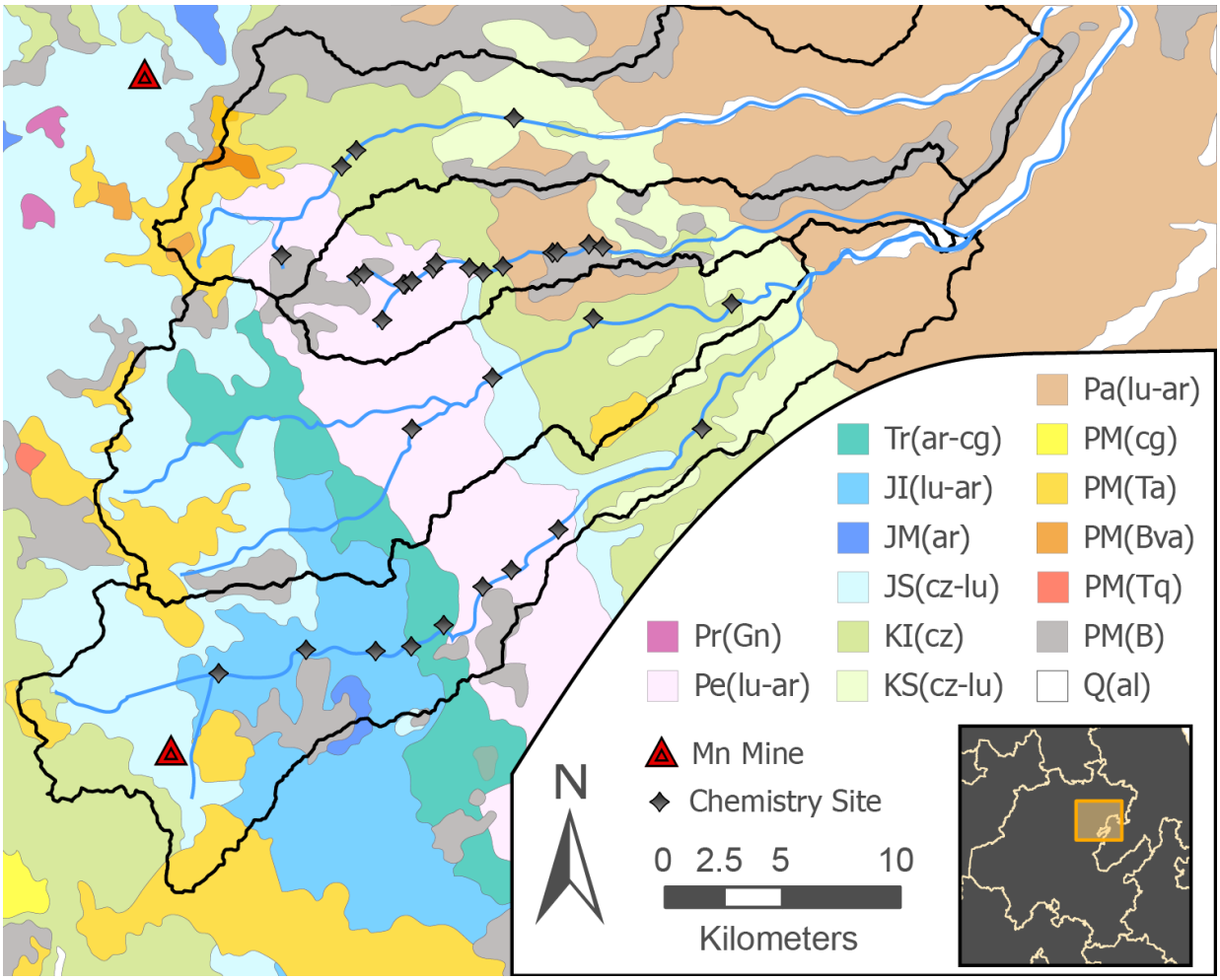

Figure S7. Geological features underlying the sampled stream drainages in the Atlapexco Basin. Black outlines denote drainage area for the four different streams included in this study. From top to bottom these streams are the Río Huazalingo, Río Calnali, Río Pochula, and Río Conzintla. Blue lines show streams, gray points show the sites of water chemistry sampling, and red triangles denotes locations of open-pit manganese mines. This geological map was adapted from the Mexican National Institute of Statistics and Geography (INEGI) (3). The color represents age and type of bedrock. The abbreviations in the legend include text outside parentheses specifying geological age (Pr – Precambrian; Pe – Permian; Tr – Triassic; JI – Inferior Jurassic; JM – Middle Jurassic; JS – Superior Jurassic; KI – Inferior Cretaceous; KS – Superior Cretaceous; Pa – Paleogene; PM – Pliocene/Miocene; Q – Quaternary) and inside parentheses indicating rock type (al – alluvial soil; ar – sandstone; B – basalt; Bva – acidic volcanic breccia; cg – conglomerate; cz – limestone; Gn – gneiss; lu – mudstone; Ta – acidic tuff; Tq – trachyte).

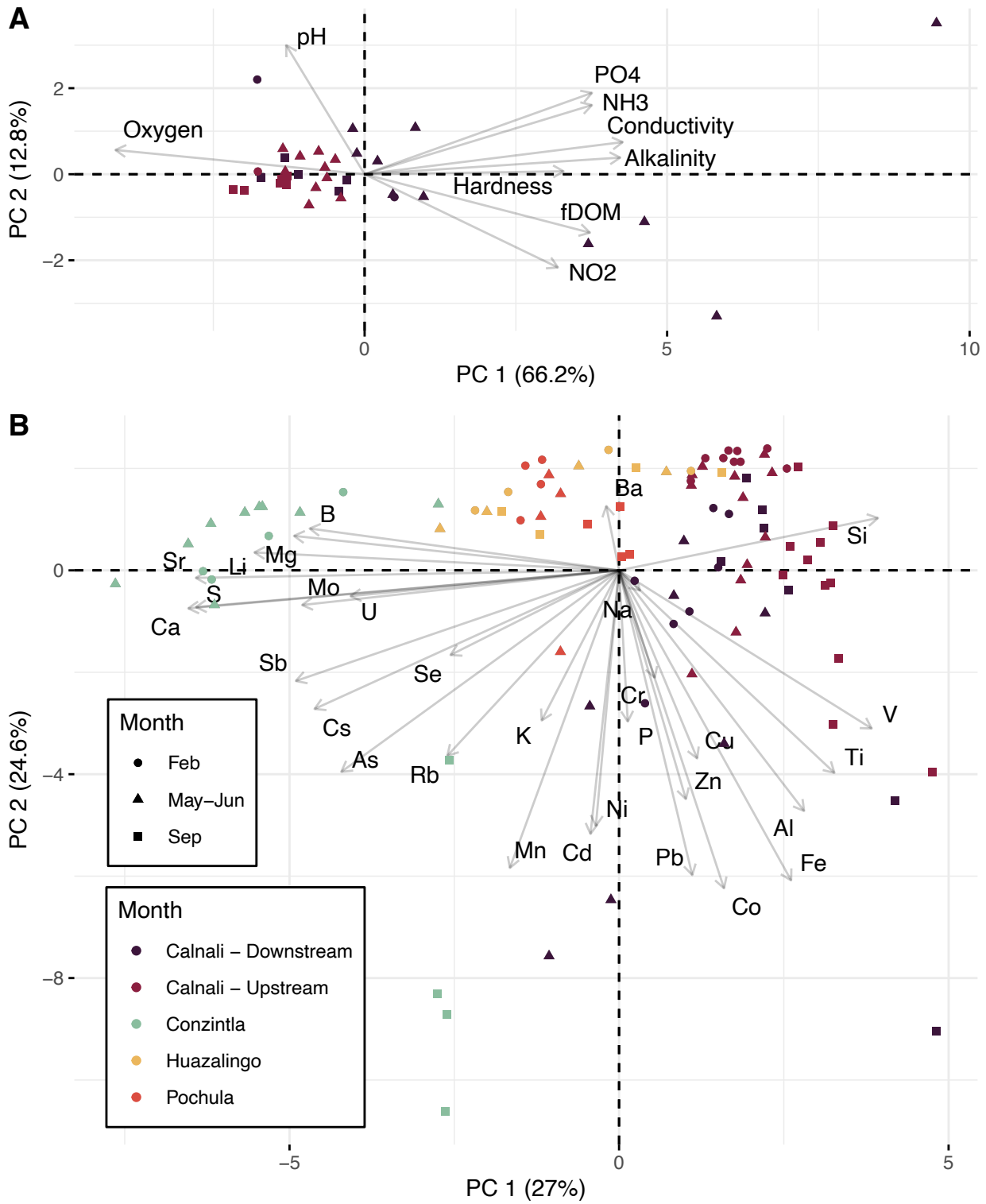

Figure S8. Principal component analysis of water chemistry data highlighting **A)** temporal variation in the Río Calnali in non-metals data and **B)** ICP-MS metals data from all sites and dates. PCAs were constructed as in main text, except for inclusion of data from the rainy season in September; sulfate measurements were not collected at that timepoint, and thus this parameter was omitted from the non-metals PCA. Points represent individual sampling events, with shape

and color denoting sampling month and drainage, respectively. Arrows and text show loading of variables on first two principal components. Proportion of variance explained is indicated parenthetically on the x and y axes.

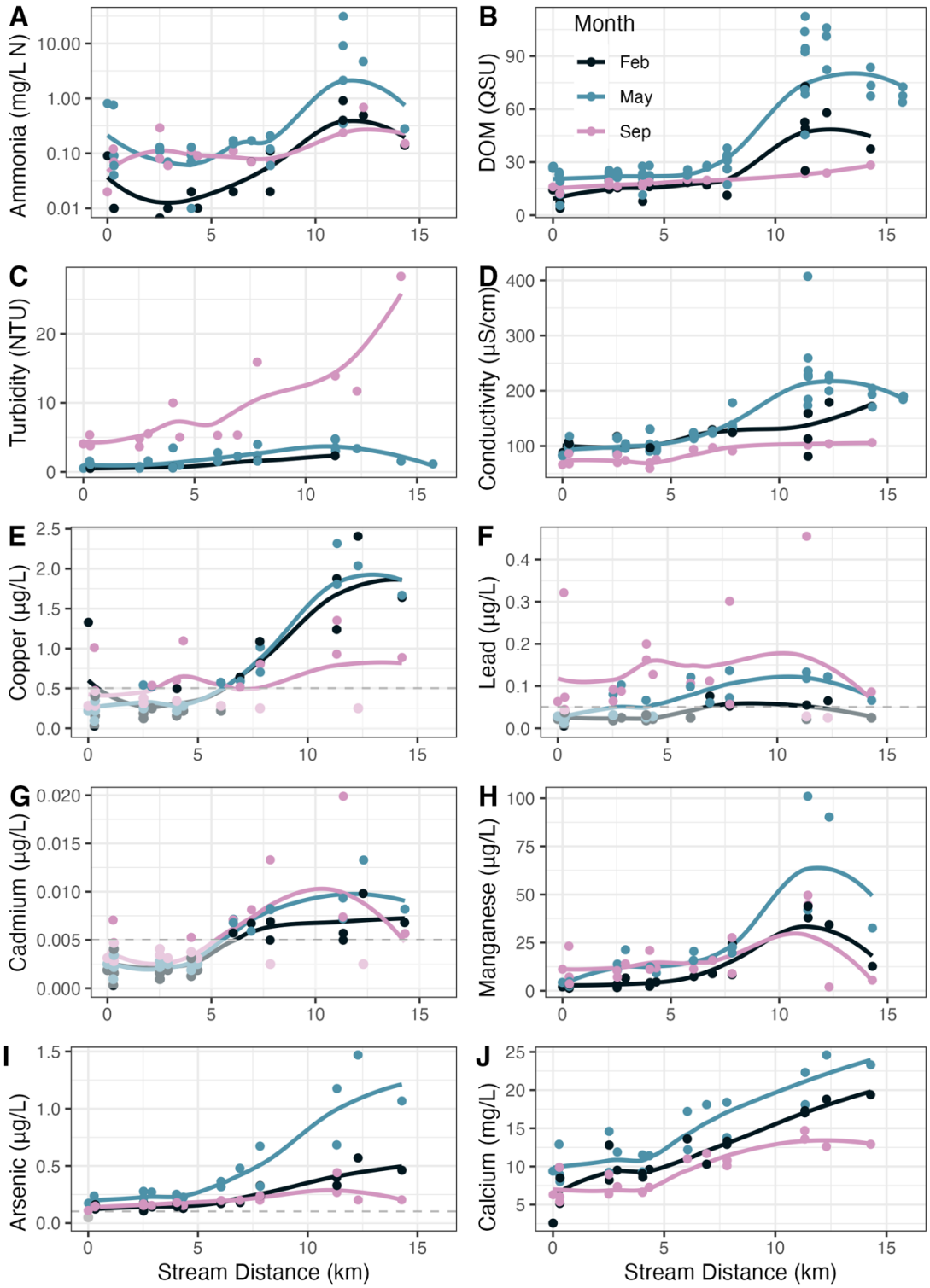

Figure S9. Temporal variation in water chemistry along the Río Calnali for various water chemistry parameters. Points represent sampling events, and x-axis indicates sampling site position along the length of the Río Calnali. Zero corresponds to the highest elevation site sampled. Values on the y-axis correspond to measurements of the chemical parameter sampled, and the color denotes month of sampling. Lines are LOESS curves fit to this data. Dashed line

and translucent zones in **E)**, **F)**, **G)**, and **I)** indicate measured values below the detection limit of the ICP-MS assay. Points below this limit are plotted at half the detection threshold, with jittering to prevent overlap and visually represent sample size, but do not represent point estimates of the concentration. Abbreviations: DOM = fluorescent Dissolved Organic Matter; QSU = quinine sulfate units; NTU = nephelometric turbidity units.

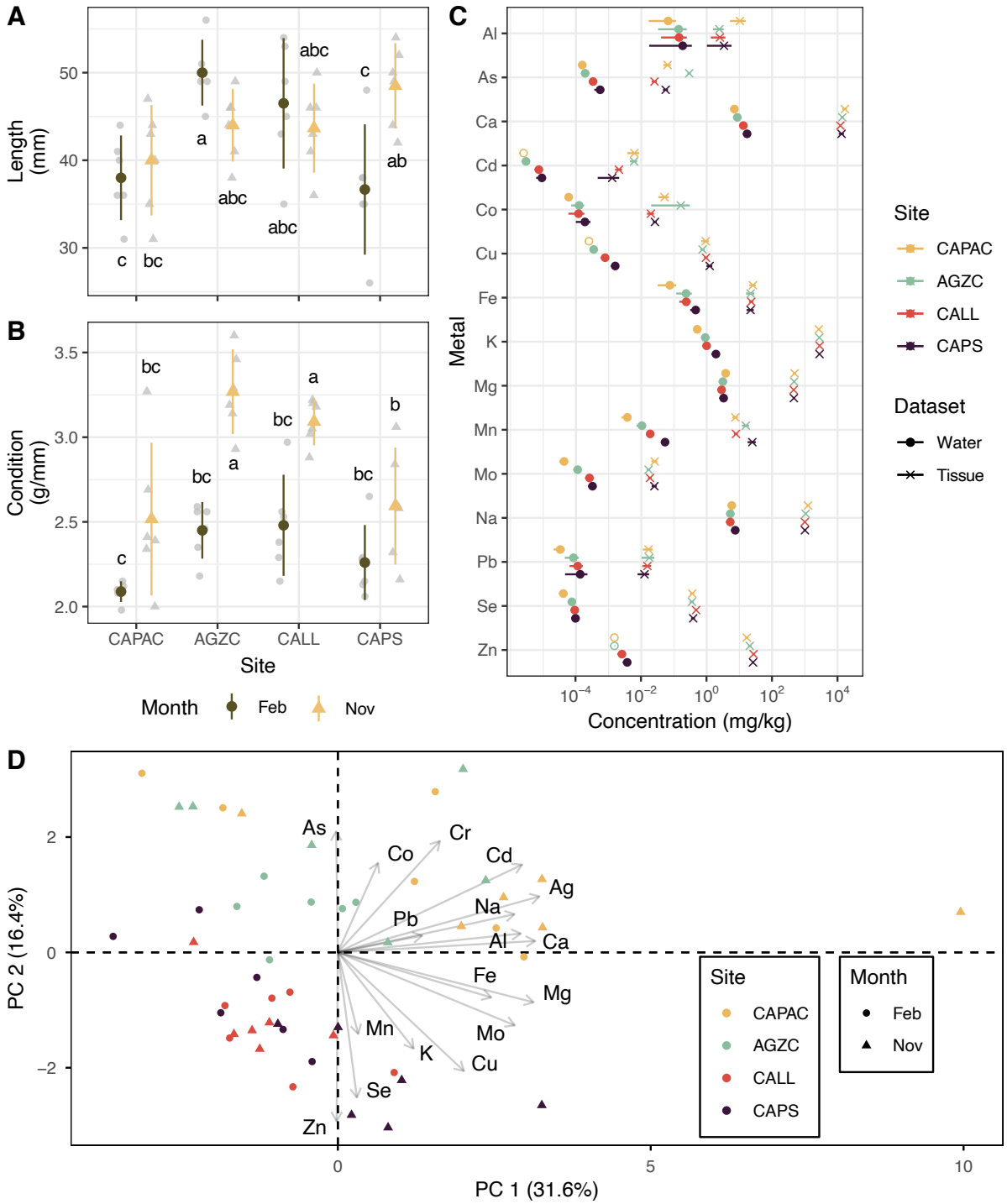

Figure S10. ICP-MS metal analysis of fish tissue from four sites on the Río Calnali. Two sites (CAPAC and AGZC) are located upstream of the town of Calnali, and the others (CALL and CAPS) are located downstream of the town. **A–B)** Length (**A**) and condition factor (**B**) of fish collected for ICP-MS, separated by site and collection month. Gray points represent individual samples, colored points and bars represent group mean ± 2 standard errors. Letters denote statistical differences from Tukey's HSD test. **C)** Concentrations of metals from ICP-MS measurements, compared between water (•) and fish tissue (×). y-axis separates each metal

tested, color denotes sampling site, and points and error bars represent mean ± 2 SE concentration for each site. Error bars are invisible in some cases due to small variance relative to the x-axis scale. Open circles denote sites and metals for which all values were below the detection limit, in which case the point was arbitrarily placed at one half the detection limit. All tissue measurements were above detection limits. **D)** Principal component analysis of metal concentrations from whole fish tissue. Points represent individual sampled fish, with shape and color denoting sampling month and site, respectively. Arrows and text show loading of variables on first two principal components. Proportion of variance explained is indicated parenthetically on the x and y axes.

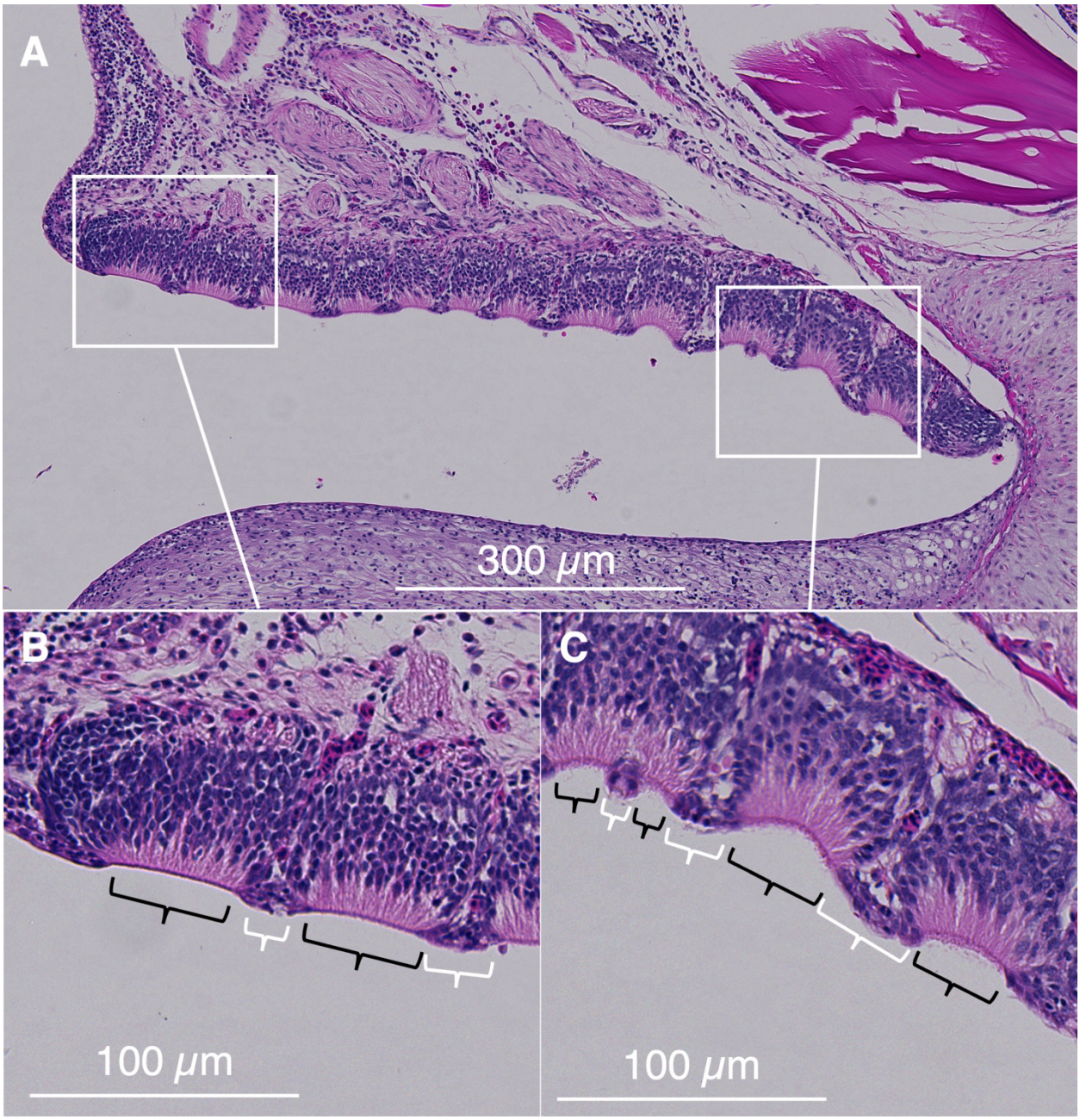

Figure S11. Representative images of hematoxylin & eosin (H&E) stained slides of *Xiphophorus birchmanni* × *malinche* hybrid olfactory rosettes. **A)** Overview of entire olfactory rosette. Sensory epithelial beds are visible due to eosinophilic (pink) apical surface of sensory neurons, with basophilic (purple) surface cells visible in the intervening non-sensory epithelial surface. **B)** Zoomed image of region with cilia absent from sensory beds. Sensory beds are indicated by black brackets, non-sensory ridges by white brackets. **C)** Zoomed image of region with cilia present in sensory beds. Brackets indicate sensory beds and non-sensory ridges as in **B)**. Note that images were taken at 400X magnification with a Cytation 5 slide scanner, but cilia were quantified at 1,000X magnification using a compound microscope.

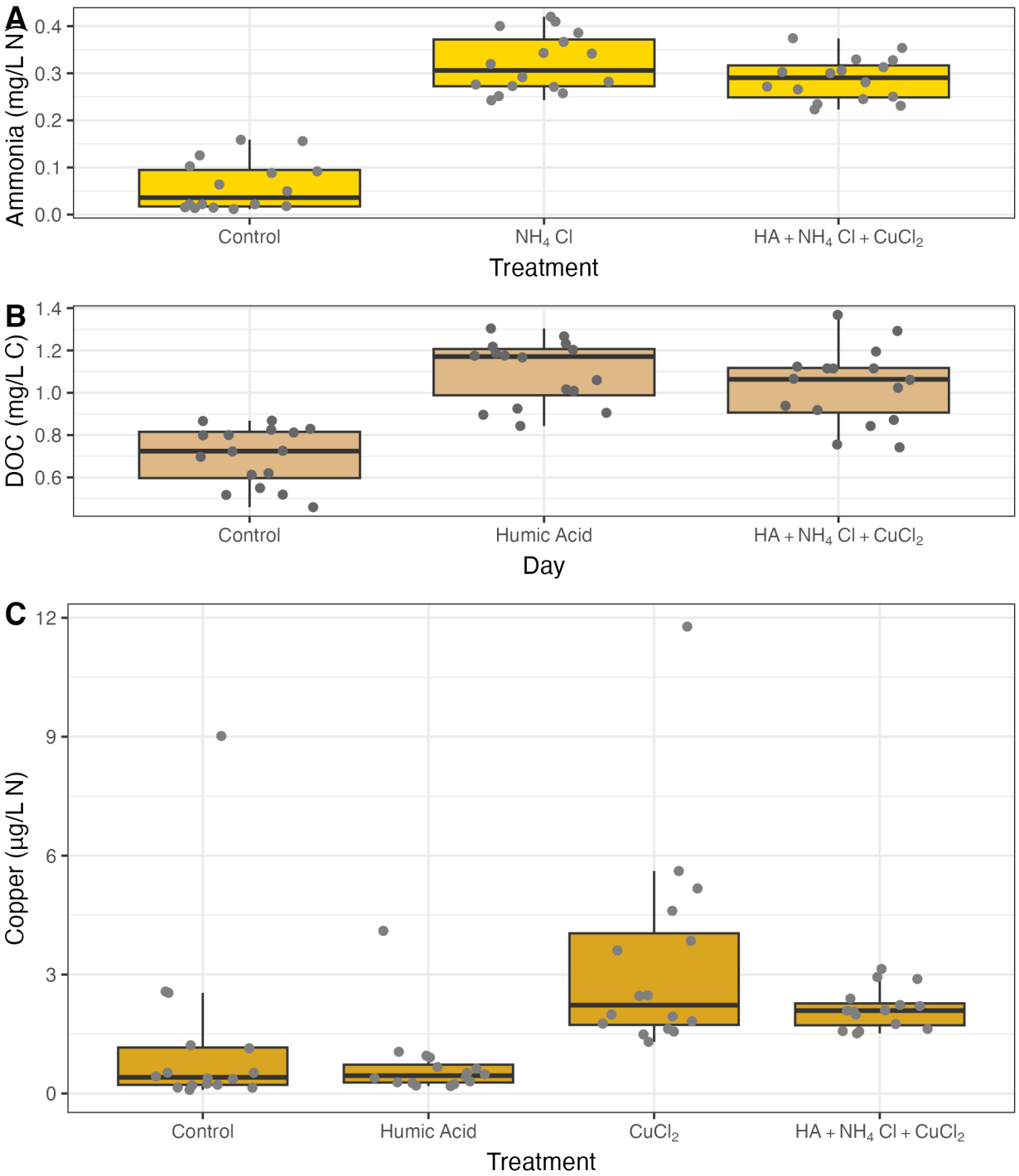

Figure S12. Water chemistry parameters measured during laboratory treatments testing chemical effects on olfactory histology (Supp. Info 8). Individual water samples, which are shown as gray points, were taken from each tank at the start of each trial, before and after daily water changes, and at the end of the trial. **A)** Ammonia, measured as NH_4. **B)** Dissolved organic carbon, measured as non-purgeable organic carbon. **C)** Copper measured by ICP-MS. In general, testing was performed on the no-manipulation control treatment and the two treatments in which the tested parameter was directly manipulated. However, the Humic Acid (HA) treatment was also

452 tested for its effect on copper levels due to previous reports of heavy metals in commercially
453 purchased humic acid (11).

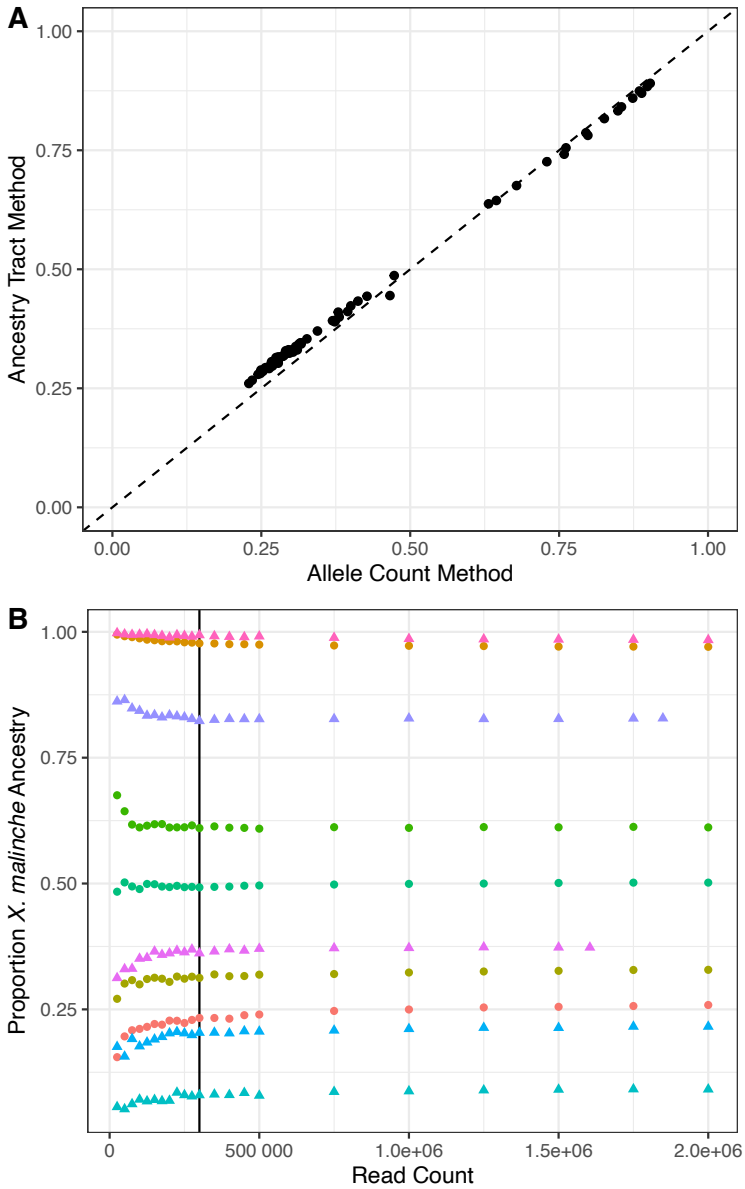

Figure S13. A) Comparison of different approaches for estimating ancestry fraction. Individuals plotted here represent 73 samples from the Plaza (PLAZ) site. On the x-axis, the proportion of the genome derived from *X. malinche* was estimated based on allele counts at ancestry informative markers. On the y-axis, the proportion of the genome derived from *X. malinche* was estimated using the lengths of ancestry tracts inferred to belong to a particular ancestry state (homozygous *X. malinche*, heterozygous, or homozygous *X. birchmanni*). The dotted line represents the expected 1:1 relationship between these estimation methods. **B)** Downsampling analysis testing sensitivity of genome-wide ancestry fraction estimates to read counts and library type. Five individuals from 150bp paired-end sequencing runs (circles) and five individuals from 100bp single-read runs (triangles) were downsampled to varying coverage before ancestry inference, with the number of reads sampled represented on the x-axis, and the inferred genome-wide ancestry fraction on the y-axis. Colors distinguish ancestry runs from reads of the same individual, and the vertical line denotes the read count cutoff used in the main text (300,000 reads).

Table S1. List of sampling locations included in this study. Lat – Latitude, Lon – Longitude. T indicates that genetic data or water chemistry data was collected for that site, F indicates that it was not.

#	*Drainage*	*Site Name*	*Site Code*	*Lat*	*Lon*	*Elevation*	*Genetic*	*Water*
1	Huazalingo	Veneno	VNNO	20.90358	-98.6601	1180	T	T
2	Huazalingo	Cansada	CNSD	20.926981	-98.643206	900	T	F
3	Huazalingo	Cascada	CSCD	20.933614	-98.638419	880	T	F
4	Huazalingo	Corazón	CRZN	20.93761	-98.63713	769	T	T
5	Huazalingo	Totonicapa to Cascade Pool 1	TCP1	20.940231	-98.635508	751	T	F
6	Huazalingo	Totonicapa	TOTO	20.94379	-98.63151	720	T	T
7	Huazalingo	Acahuasco Low	AHLW	20.955858	-98.59015	588	T	F
8	Huazalingo	Acuapa	ACUA	20.95618	-98.57121	450	T	T
9	Huazalingo	Pilcuatla	PILC	20.951744	-98.550669	431	T	F
10	Huazalingo	San Pedro	SNPD	20.950418	-98.524769	384	T	F
11	Huazalingo	Tlatzonco	TLZO	20.964663	-98.474852	304	T	F
12	Huazalingo	Achiquihuixtla	ACHI	20.989106	-98.370194	186	T	F
13	Calnali	Calnali High South	CAHS	20.89553	-98.63139	1176	F	T
14	Calnali	Calnali High	CALH	20.8966	-98.62859	1145	F	T
15	Calnali	CAPASC Fuente de Agua	CAPAC	20.87878	-98.62159	1124	T	T
16	Calnali	Calnali Branch South	CABS	20.8924	-98.61285	1017	F	T
17	Calnali	Calnali Branch North	CABN	20.89252	-98.61352	1017	F	T
18	Calnali	Calnali Mid	CALM	20.89366	-98.61024	1004	T	T
19	Calnali	Aguazarca	AGZC	20.8985	-98.60215	981	T	T
20	Calnali	Plank	PLNK	20.90074	-98.60091	971	F	T
21	Calnali	Piloncillo	PILO	20.89883	-98.58828	936	T	T
22	Calnali	Plaza	PLAZ	20.89704	-98.58302	920	T	T
23	Calnali	Peatonal	PEAT	20.898047	-98.579144	919	T	F
24	Calnali	Calnali Low	CALL	20.89936	-98.57544	916	T	T
25	Calnali	Tlalica	CAPS	20.90459	-98.55644	877	T	T
26	Calnali	Tlalica Down	TLCD	20.90475	-98.55456	874	F	T
27	Calnali	Pezmatlán	PEZM	20.90778	-98.5425	829	T	T
28	Calnali	Chahuaco Falls	CHAF	20.90689	-98.53726	733	T	T
29	Calnali	Gilroy	GILR	20.905331	-98.533239	640	F	T
30	Pochula	Culhuacán	CULH	20.797511	-98.666703	1400	T	F
31	Pochula	Texcaco	TEXC	20.83716	-98.61026	860	T	T

32	Pochula	Cascada Real	CSRL	20.844025	-98.597997	765	T	F
33	Pochula	Pochula	POCH	20.85677	-98.57946	552	T	T
34	Pochula	Pochula Low	PHLW	20.857669	-98.575858	542	T	F
35	Pochula	Ocotepec	OCOT	20.861167	-98.576208	522	T	F
36	Pochula	Islet	ISLT	20.867308	-98.559903	442	T	F
37	Pochula	Pico de Aguila	PICO	20.869431	-98.550997	438	T	F
38	Pochula	Tula	TULA	20.87946	-98.54086	405	T	T
39	Pochula	Bicho	VCHO	20.886817	-98.506633	375	T	F
40	Pochula	Atempa	ATEM	20.8851	-98.4879	330	T	T
41	Pochula	Papatlatla	PAPA	20.8975	-98.4575	276	T	F
42	Conzintla	Coatitlamixtla	CTMX	20.74362	-98.6842	1130	T	T
43	Conzintla	Xochicoatlán	XOCH	20.75265	-98.65074	1020	T	T
44	Conzintla	Mixtla	MXLA	20.75217	-98.62412	952	T	T
45	Conzintla	Mazahuacán	MZHC	20.75393	-98.6105	900	T	T
46	Conzintla	Tlaxcoya	TLCY	20.76208	-98.59806	865	T	T
47	Conzintla	La Esperanza	LESP	20.77676	-98.58318	775	F	T
48	Conzintla	Papaxtla	PPXL	20.78322	-98.5722	720	T	T
49	Conzintla	Otlamalacatla	OMCA	20.79871	-98.55421	576	T	T
50	Conzintla	Zacatipán	ZACA	20.837186	-98.499236	400	T	T
51	Pochula	Huiznopala	HZNP	20.912376	-98.417092	244	T	F
52	Pochula	El Arenal	AREN	20.913033	-98.392794	221	T	F
53	Cal Trib	Calnali Tributary Up	CATU	20.902586	-98.573572	926	T	F
54	Cal Trib	Calnali Tributary Middle	CATM	20.904600	98.569500	925	T	F
55	Cal Trib	Calnali Tributary Down	CATD	20.907700	98.565900	929	T	F
56	Cal Trib	Ciudad de Ranas	CDDR	20.905225	-98.557397	892	T	F

Table S2. List of genetic sample sizes by location and date. Site codes match those in Table S1.

Drainage	*Site Code*	*Year*	*# Collected*
Huazalingo	VNNO	2014	40
	CNSD	2015	26
	CSCD	2014	19
	CRZN	2014	28
		2021	46
		2024	39
	TCP1	2014	31
	TOTO	2013	16
		2014	120
		2015	91
	AHLW	2016	19
	ACUA	2013	36
		2015	13
	PILC	2013	32
	SNPD	2013	22
	TLZO	2013	28
		2014	10
	ACHI	2014	15
		2016	4
Calnali	CAPAC	2017	23
	CALM	2021	79
	AGZC	2016	51
	PILO	2012	26
		2017	54
	PLAZ	2017	73
	PEAT	2017	37
	CALL	2017	234
		2018	74
		2020	38
		2021	201
		2022	155
	CAPS	2021	12
		2022	24
	PEZM	2016	22
	CHAF	2017	50
		2018	138
		2019	60
	GILR	2019	23

Drainage	*Site Code*	*Year*	*# Collected*
Pochula	CULH	2015	26
	TEXC	2015	23
	CSRL	2015	16
	POCH	2015	17
		2016	22
	PHLW	2016	19
	OCOT	2016	26
	ISLT	2016	36
	PICO	2016	39
	TULA	2015	33
	VCHO	2016	14
		2017	31
	ATEM	2015	14
		2017	23
	PAPA	2006	4
		2008	9
Conzintla	CTMX	2023	54
	XOCH	2018	54
		2021	16
	MXLA	2022	29
	MZHC	2023	17
	TLCY	2023	12
	PPXL	2023	19
	OMCA	2023	19
	ZACA	2019	19
	HZNP	2006	24
		2007	2
	AREN	2016	39
Calnali	CATU	2020	6
Tributary	CATM	2020	25
	CATD	2020	31
	CDDR	2021	12

Table S3. Metadata for water chemistry measurements. The first two sheets list sample sizes for all water chemistry variables, the first excluding measurements from September as in the main text analysis, and the second for all timepoints. The next sheet provides a key connecting ICP-MS sample codes in subsequent sheets to locations and sampling times provided in the publication. Subsequent sheets provide detailed ICP-MS results for each sample, results of technical duplicates and quality control samples, methodology used, holding time exceedances, and detection limits for each ion. (Provided as Excel file)

Table S4. Ancestry statistics for sites included in the genetic sampling dataset. Mean and standard deviation in ancestry are based on individual measurements of the proportion of ancestry informative markers derived from *X. malinche*, with 0 indicating pure *X. birchmanni* and 1 indicating pure *X. malinche*. *D* statistic and *P*-value are from Hartigan's Dip Test for unimodality. Asterisks denote sites that significantly departed from unimodality, even after Bonferroni correction for multiple testing. Daggers denote sites that significantly departed from unimodality in a subset of sampling years but not across all sampling years (See Supp. Info 2). Sites are ordered upstream to downstream within each drainage.

Drainage	***Site Code***	***Sample Size***	***Mean Ancestry***	***Std. Dev. Ancestry***	**D *Statistic***	**P-*value***	***Bonferroni Significance***
Calnali	CAPAC	23	0.982	0.002	0.0632119	0.664125	
	CALM	79	0.647	0.347	0.1597263	0	*
	AGZC	51	0.584	0.351	0.2146567	0	*
	PILO	80	0.490	0.284	0.1161647	0	*
	PLAZ	73	0.414	0.215	0.0453731	0.320643	
	PEAT	37	0.391	0.184	0.0637864	0.274838	
	CALL	702	0.448	0.190	0.0108287	0.896476	
	CAPS	36	0.503	0.148	0.0692381	0.182777	
	PEZM	22	0.628	0.154	0.0617895	0.737224	
	CHAF	248	0.686	0.105	0.0146906	0.990367	
	GILR	23	0.689	0.082	0.0637874	0.647471	
Conzintla	CTMX	54	0.996	0.010	0.0328751	0.965143	
	XOCH	70	0.594	0.438	0.1924042	0	*
	MXLA	29	0.374	0.383	0.1281781	0.000211	*
	MZHC	17	0.090	0.018	0.0773580	0.538903	
	TLCY	12	0.117	0.084	0.0870907	0.599963	
	PPXL	19	0.082	0.016	0.0567116	0.916779	
	OMCA	19	0.085	0.013	0.0502825	0.980973	
	ZACA	19	0.169	0.015	0.0800843	0.385644	
	HZNP	26	0.162	0.017	0.0569652	0.747239	
	AREN	39	0.174	0.013	0.0490792	0.693023	
Huazalingo	VNNO	40	0.986	0.002	0.0405727	0.919785	
	CNSD	26	0.984	0.002	0.0540566	0.821784	
	CSCD	19	0.988	0.014	0.1129799	0.032045	
	CRZN	113	0.343	0.213	0.0319384	0.586268	†
	TCP1	31	0.246	0.116	0.0512672	0.78897	
	TOTO	227	0.245	0.117	0.0161153	0.98159	
	AHLW	19	0.208	0.021	0.0468443	0.991205	
	ACUA	49	0.202	0.025	0.0373504	0.91452	
	PILC	32	0.101	0.016	0.0491217	0.825054	
	SNPD	22	0.088	0.022	0.0793971	0.29282	

	TLZO	38	0.081	0.008	0.0501598	0.675376
	ACHI	19	0.074	0.007	0.1045109	0.067967
Pochula	CULH	26	0.998	0.001	0.0603902	0.648209
	TEXC	23	0.999	0.000	0.0608561	0.72945
	CSRL	16	0.998	0.000	0.0614887	0.914394
	POCH	39	0.994	0.009	0.0370263	0.977026
	PHLW	19	0.995	0.005	0.0516198	0.970474
	OCOT	26	0.948	0.060	0.0572164	0.740296
	ISLT	36	0.635	0.119	0.0459761	0.839922
	PICO	39	0.520	0.076	0.0307243	0.993883
	TULA	33	0.474	0.019	0.0427192	0.946834
	VCHO	45	0.420	0.027	0.0380131	0.929538
	ATEM	37	0.337	0.047	0.0509313	0.66973
	PAPA	13	0.211	0.020	0.0584610	0.984087

Table S5. Results of downsampling the number of individuals per population on Hartigan's Dip Statistic results, based on 1,000 replicate simulations. For each simulation, 22 individuals were drawn from the total sample for the population without replacement before calculating Hartigan's Dip Statistic. Rightmost columns represent the proportion of the 1,000 simulations in which the *P*-value for the departure from unimodality was nominally significant (Proportion P < 0.05) or significant at the same Bonferroni correction threshold used in the main text (Proportion Bonferroni Significant, i.e. P < 0.001105).

Drainage	***Site Code***	***Full Sample N***	***Full Sample D***	***Mean Down-sampled D***	***Proportion P* < 0.05**	***Proportion Bonferroni Significant***
Huazalingo	CRZN	113	0.0319384	0.061501	0.014	0
	TOTO	227	0.0161153	0.058308	0	0
Calnali	CALM	79	0.1597263	0.162670	0.967	0.845
	AGZC	51	0.2146567	0.194172	0.999	0.976
	PILO	80	0.1161647	0.125770	0.773	0.429
	PLAZ	73	0.0453731	0.068764	0.047	0.001
	CALL	702	0.0108287	0.063760	0.02	0.001
	CAPS	36	0.0692381	0.082225	0.095	0
	PEZM	22	0.0617895	0.061790	0	0
Conzintla	XOCH	70	0.1924042	0.186371	0.993	0.908
	MXLA	29	0.1281781	0.128963	0.9	0.285
Pochula	TULA	33	0.0427192	0.056138	0	0

Table S6. Results of Type-II ANOVA and Tukey HSD test for differences in water chemistry parameters between streams, with the Río Calnali split into sites upstream and downstream of the center of the town of Calnali. Sites from CAPAC to PILO were treated as upstream, sites from PLAZ to CHAF were treated as downstream. All values were log-transformed to better fit the assumption of normality (Shapiro-Wilks test $P > 0.01$ for all model residuals). Because of the presence of zero values in these measurements, 0.001 was added to ammonia and nitrite values to avoid undefined log-transformations. Drainages with the same letter code were not significantly different by Tukey HSD testing.

Ammonia

ANOVA	*Sum Sq*	*D.f.*	F	P *(>F)*	*Signif.*	***Tukey HSD***	*Group*
Drainage	112.784	4	16.666	1.04E-09	***	Huazalingo	A
Month	122.055	2	36.072	1.40E-11	***	Calnali - Upstream	A
Interaction	19.024	5	2.249	0.05851	.	Calnali - Downstream	B
Residuals	121.811	72				Pochula	A
						Conzintla	A

Nitrite

ANOVA	*Sum Sq*	*D.f.*	F	P *(>F)*	*Signif.*	***Tukey HSD***	*Group*
Drainage	100.639	4	21.867	7.67E-12	***	Huazalingo	A
Month	18.44	2	8.0135	0.000721	***	Calnali - Upstream	A
Interaction	7.502	5	1.3041	0.271867		Calnali - Downstream	B
Residuals	82.842	72				Pochula	A
						Conzintla	A

fDOM

ANOVA	*Sum Sq*	*D.f.*	F	P *(>F)*	*Signif.*	***Tukey HSD***	*Group*
Drainage	45.34	4	41.6948	<1E-15	***	Huazalingo	A
Month	6.959	2	12.7999	8.91E-06	***	Calnali - Upstream	B
Interaction	1.054	6	0.6463	0.693		Calnali - Downstream	B
Residuals	33.438	123				Pochula	A
						Conzintla	A

Turbidity

ANOVA	*Sum Sq*	*D.f.*	F	P *(>F)*	*Signif.*	***Tukey HSD***	*Group*
Drainage	53.89	4	23.8405	9.16E-12	***	Huazalingo	A
Month	1.744	2	1.5433	2.22E-01		Calnali - Upstream	B
Interaction	1.142	6	0.3367	0.9148		Calnali - Downstream	C
Residuals	33.341	59				Pochula	B
						Conzintla	A

References

1. B. M. Moran, *et al.*, A lethal mitonuclear incompatibility in complex I of natural hybrids. *Nature* **626**, 119–127 (2024).

2. D. L. Powell, *et al.*, Natural hybridization reveals incompatible alleles that cause melanoma in swordtail fish. *Science* **368**, 731–736 (2020).

3. INEGI, Conjunto de datos vectoriales Geológicos. serie I. Pachuca. Clava carta F14-11. 1:250000. (1983).

4. C. Y. Payne, *et al.*, Recent evolution of large offspring size and post-fertilization nutrient provisioning in swordtails. *Proceedings of the Royal Society B: Biological Sciences* **293**, 20251945 (2026).

5. H. U. Amilpa, "Estrategia reproductiva de tres especies del género Xiphophorus (Pisces: Poeciliidae) en la cuenca del río Atlapexco, México," Universidad Autonoma de Queretaro, Santiago de Queretaro, Queretaro, MX. (2006).

6. F. Jamil Emon, *et al.*, Bioaccumulation and bioremediation of heavy metals in fishes—a review. *Toxics* **11**, 510 (2023).

7. A. J. Horowitz, K. A. Elrick, The relation of stream sediment surface area, grain size and composition to trace element chemistry. *Applied Geochemistry* **2**, 437–451 (1987).

8. R. J. Erickson, D. R. Mount, T. L. Highland, J. Russell Hockett, C. T. Jenson, The relative importance of waterborne and dietborne arsenic exposure on survival and growth of juvenile rainbow trout. *Aquatic Toxicology* **104**, 108–115 (2011).

9. P. C. Hubbard, E. N. Barata, A. V. M. Canario, Possible disruption of pheromonal communication by humic acid in the goldfish, Carassius auratus. *Aquatic Toxicology* **60**, 169–183 (2002).

10. R. M. R. S. Mesquita, A. V. M. Canário, E. Melo, Partition of fish pheromones between water and aggregates of humic acids. consequences for sexual signaling. *Environmental Science & Technology* **37**, 742–746 (2003).

11. B. Scaglia, F. Tambone, F. Adani, Cr(VI) reduction capability of humic acid extracted from the organic component of municipal solid waste. *Journal of Environmental Sciences* **25**, 487–494 (2013).